SOKENDAI (The Graduate University for Advanced Studies)

Dissimilar-metal bondings for reduced-activation ferritic/martensitic steel, oxide-dispersion-strengthened steel, and stainless steel

Haiying FU

Doctor of Philosophy

2015

Contents

Abstract

Reduced activation ferritic/martensitic (RAFM) steels are considered as one of the promising structural materials for fusion blanket systems because of their mature fabrication technologies, good irradiation resistance, and excellent thermo-mechanical properties. The operation temperature of RAFM steels ranges from 300^oC to 550^oC. Oxide-dispersion-strengthened RAFM (ODS-RAFM) steels are produced with high number-density nano-scale oxide particles. Because ODS-RAFM steels have excellent high temperature strength and good irradiation resistance, the dissimilar-metal joints can be used in the first wall blanket to locate the ODS-RAFM steels near the blanket surface and to enhance the acceptable heat load from the fusion plasma. In this concept, the acceptable temperature of the first wall will be improved to 700^oC from 550^oC of full-conventional-RAFM-blanket concept. Thus, it is important to develop dissimilar-metal bonding between ODS-RAFM steels and conventional RAFM steels to apply ODS-RAFM steels in advanced concept of fusion blanket systems. While, austenitic stainless steels are structural materials of out-vessel components for tritium extraction and heat exchange in a fusion reactor. For the connection of the blanket to the out-vessel components, it is also essential to develop dissimilar-metal bonding between conventional RAFM steels and austenitic stainless steels.

By considering a plate bonding for thermal protection on the blanket surface, the first wall structure requires large area and complicated-shape bonding for ODS-RAFM steels and conventional RAFM steels with a typical cross section of one square meter. Compared with other techniques, diffusion bonding with hot isostatic pressing (HIP) is more suitable for such bonding. For the cooling channel connection inside or at the backside of the blanket between ODS-RAFM steels and conventional RAFM steels, and between conventional RAFM steels and austenitic stainless steels, electron beam welding (EBW) is necessary for robust bonding with several millimeters in thickness to resist the coolant pressure.

In this study, an ODS-RAFM steel, designated as 9Cr-ODS, and a conventional RAFM steel, JLF-1, were bonded by EBW and HIP. Another conventional RAFM steel,

F82H, and austenitic stainless steel type 316L were also bonded by EBW. Bonding mechanisms and optimum bonding conditions were investigated for these dissimilar-metal joints. As a result of the bonding, the weld metal (WM: the melted zone during the welding), heat-affected zones (HAZs: the heat-damaged zone around the WM with mechanical property and microstructural change) and the base metals (BMs) in the joints exhibited undesirable hardening or softening. Post-weld heat treatment (PWHT) was studied for recovery of microstructure and mechanical properties for these joints. The mechanisms for the degradation and recovery were well understood by carbon behavior in the steels, such as phase transformation with carbide decomposition, carbon dissolution and re-precipitation, and carbide coarsening and decarburization. In addition, the experimental mechanical property tests were combined with computer simulations using finite element method (FEM), which revealed better-estimated bonding strength of the EBW joint between 9Cr-ODS and JLF-1 compared with conventional experiments. On the other hand, the joint between F82H steel and 316L steel, was neutron-irradiated and showed good resistance to neutron-irradiation embrittlement under a commercial reactor condition.

1. Dissimilar-metal joints between 9Cr-ODS steel and JLF-1 steel made by HIP

Dissimilar-metal joints between 9Cr-ODS and JLF-1 were fabricated by HIP at 1000°C, 1050°C, and 1100°C, under a pressure of 191 MPa for 3h with a cooling rate of 5°C/min after the HIP. The HIP process always induced undesirable hardening in the BM of JLF-1, and also undesirable softening at the bonding interface, irrespective of the HIP temperatures.

The hardening is due to the formation of quenched martensite, because the cooling rate after the HIP was enough for quenching before carbon diffusion in the BM of JLF-1. While, it was too slow for 9Cr-ODS when HIP at 1000°C, where coarse carbides observed on the grain boundaries evidently indicated much diffusion of the carbon before quenching. No quenching (ferritic structure) and the carbide coarsening resulted in the softening of the BM of 9Cr-ODS. However, HIP at higher temperatures of 1050°C and 1100°C also induced quenched martensite with smaller coarse carbides. For the recovery

of both the hardening and softening in the BMs, PWHT with normalization (1050°C×1h) and tempering (780°C×1h) with a rapid cooling at 36°C/min was effective.

On the other hand, the softening at the interface is attributed to decarburization of the specimen surface during the HIP process before bonding, which produced few-particle soft layer there. The soft layer is clearly observed in the 1000°C-HIP specimen, and can be a potential fracture site in tensile tests. Coarse carbides near the interface are more than those in 9Cr-ODS BM, and can be another potential fracture site during tensile tests. There is also supposed to have un-bonded areas with spherical voids at the interface in the 1000°C-HIP joint, because only 1/3 yield strength of 9Cr-ODS is needed to make the joint fracture with almost no elongation in tensile tests. However, the elongation was improved very much at higher HIP temperatures, such as 1050°C and 1100°C. Disappearance of the few-particle layer is observed at these temperatures. It is probably promoted by the decomposition of the $M_{23}C_6$ carbides and re-distribution of carbon at the high temperatures and the following diffusion of carbon into the few-particle layer. Actually, 1100°C HIP resulted in slight lower strength of the joint than 1050°C HIP. This is likely because of coarsening of grain structures. Therefore, 1050°C is the optimum HIP temperature in the present study. The following PWHT with normalization and tempering is necessary to recover microstructure and mechanical properties of the whole joint.

2. Dissimilar-metal joint between 9Cr-ODS steel and JLF-1 steel made by EBW

Dissimilar-metal butt joint between 9Cr-ODS and JLF-1 was fabricated by EBW with an output of 15 mA and 150 V and with a speed of 2000 mm/min. The electron beam was at the butting position for the plates.

The hardness of WM and HAZs in both 9Cr-ODS and JLF-1 was much higher than the BMs. The WM is quenched martensitic phase with occasional δ-ferrite phase. The HAZs are also quenched martensitic phase with carbide decomposition. The quenched martensite in the WM and HAZs contributes unacceptable hardening for the joints. Two conditions of PWHT were carried out to relieve the hardening and recover the microstructures of WM and HAZs to the levels close to the BMs.

One condition of PWHT is only tempering at 720-780°C for 1h. The tempering changes the quenched martensite into softer tempered martensite. As tempering

temperature increased, the hardening of WM and HAZs was relieved. The complete recovery of the hardening is obtained by tempering at 780°C for 1h. However, the δ-ferrite phase still remained in the WM, and softening of BMs was induced by over-tempering.

The other condition of PWHT is a combination of normalization at 1050°C for 1h and then the complete-recovery tempering at 780°C for 1h. Because of the normalization, residual δ-ferrite disappeared. The whole microstructure including WM, HAZs, and BMs is quenched martensite after the normalization. After the following tempering, the whole microstructure is tempered martensite. No residual δ-ferrite existed anymore. The PWHT is the optimum to relief the hardening of WM and HAZs, and eliminate the residual ferrite at the same time. The strength of BMs was kept in the similar level as that before EBW. No softening of BMs induced by over-tempering was observed in this PWHT condition with normalization and tempering.

All the specimens fractured at the BM of JLF-1 during tensile tests, because the interface is stronger than BM of JLF-1. In this situation, the bonding strength cannot be determined by uniaxial tensile tests in the same way as the HIP joints, and is estimated larger than the ultimate tensile strength of JLF-1. In order to make better estimation of the bonding strength of the joint, symmetric four-point bend tests, which can concentrate the stress inside the inner span including the WM, was executed for the joint. Bending normal stress can be calculated according to the theory of elasticity within only 0.25% in strain, though the joint shows large deformation with more than 10% in strain due to plastic deformation. Thus, FEM simulation was used to extend the analysis to large deformation condition in the bend tests.

The large deformation induces sliding at the contact areas between the specimen and jig. The sliding must be also simulated for accurate analysis, which requires an input parameter of friction coefficient at the contact areas. The friction coefficient was fitted by simulation for bending behavior on BM-single-material specimens. According to the coincidence of the displacement-load curves of the upper jig between simulation and experiment, the friction coefficient was determined as 0.3 for the contact between 9Cr-ODS and jig at RT, 0.5 and 0.55 between JLF-1 and jig at RT and 550°C, respectively. Because of the analysis on the friction, the simulation successfully calculated the stress

distribution in the specimens up to strain of 20.0% at RT and 23.4% at 550°C. The maximum stress applied to the WM of the joint is estimated as 854 MPa at RT and 505 MPa at 550°C. The bonding strength is estimated to be larger than these stresses because the specimens did not fracture during bend tests. The FEM simulation successfully made better estimation for bonding strength than uniaxial tensile tests and conventional analysis on bend tests with the theory of elasticity.

3. Dissimilar-metal joint between F82H steel and 316L stainless steel made by EBW

The butt joint between F82H steel and 316L steel plates with a thickness of 7 mm was made by EBW with an output of 20 mA and 150 V, and a welding speed of 2000 mm/min. The electron beam position was 0.2 mm shifted from the butting position toward 316L side according to previous studies. PWHT condition was also determined by the previous study as 680°C for 1h.

Neutron irradiation was carried out for the joint at 300°C with a neutron flux of 5.6±0.1×10^{23} n m^{-2}, which is equivalent to a dose of 0.1 dpa (displacement per atom). The joint will be located near the vacuum vessel and superconducting magnet in fusion reactors. The maximum dose for the vacuum vessel in ITER (International thermonuclear experimental reactor) has been estimated as 0.027 dpa. The neutron flux at the magnets in commercial-grade reactor design is about 1×10^{23} n m^{-2}. Since the present irradiation dose was more than these conditions, it is enough to evaluate the resistance of the dissimilar-metal joint to neutron irradiation under fusion reactor condition.

Neutron irradiation induced hardening for the whole part of joint, such as BMs, WM, and HAZs. Hardness of the joint before irradiation ranged from 180 HV to 210 HV, while the one after the irradiation ranged from 230 HV to 300 HV. In addition, significant hardening area with 450 HV in hardness and with a size of 50 µm was discovered at the fine-grain HAZ of F82H. One of possible mechanisms for the significant hardening is irradiation-induced precipitations produced by the carbides decomposed during the welding. The PWHT condition with 680°C for the irradiated specimens was determined by the previous study, mainly from the viewpoint to avoid softening of F82H steel by over-tempering. However, it was not enough to complete the recovery of the hardness change by the welding. The present study found a better PWHT condition as 750°C for

1h from further investigation from the viewpoint of precipitation control. This PWHT will suppress the significant irradiation hardening and should be examined under neutron irradiation in future.

Fortunately, the significant irradiation hardening observed in the HAZ of F82H did not degrade the impact property of the joint. This is probably because the hardening volume was very limited. In addition, 316L steel part of the joint maintained much ductility and assisted the deformation of the joint during the impact test. The present study successfully demonstrated the resistance of the joint to neutron irradiation under the commercial reactor condition. The results presented in the work are expected to provide technical reference for the design and construction of a fusion reactor in the future.

1.   Introduction

There is great demand for electric power in the world today and tomorrow. A lot of resources can be utilized for power generation, such as oil, coal, natural gas, hydropower, geothermy, wind, biofuels, solar, nuclear, and so on. The non-renewable resources such as oil, coal and natural gas, are limited and consumable, and become fewer and fewer. The renewable resources such as wind, solar, and biofuels, are scattered, unstable, technology-limited, and small-production. They cannot fulfill the increasing demand of humans completely. Nuclear is a kind of promising power resource. Figure 1-1 demonstrates that nuclear power will play more and more important role in the next decades to fulfill the huge demands of electricity by humans.
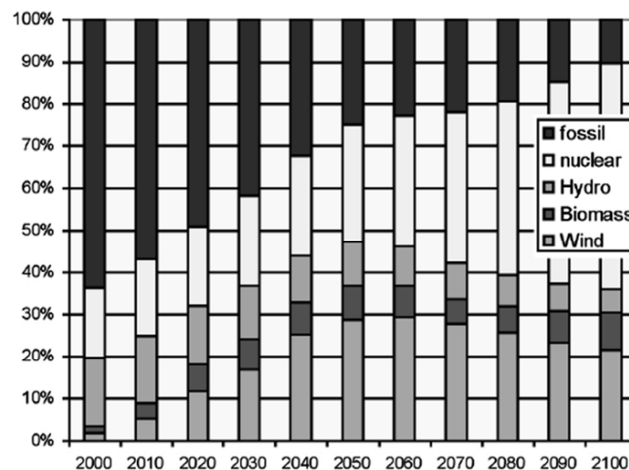
Figure 1-1 Evolution of electricity mix in the next decades[1].

Fusion nuclear energy is a type of safe and clean power without high level radioactive waste and CO_2 emission[2,3]. The fusion reactions in the reactor core are expressed in the followings[4],

$$D + T \rightarrow n \ (14.1 \ \text{MeV}) + {}^4\text{He} \ (3.5 \ \text{MeV}) \qquad (1\text{-}1)$$

$$D + {}^3\text{He} \rightarrow {}^4\text{He} \ (3.5 \ \text{MeV}) + p \ (14.6 \ \text{MeV}) \qquad (1\text{-}2)$$

$$D + D \rightarrow n \ (2.5 \ \text{MeV}) + {}^3\text{He} \ (0.8 \ \text{MeV}) \qquad (1\text{-}3)$$

$$\rightarrow T(1.0 \ \text{MeV}) + p \ (3.0 \ \text{MeV})$$
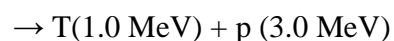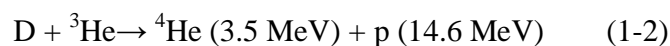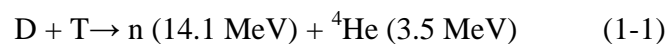
Figure 1-2 shows the reaction rate of fusion reactions. The D-T reaction is the most possible because relatively low temperature (several tens keV, i.e. $4.7 \times 10^{7o}C$[5]) is needed to have a peak cross section. Totally 17.6 MeV (2×10^{-12} J) is released for the D-T reaction, 14.1 MeV with neutron and 3.5 MeV with helium.

The fuel tritium is quite rare in nature. However it can be produced in the breeding blanket of a fusion reactor through the reaction of lithium with neutron as follows,

$$n + {}^{6}Li \rightarrow T + {}^{4}He + 4.8 \text{ MeV} \qquad (1\text{-}4)$$

$$n + {}^{7}Li \rightarrow T + {}^{4}He + n - 2.5 \text{ MeV} \qquad (1\text{-}5)$$
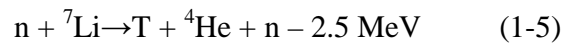
For a 1 GW fusion power plant, only 0.1 ton deuterium and 10 tons lithium per year[2] as fuels is needed. The fuels deuterium and lithium are inexhaustible on the earth. They can be obtained from sea water. While tritium can be obtained by industrial production and from the breeding system of the fusion blanket itself by isotope separation techniques with column exchange separation method and vacuum distillation method[2].

Fusion energy is safe and clean from the following viewpoints: (1) unlike fission energy with chain reaction, D and T fuels are fed continuously into the fusion reactor. When the feeding is stopped, fusion reactions stopped immediately. (2) No green-house gas CO_2 emitted in the fusion reactor. The production by D-T reaction is helium, which is not radioactive at all. (3) Tritium is a radioactive element with half-life of only 12 years. However tritium is confined and bred in the blanket by the reaction between lithium and neutron. The hazard potential due to radioactivity is only 1/1500 of that of a fission reactor[2]. (4) The only nuclear waste is structural materials with neutron induced activation. The present material design of fusion reactors is focused on recycling of structural materials after 50 to 100 years cooling down. In this case, structural materials with low-activation are required.
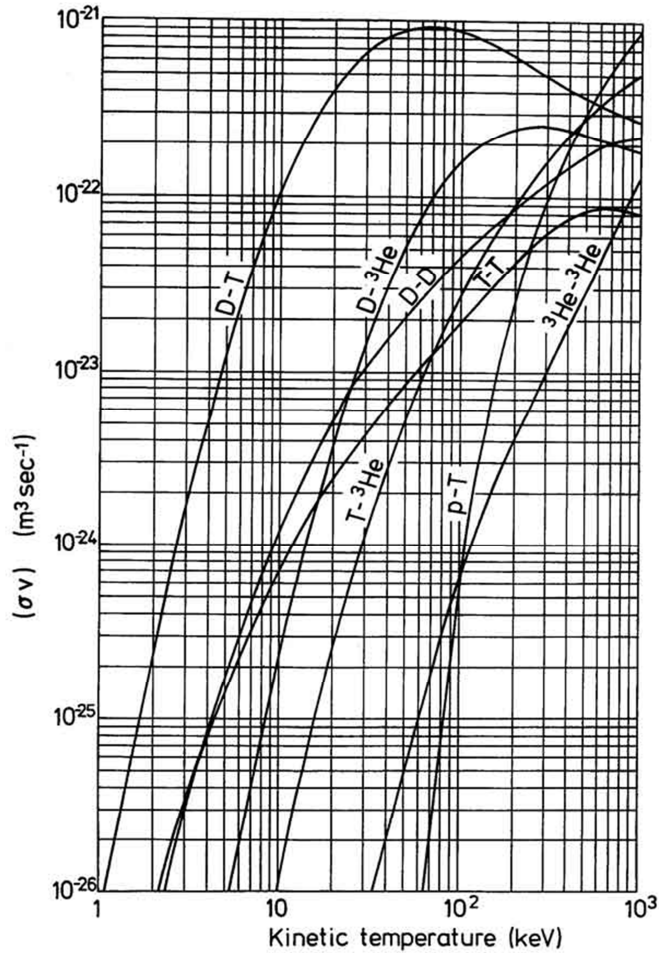
Figure 1-2 Fusion reaction rate between light atoms[2] (for the kinetic temperature, 1 eV corresponds to $11600^{\circ}C$).

As depicted in Figure 1-2, hot D-T plasmas are required with temperature of about $10 \times 10^{7\circ}C$ for the fusion reaction. The thermo-nuclear plasma has to meet the condition of self-sustained ignition $n.\tau_E.T > 5 \times 10^{21}$ m^{-3} keV.s[1], where τ_E is the confinement time, n the electronic density, and T the temperature. The research and development of fusion energy have already persisted almost 60 years since the 1950s. Achievement of fusion energy is not easy because it is hard to maintain burning after heating the plasma to the extremely high temperature for igniting fusion reaction. There are no commercial fusion reactors in the world yet since the key issues for plasma control are unsolved. However, two types of experimental facilities for fusion research are operated, designed, or under construction. (a) Inertial confinement fusion facilities[4][6] are the National Ignition Facility[7] (NIF, USA), the Laser MegaJoule facility[8] (LMJ, France), Shenguang

9

facility (SG-IV, China), the Fast Ignition Realization Experiment project (FIREX)[9][10] and International Laboratory Inertial Fusion Test (i-LIFT) experimental reactor (Japan). (b) Magnetic confinement fusion facilities of *Tokamak-type* are JT-60U[11] (Japan), EAST[12] (China), HL-2A[13] (China), Korea Superconducting Tokamak Advanced Research facility[14] (KSTAR, Korea), the Joint European Torus[15] (JET, EU), the Tokamak Fusion Test Reactor tritium facility[16][17] (TFTR, USA), and of *Helical-type* such as the Large Helical Device[18] (LHD, Japan), the WENDELSTEIN 7-X stellarator[19] (W7-X, Germany).
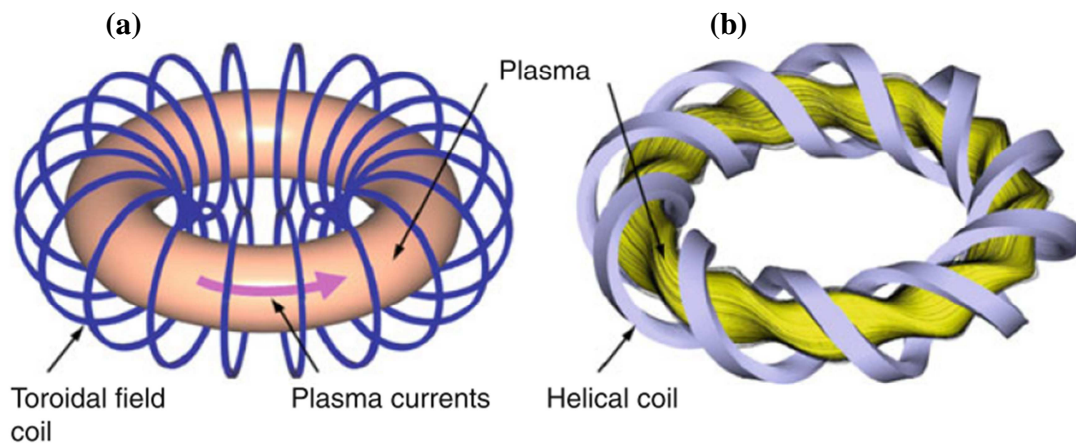
Figure 1-3 Two concepts of magnetic confinement fusion, (a) Tokamak type, (b) Helical type[2].

Figure 1-3(a) illustrates the concept of Tokamak-type magnetic confinement of fusion. The plasma with currents is confined by the toroidal field coils, and then is heated to high temperature to meet the self-sustained ignition condition for fusion reaction. International Thermonuclear Experimental Reactor (ITER) is a kind of Tokamak facility under construction in Cadarache, France, by the joint cooperation of seven leading parties, i.e. China, EU, Japan, India, Korea, Russia, and the USA. ITER does not have the plan for electrical power generation. The goal of ITER is just to demonstrate control of burning plasma and engineering feasibility[20][21] of a fusion reactor. The first D-T operation in ITER is estimated in 2027[22]. National Institute for Fusion Science (NIFS) in Japan is famous for the large helical device (LHD). As depicted in Figure 1-3(b), it utilizes helical coils to generate magnetic field for confining plasmas. The helical system has advantages of steady-state and stable operation compared with Tokamak system,

because it does not need currents in plasma to generate helical magnetic field for confinement.

1.1 Fusion reactor and structural materials

Typical structure of a fusion reactor contains vacuum vessel, breeding and shielding blanket, magnet system, cryostat, cooling systems, and so on. Figure 1-4 is a kind of force-free helical reactor FFHR-2[23] designed in NIFS. The plasma major radius is 14 m. It can produce fusion power of 1.9 GW. By considering the construction of a fusion reactor, not only to develop materials itself, but also it is important to develop component fabrication technologies of divertor, blanket, superconductors, cryostat, and bonding and assembly of these different kinds of components together. Among these components, two in-vessel components i.e. divertor and blanket, are particularly important for the operation of a fusion reactor. The former is essential to self-sustained ignition by purifying the plasma with evacuation of α particles and impurities. The significance of the latter is extracting the energy from neutron and plasma, breeding tritium fuel for self-sufficient operation, and proving shielding for the out-vessel components such as superconductors.
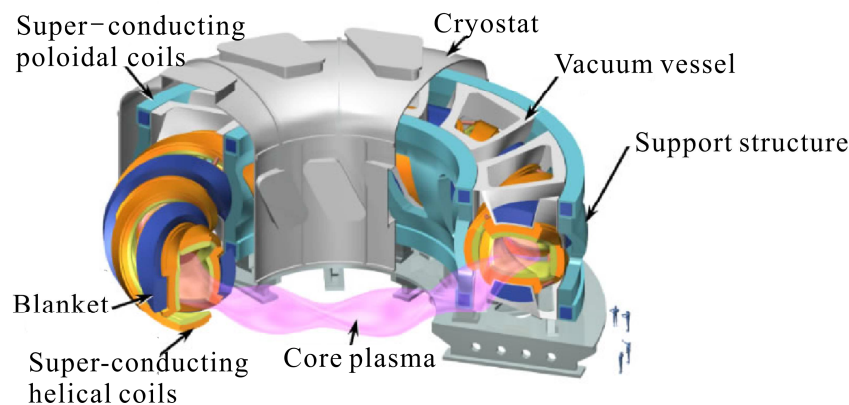
Figure 1-4 Helical-type reactor FFHR-2 designed in NIFS[23].

Development of blanket structural materials to resist the high flux of 14 MeV neutrons generated by the D-T reaction is a key issue for the construction and normal

11

operation of fusion nuclear power plants. The first wall blanket has to evacuate peak heat flux of 0.5 MW/m^2[24]. In addition, the 14 MeV intense neutrons will make huge damages to the structural materials because the neutrons have no electrical charge and cannot be confined by the magnetic field. The blanket structure will undergo 30-80 dpa[25] (displacement per atom) in the Demonstration (DEMO) reactors or even 100-150 dpa in prototype commercial reactors[26][27], respectively. In addition, the D-T reaction will produce high concentration of He and H in the structural materials with a production rate of 10 and 45 appm/dpa[1], respectively. This means that the structural materials should have excellent resistance to high dose neutron irradiation, high heat load, and He/H swelling and embrittlement at the same time.

Moreover, the structural materials should satisfy low-activation requirement by considering minimization of radioactive waste and its hazard. There are four types of low activation criteria for structural materials of fusion reactors as the following examples,

(1) Release limit: one-year dose to the population due to the maximum release to environment in case of the worst accidental conditions. The early dose should be under 50 mSv[28].

(2) Maintenance limit: contact dose rate after one day of cooling should not exceed 10^4 Gy/h[28].

(3) Waste disposal limit: decay heat should be less than 10 W/m^3 and contact dose rate under 20 mSv/h after no more than 50 years of cooling (acceptable for deep geological repository (DGR))[28]. 10 μSv/year can be as shallow land burial (SLB) criterion after 300 years cooling[29].

(4) Recycling limit: for remote recycling, the limit is 10 mSv/h[30] after 50 years cooling. For hands-on recycling, the contact dose rate should be less than 10 μSv/h[31] after no more than 100 years of cooling down.

Furthermore, the blanket structural materials should have excellent mechanical and physical properties, and good compatibility with the liquid coolant, to keep well operation during the whole life-time of a fusion reactor. The cost of fabrication and maintenance of the structure should also be acceptable. In summary, the blanket structural materials in a fusion reactor should meet the requirements shown in Table **1-1**.

Table 1-1 Requirements for fusion blanket materials.

	Requirements
1	Low-activation property to decrease radioactive waste and its hazard on environment and the population.
2	Excellent high-temperature mechanical properties and their stability during the lifetime.
3	Satisfactory tolerance against neutron and heat loads from D-T plasma.
4	Resistance to swelling and H/He embrittlement.
5	Sufficient compatibility with breeder/coolant.
6	Machinability and acceptable cost for fabrication and maintenance.

In the fusion blanket systems, there are three candidates for structural materials, i.e. reduced activation ferritic/martensitic (RAFM) steels, vanadium alloys, and SiC/SiC composites. Table 1-2 lists these structural materials utilized in different design concepts of blanket systems. The blanket concepts with different structural materials are classified into solid-breeder/water-cooled, solid-breeder/He-cooled, Li/self-cooled, FLiBe/self-cooled, and so on. The maximum application temperature of the blanket is $550^{o}C$ for RAFM steels as structural materials, $700^{o}C$ for vanadium alloys, and $1157^{o}C$ for SiC/SiC composites. If the high-temperature mechanical properties of RAFM steels and vanadium alloys are improved by advanced nano-particle dispersion strengthening, the application temperature of the blanket can be increased by $100\text{-}150^{o}C$.

Table 1-2 Structural materials in different concepts of blanket systems[32][33].

Concept	SSTR[34][35][36]	ARIES-RS [37][38][39]	A-SSTR2[40]	FFHR-2[41]
Breeder	Li_2O, Li_2TiO_3 (pebble bed)	Li	Li_2TiO_3 (pebble bed)	FLiBe
Breeder temperature (^{o}C)	300-600(900)	330-610	700-800	450-550
Multiplier	Be (pebble bed)	—	Be (pebble bed)	Be (pebble bed)
Multiplier temperature	300-600	—	700-800	

(°C)

	H_2O	Li	He	FLiBe
Coolant	H_2O	Li	He	FLiBe
Coolant temperature (°C)	280(290*)-320(520*)	330-610	600-900	450-550 (700)
Coolant pressure	15 (25*)	<1	10	0.5
Structural material	RAFM	Vanadium	SiC/SiC	RAFM, vanadium
Structural temperature (°C)	280-550	330-700	700-1157	300-550 (700)
Max. neutron wall load (MW/m^2)	3-5	5.6	6	1.5
Max. surface heat flux (MW/m^2)	1	0.5	<1	0.1
Energy multiplication factor	1.3	1.21	1.3	
Tritium breeding ratio	1.2	1.1	1.3	>1
Thermal efficiency (%)	35 (>40*)	46	>50	38

*supercritical – pressurized water

RAFM steels are selected as the first candidate structural materials in fusion blanket systems due to their mature fabrication technology, good neutron irradiation resistance, and excellent thermo- physical and mechanical properties[42–44]. Chemical compositions of RAFM steels should be limited by considering minimization of the residual radioactive waste. Table 1-3 shows the maximum permissible concentrations of elements in the RAFM steels according to remote recycling criteria after 50 years cooling down, and hands-on recycling criteria after 100 years cooling down. Figure 1-5 compares dose rate of several blanket structural materials after 30 years operation in the reactor FFHR-2 with Li as coolant. V-4Cr-4Ti alloy (NIFS-HEAT-2) and pure SiC can reach the full-remote recycling level (30 years after cooling down) earlier than RAFM steel (F82H) (50 years after cooling down). However, after 100 years cooling down, RAFM steel (F82H) reaches the same level as that of V-4Cr-4Ti alloy (NIFS-HEAT-2) for full-remote recycling.

Table 1-3 Maximum permissible concentrations of the elements in steel according to the "hands-on" limit on surface γ-dose at 100 year after irradiation[45][46].

	No limit	10-90%	1-10%	0.1-1%	100-1000 ppm	10-100 ppm	1-10 ppm	0.1-1 ppm	<0.1 ppm
100-year cooling, "Hands-on" limit	H, He, Li, Be, B, C, N, O, F, Ne, Na, Mg, P, S, Ar, V, Cr, Mn, Ga, Ge, As, Se, Sr, Y, Sb, Te, I, Pr, Au, Hg, Tl	Si, Cl, K, Fe, Zn, Rh, Sn, La, Ce	Ca, Br, Rb, Ru, In, W, Re	Ti, Zr, Yb, Lu, Ta	Sc, Ni, Cu, Mo, Pb	Al, Kr, Cs, Ba, Nd, Er, Tm, Pt	Co, Pd, Cd, Xe, Sm, Gd, Dy, Hf	Nb, Os, Bi	Ag, Eu, Tb, Ho, Ir
50-year cooling, "Remote recycling" limit	H, He, Li, Be, B, C, N, O, F, Ne, Mg, Si, P, S, Cl, Ar, K, Ca, V, Cr, Mn, Ga, Ge, As, Se, Br, Zr, Ru, In, Sr, Y, Sb, Te, I, La, Ce, Pr, Ta, W, Re, Au, Hg, Tl	Na, Ti, Fe, Zn, Rb, Sn, Yb, Pb	Al, Sc, Mo, Er, Tm, Lu, Pt	Kr, Rh, Pd, Cd, Xe, Nd, Dy	Ni, Cu, Cs, Ba, Sm, Gd, Hf	Nb, Ho, Os, Bi	Co, Ag, Tb, Ir	Eu	–
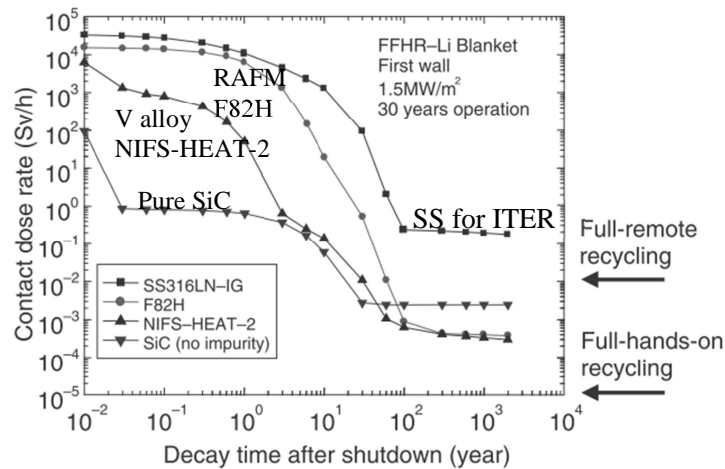
Figure 1-5 Dose rate after shutdown for different structural materials[47].

RAFM steels are ferritic or martensitic structure. Compared with austenitic steels 316SS, as shown in Figure 1-6, these steels have much smaller void swelling after neutron irradiation, since high density dislocations, large areas of packets and lath boundaries in the structure of RAFM steels provide sinks for neutron irradiation defects[48]. Table 1-4 shows the chemical composition range of RAFM steels. The steels commonly contain 8% to 9% Cr, because at this range, the steels have the smallest

ductile-to-britle transition temperature (DBTT) shift due to neutron irradiation, as indicated in Figure 1-7. W contents are optimized to balance solution hardening effect and against embrittlement by Laves phase. In the world, various RAFM steels are developed, such as F82H[49] and JLF-1[50] (Japan), Eurofer 97[51] (EU), CLF-1[52] and CLAM[53] (China), 9Cr-2WVTa[54] (USA), and so on.

Oxide-dispersion-strengthened (ODS) RAFM steels have more superior high temperature strength than conventional RAFM steels. Its maximum application temperature can be increased by 100-150°C compared with conventional RAFM steels[55]. The first ODS ferritic steels developed in Japan were in Japan Atomic Energy Agency (JAEA) in 1987, for fuel pin cladding tubes to endure heavy displacement damage to 250 dpa at high temperatures up to 700°C in commercial sodium cooled fast breeder reactor cores[1]. Nowadays, to develop ODS-RAFM steels for fusion application, valuable experiences from ODS pin cladding have been drawn on. Two types of ODS-RAFM steels have been developed in Japan, 9Cr-ODS martensitic steels for better radiation resistance, and 12~15Cr-ODS ferritic steels for better corrosion resistance. The chemical composition range of ODS-RAFM steels shown in Table 1-4 is mainly designed to maximize high temperature strength by high number-density nano-scale oxide-particle dispersion and solution strengthening mechanisms. C and Cr contents are designed for α to γ transformation to form martensite for 9Cr-ODS steel, and to form fully ferrite for 12~15Cr-ODS steels. Ti, Y, and O concentrations are optimized for high temperature strength by controlling microstructure. ODS-RAFM steels are usually fabricated by mechanical alloying, hot extrusion or hot-isostatic pressing, and hot forging[56]. There are many kinds of ODS-RAFM steels developed in the world, such as 9Cr-ODS and 12Cr-ODS[56][57] (Japan), SOC1, SOC5, SOC-P3[58][59] (14~16Cr-ODS, Japan), 15Cr-ODS[60] (Korea), ODS Eurofer[61][62][63](EU), Fe–14CrWTi ODS[64] (France), ODS-CLF[65] (China), ODS CLAM[66] (China), etc.

16
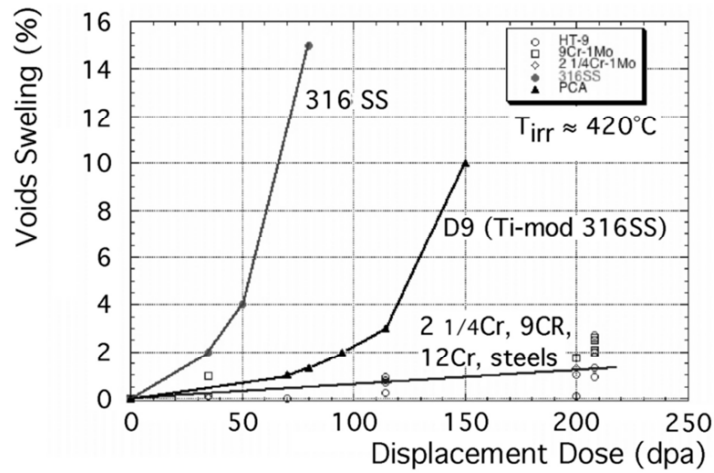
Figure 1-6 Void swelling behavior after neutron irradiation for austenitic steels and banite/martensite/ferrite steels[1].

Table 1-4 Chemical composition range of RAFM and ODS-RAFM steels (wt. %).

Steels	Fe	Cr	W	C	Ti	Y	V	Ta	O
RAFM	Bal.	8-9	1-2	0.1-0.15			0.2	0.04-0.15	
ODS-RAFM	Bal.	9-15	1-2	<0.03-0.15	0.2-0.4	0.2-0.3			0.1-0.2
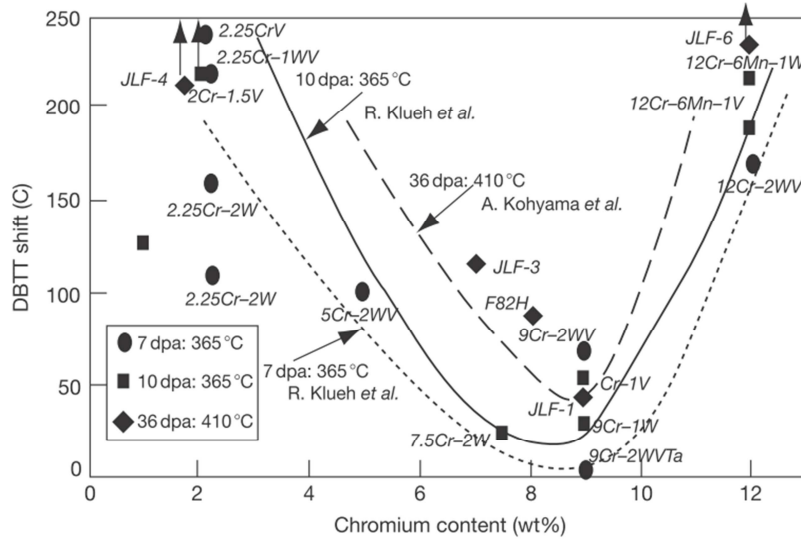
Figure 1-7 DBTT shift for several steels with different Cr content after neutron irradiation[67].

A lot of issues should be concerned for the development of both conventional RAFM steels and ODS-RAFM steels: (1) Manufactory techniques especially for industrial

17

production with low activation characteristics are critical to meet large demand of structural materials in the blanket of the future fusion plants. (2) Irradiation induced hardening and shift of DBTT after irradiation at temperatures below 350°C are the most critical issues for ferritic and martensitic steels. It is important to develop advanced RAFM steels especially ODS-RAFM steels for excellent irradiation resistance. (3) Compatibility with coolant is important to apply RAFM steels in fusion blanket. Development of proper coating in the coolant tubes is necessary to increase corrosion resistance. (4) Development of component fabricating technologies is also essential to the construction of the blanket structure of a fusion reactor. The issue (4) is very important but has not been investigated systematically yet. Therefore, the present study focuses on this issue.

1.2 Dissimilar-metal bonding issues for fusion reactors

The main technologies to fabricate a blanket include: (a) cutting and machining of semi-finished products, (b) bonding of comonents especially for the plates with internal coolant channels, (c) bending of coolant pipes as well as avoiding fusion welding close to the first wall[68], (d) post-weld heat treatment (PWHT) of the joints to improve mechanical properties. Among these, bonding techniques and the following PWHT are the most important to determing the mechanical strength and the DBTT before and after neutron irradiation.

By considering development of component fabrication technologies for fusion blanket systems, invesitigation of bonding techniques for structural materials has been carried out by scientists in the world. Nowadays, lots of activities are conducted for single-metal bondings (the bondings for themselves) of RAFM steels and ODS-RAFM steels, as shown in Table 1-5. The single-metal joints are mainly fabricated by techniques of electron beam welding (EBW), hot isostatic pressing (HIP) or hot pressing (HP), tungsten inert gas welding (TIGW), pressurized resistance welding (PRW), laser welding (LW), friction stir welding (FSW), and so on. For the bondings of conventional RAFM steels, all the above techniques are applicable. However, for ODS-RAFM steels, usually fusion

welding such as LW, EBW, and TIGW should be avoided. Otherwise, disruption of nano-scale oxide particles in the heat-affected zones (HAZs) and weld metal (WM) would be induced. This would lead to degradation of mechanical properties of the joints. K. Hatayama et al.[69] have investigated bonding of 9Cr-ODS steel by LW, EBW, and TIGW. The joints fractured at the WM by tensile tests because of local softening there. The bonding strength is only 53-75% of that of the base metal (BM). R. Lindau et al.[70] have developed the single-metal bonding for ODS Eurofer by EBW. Compared to BM, loss of tensile strength and impact absorbed energy was found for the joint due to grain and particle coarsening in the WM. The joint is considered to be applied in regions with lower mechanical loads of fusion blanket systems.

Other techniques such as diffusion bonding with HP or HIP and forging welding with FSW or PRW are more suitable for the bonding of ODS-RAFM steels to avoid disruption of nano-scale oxide particles and fine grain structures. (1) During diffusion bonding process, an adequate temperature (50-80% of the melting temperature T_m[71]) and pressure for a specific time can be determined in the range where the atomistic interaction happened between the joint interfaces by diffusion. S. Noh et al.[72] have studied diffusion bonding by HP with phase transformation (1150°C) to join 9Cr-ODS steel. By the following PWHT with normalization and tempering (N&T), fine tempered martensitic structure and nano-scale oxide particles were homogeneously distributed at the interface region. The diffusion bonded joints exhibited the similar tensile behavior as that of the BM. (2) FSW uses the friction heat generated between the stir tool and the material of the work pieces. The heat softens the material work pieces without reaching the melting point. The materials are forged together by the intimate contact of the stir tool. W. Han et al.[73] have researched the effect of mechanical force of friction tool on grain structure of 15Cr-ODS ferrite steel. The mechanical force can activate recrystallization and contribute to grain refinement of the stir zone. Thus by well control of the mechanical force of friction tool, good bonding properties of the joints of ODS steels can be gained. (3) PRW utilizes the heat generated by resistance at the butt-aligned joint of the weld materials under a specified axial pressure while passing a large current. H. Endo et al.[74] and M. Seki et

19

al.[75] have utilized PRW for the bonding for 14Cr-ODS steel, 12Cr-ODS steel, and 9Cr-ODS. The strength of the WM was maintained equal to or higher than that of the BMs.

Table 1-5 Single-metal bonding techniques for conventional RAFM steels and ODS-RAFM steels

For conventional RAFM steels	For ODS-RAFM steels
F82H, HIP[76][77][78], TIGW[79], EBW[80]	9Cr-ODS, HP[72], PRW[75]
JLF-1, TIGW[81]	15Cr-ODS, FSW[73], HP[88]
CLAM, TIG[82], HIP[83][84]	ODS Eurofer, EBW[70]
CLF-1, EBW, HIP, TIG[85]	
Eurofer97, TIG[86], EB, LW, HIP[87]	

On the other hand, it is also essential to develop dissimilar-metal bondings for the fabrication of fusion reactors by using RAFM steels as structural material and austenitic stainless steels as out-vessel-component material. As shown in Figure 1-8 (a), if only conventional RAFM steels are used as blanket structural material by bonding with out-vessel austenitic stainless steel, the application temperature of the blanket system would be below 550°C. However, as depicted in Figure 1-8 (b), if ODS-RAFM steels used partly for the surface of fusion blanket close to the plasma by bonding with conventional RAFM steels, the application temperature of blanket surface would be increased by up to 100 to 150°C. This advanced concept is very attractive, since thermal margin is gained in the blanket design. Therefore, dissimilar-metal bondings are important topics in the blanket systems. Dissimliar-metal bonding between conventional RAFM steels and austenitic stainless steels is a common issue for both the conventional design and advanced design.
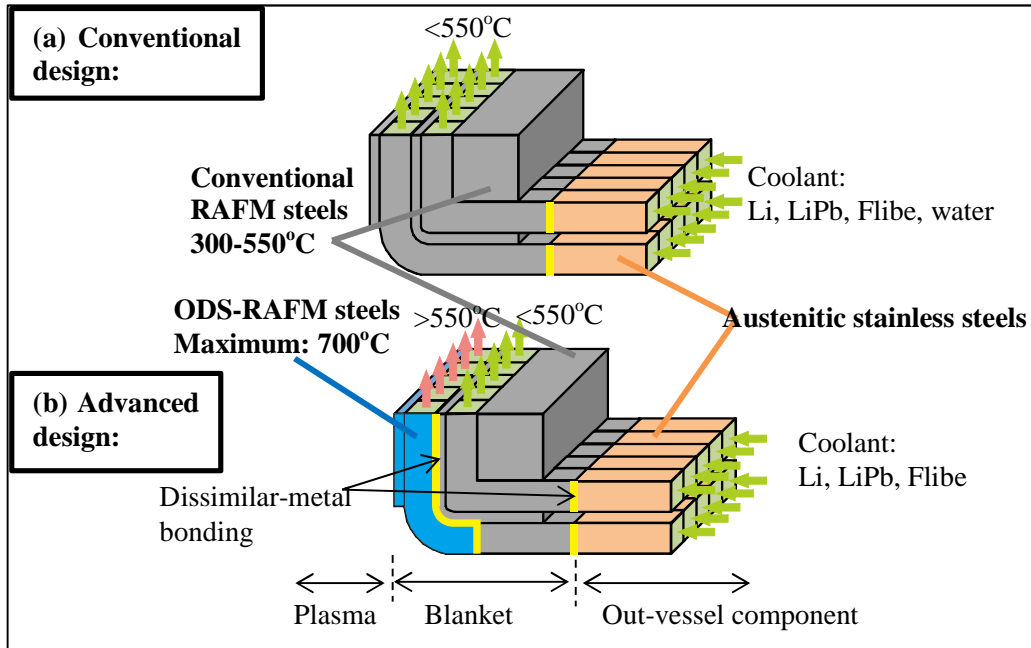
Figure 1-8 Illustration of dissimilar-metal bondings in blanket systems.

Several dissimilar-metal joints between ODS-RAFM steels and conventional RAFM steels, and between conventional RAFM steels and austenitic stainless steels are developed by scientists, as listed in Table 1-6, by EBW, HIP or HP, TIGW, LW, FSW, and so on. Unlike HP with only uniaxial pressure which is usually executed in a hydrostatic vacuum hot-press furnace, HIP produces isostatic pressure (from high-pressure gas) acting on the outer surfaces of the welding objects. Thus compared to HP, wider area bonding of components with more complicated shape can be made by HIP. For the large area bonding of the plate structure in the first wall blanket as depicted in Figure 1-8, HIP is the most suitable among the above-mentioned bonding techniques. It has been considered to be the most promising methods[77] for fabricating of blanket components of a complicated structure with rectangular coolant channels in the first wall to remove the heat from the plasma. HIP has also been chosen as the main manufacturing technique for the substructures of the test blanket modules (TBMs) for ITER[68].

Fusion welding is used for assembling of the main parts of the blanket system such as for the pipes connection. In the fusion welding techniques, EBW is more proper because it can produce robust joints with high accuracy and narrow HAZs and WM compared

with other fusion welding techniques. In addition, because of the vacuum environment, EBW can make joints without air contamination.

For the dissimilar-metal bonding between ODS-RAFM steel and conventional RAFM steel, there are some activities in Europe by R. Lindau et al.[63][89] with HIP and by L. Commin et al.[90] with EBW by using ODS Eurofer steel and Eurofer steel. Tensile tests showed good strength of the dissimilar-metal joints. Fracture always occurred outside the WM in the Eurofer part (below 550°C) or ODS Eurofer part (after 600°C), as shown in Figure 1-9. Impact tests of the joints made by HIP showed up to 80% of upper shelf energy (USE) of Eurofer BM (Figure 1-11 (a)). DBTT is about 50°C, below the DBTT of ODS Eurofer material. For the EBW dissimilar-metal joint, PWHT as shown in Figure 1-10, is required for grain structure modification and carbide re-precipitation in the WM to achieve high creep strength and low DBTT (Figure 1-11 (b)). L. Commin and R. Lindau et al. have successfully demonstrated the feasibility to apply HIP and EBW for the dissimilar-metal bonding between 9Cr ODS-RAFM and conventional RAFM.

Table 1-6 Dissimilar-metal bonding technologies currently developed in the world.

Between ODS-RAFM steels and conventional RAFM steels	Between conventional RAFM steels and austenitic stainless steels
ODS Eurofer—Eurofer, EBW[90], HIP[63][89]	F82H—SUS304, FSW[94]
15CrODS—F82H, HP[91]	F82H—316L, EBW[95,96], LW[97],
9Cr-ODS—PNC-FMS(11Cr ferrite steel), FSW[92]	TIG[98]
14YWT—F82H, FSW[93]	
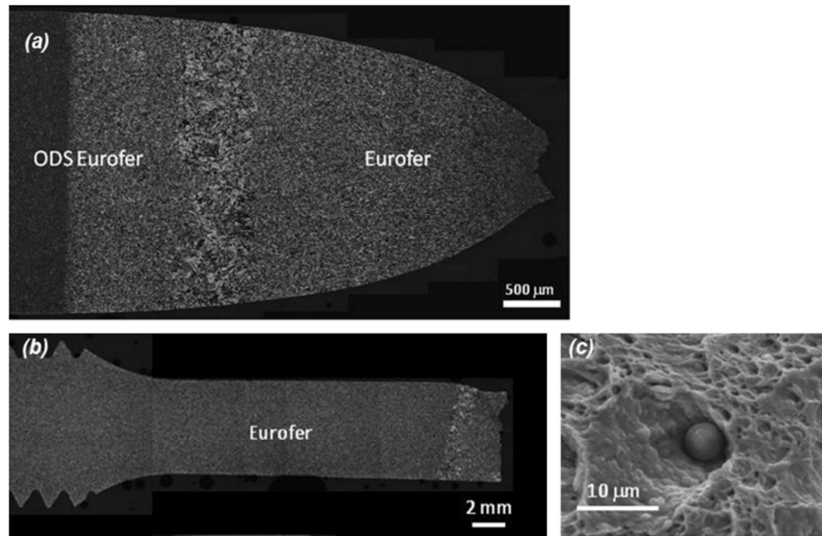
Figure 1-9 Fracture surface of the joint between ODS Eurofer and Eurofer (a) until 550°C, (b) and (c) after 600°C[90].
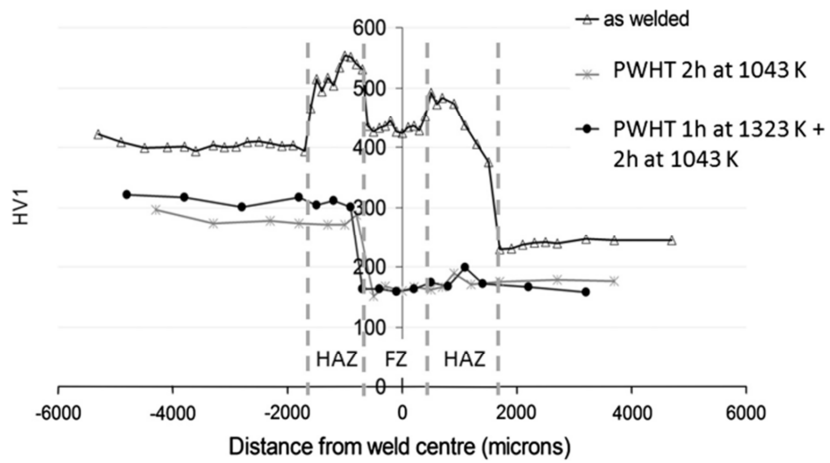
Figure 1-10 Effect of PWHT on the EBW joint between ODS Eurofer and Eurofer[90].
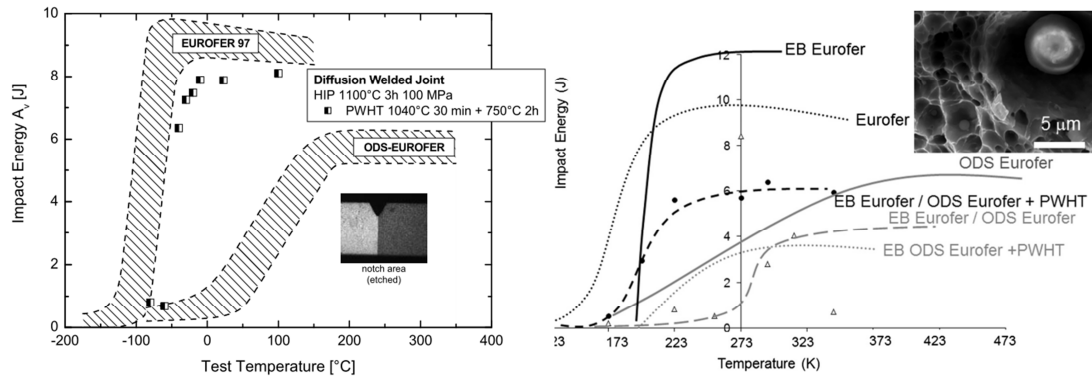
Figure 1-11 Charpy impact properties of the joint between ODS Eurofer and Eurofer (a) by HIP[63], (b) by EBW[90].

For the dissimilar-metal bonding between conventional RAFM steel and austenitic stainless steel by EBW, there are also activities conducted by S. Nogami and N. Hara[95,96] in Japan. The effect of electron beam position was investigated by N. Hara. The hardening in the WM can be completely eliminated by PWHT if the electron beam shifted 0.2 mm towards the 316L during EBW, as depicted in Figure 1-12, while the hardening cannot be cleared up if without any electron beam shift. As shown in Figure 1-13, the joint with the electron beam shifted 0.2 mm towards 316L side showed excellent impact property compared to that without any shift. In S. Nogami et al.'s work, the hardness recovery process by PWHT with tempering was investigated, as illustrated in Figure 1-14, and proton irradiation hardening was also studied for the joint in Figure 1-15.
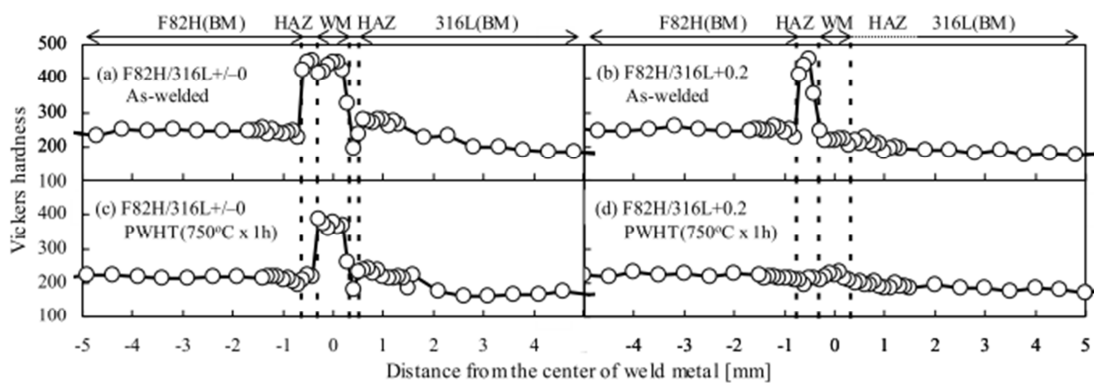
Figure 1-12 Hardness of the EBW joints with and without electron beam shift[96].
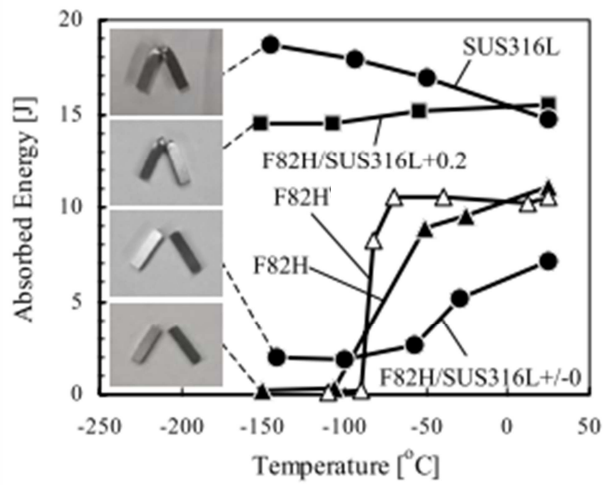
Figure 1-13 Charpy impact property of the joints between F82H and 316L when the electron beam located at different positions during EBW process[96].
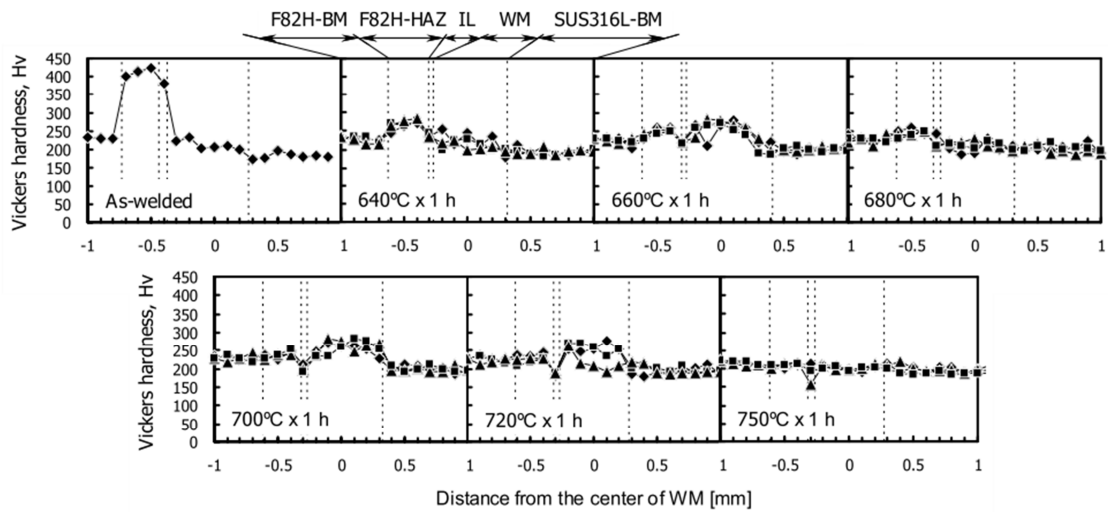
Figure 1-14 Hardness recovery of the dissimilar-joint between F82H and 316L by PWHT[95].
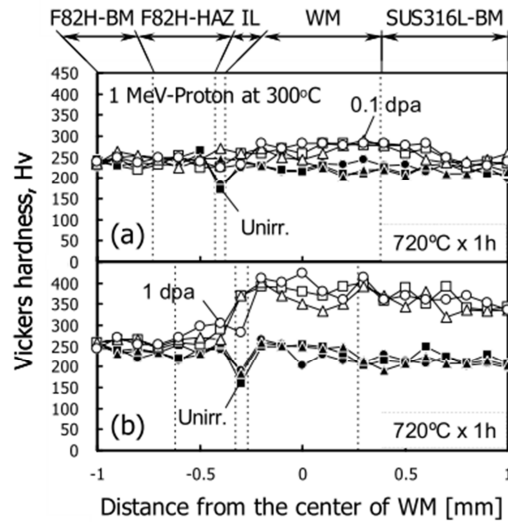
Figure 1-15 Proton irradiation on the dissimilar-metal joint between F82H and 316L at 0.1 dpa and 1dpa[95].

1.3 Motivation and purpose of this study

Dissimilar-metal bondings are very important for the construction of a fusion reactor. In the present study, dissimilar-metal joints between ODS-RAFM steels and conventional RAFM steels, and between conventional RAFM steels and austenitic stainless steels were developed by welding techniques of HIP and EBW.

As mentioned above, activities on dissimilar-metal bonding between ODS-RAFM steel (ODS Eurofer) and conventional RAFM steel (Eurofer) have been conducted in Europe by HIP and EBW. They produced the dissimilar-metal joints with the welding condition already optimized for the conventional Eurofer steel, and analyzed the effect of PWHT on mechanical properties with tensile test, Charpy impact test, and creep test. However, the optimum bonding and PWHT conditions have not been systematically investigated yet by using dissimilar-metal joints. In the present study, more progress is obtained on the optimum bonding and PWHT conditions to get good bonding properties of the dissimilar-metal joints. In addition, in their work the bonding strength was not analyzed further when the fracture occurred at the base metal, because this situation satisfies the practical requirements for joints. In the present study, further analysis on the

bonding strength was conducted to obtain the margin for fracture from academic viewpoint.

On the dissimilar-metal bonding between conventional RAFM steel and austenitic stainless steel by EBW, N. Hara and S. Nogami et al.[95][96] have preliminarily investigated the optimum bonding and PWHT conditions, and the effect of proton irradiation at 300°C for 1dpa on the joint. However, it is necessary to evaluate the irradiation resistance of the dissimilar-metal joint under neutron irradiation more close to the real fusion environment. In this work, investigation on neutron irradiation at 300°C was conducted on the basis of their work.

The following goals will be obtained,

1. Development of dissimilar-metal bondings between ODS-RAFM steel and conventional RAFM steel, and between conventional RAFM steel and austenitic steel by HIP and EBW, investigation of proper welding parameters for good bonding properties.

2. Evaluation of microstructure evolution during welding, understanding welding mechanisms, and investigation of PWHT for recovery of microstructure and mechanical properties of the dissimilar-metal joints after welding.

3. Investigation of neutron irradiation effect on the dissimilar-metal joint between conventional RAFM and austenitic stainless steel, interpreting hardening mechanism of the joint, and obtaining neutron irradiation data to provide support for the design of fusion reactors.

27

2. Experimental Procedure

2.1 Materials

Materials used in the present study are conventional RAFM steels F82H and JLF-1, ODS-RAFM steel 9Cr-ODS, and nuclear-grade austenitic stainless steel type 316L. Table 2-1 roughly introduces the fabrication process and final heat treatment conditions of these steels. RAFM steels of F82H and JLF-1 were made by vacuum induction melting (VIM) with or without electro slag re-melting (ESR)[99] followed by forging and rolling. 9Cr-ODS was fabricated by mechanical alloying, extrusion, and forging. The final heat treatments for F82H, JLF-1, and 9Cr-ODS are normalization and tempering (N&T) to form tempered martensitic structure. However, for the 316L steel, the microstructure is austenite. The fabrication process is similar as that of conventional RAFM steels with melting, forging, and rolling. However, the necessary final heat treatment is just normalization to form austenite structure.

Table 2-1 Fabrication process and final heat treatment of the materials

Materials	Fabrication process	Final heat treatment	Structure
JLF-1[50], F82H[99]	Vacuum induction melting (VIM) + electro slag re-melting (ESR), followed by hot forging and rolling	F82H:$1040^{o}C \times 40min + 750^{o}C \times 1h$ JLF-1: $1050^{o}C \times 1h + 780^{o}C \times 1h$	Tempered martensite
9Cr-ODS[56]	Mechanical alloying+ hot extrusion+ hot forging	$1050^{o}C \times 1h + 800^{o}C \times 1h$	Tempered martensite
316L	Melting + hot forging+ rolling	$1040^{o}C \times 30min$	Austenite

2.1.1 F82H and JLF-1 reduced-activation ferritic/martensitic (RAFM) steels

The conventional RAFM steels used in this work containing 8 wt.% Cr (F82H) and 9 wt.% Cr (JLF-1) solidify as δ-ferrite and transform to austenite during cooling, as shown the Fe-Cr phase diagram in Figure 2-1. When the cooling rate is sufficiently rapid, the

austenite transforms into quenched martensite. Because of low carbon content (0.09 wt.%), the steels are expected to have good resistance to under-bead cracking which was induced by internal stresses when austenite-to-martensite transformation during welding[100].
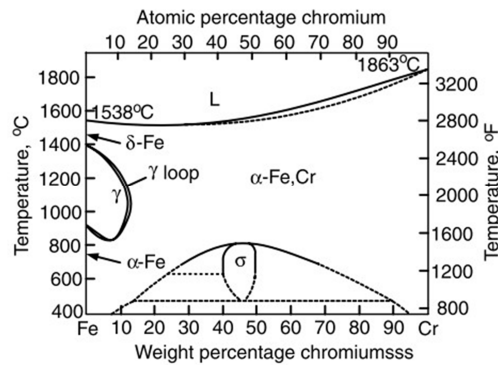
Figure 2-1 Fe-Cr phase diagram

The conventional RAFM steels used in this study are F82H-IEA heat[101][102] and JLF-1 JOYO heat[102], respectively. The chemical composition of them is shown in Table 2-2.

Table 2-2 Chemical composition of F82H and JLF-1 (wt.%).

	C	Si	Mn	P	Cr	W	Cu	Ni	Mo
F82H	0.091	0.11	0.16	0.002	7.71	1.95	0.01	0.02	0.003
JLF-1	0.09	0.05	0.49	<0.003	9.00	1.98			

	V	Ta	N	O	S	Co	Ti	Al
F82H	0.16	0.02	0.006		0.002	0.005	0.01	0.003
JLF-1	0.20	0.083	0.015	0.002	0.0005			

2.1.2 9Cr oxide-dispersion-strengthened (ODS) RAFM steel

The ODS-RAFM steel used in this study is 9Cr-ODS steel. The detailed fabrication process of 9Cr-ODS steel is shown in Figure 2-2. Argon gas atomized pre-alloyed steel powders and Y_2O_3 particulates were mechanical alloyed by ball mill in high purity argon gas atmosphere to avoid contamination by air. The mechanical alloying was carried out for 48h with a rotation speed of 220 rpm. The mixed powders were sieved, filled into mild steel cans, degassed at 400°C for 3h. And then, 3 bars with 30 mm in diameter were

hot extruded at 1150°C with the ratio of 6.4. By the following hot forging at 1150°C, plates with thickness of 10 mm were made. The final annealing is 1050°C×1h for normalization and 800°C×1h for tempering, with air cooling (AC). At last, by cutting and shaping, plates with 5 to 6 mm in thickness were fabricated.

Argon gas atomized power
pre-alloyed, <150 μm

↓

Addition of Y$_2$O$_3$ (about 20 nm in diameter)
Addition of elements for compositional adjustment

↓

Mechanical alloying
Attrition ball milling (220 rpm, 48h, Ar)

↓

Canning, Degassing
(400°C, >3h)

↓

Hot extrusion
(1150°C, extrusion ratio=6.4, φ30 mm)

↓

Hot Forging
(1150°C, 50-60 mm (width) ×10 mm (thickness))

↓

Annealing
(1050°C×1h, AC+ 800°C×1h, AC)

↓

Cutting, shaping
(40 mm (width)) × 200 mm (length) × 5-6 mm (thickness))

Figure 2-2 Fabrication process of 9Cr-ODS plates, reproduced from[56].

The detailed chemical composition of 9Cr-ODS is shown in Table 2-3. In which, C and S were analyzed by combustion-infrared absorptiometry, Si and P by absorption spectrophotometry, Mn, Ni, Cr, W, Ti, and Y by inductively coupled plasma atomic emission spectroscopy, and O, N and Ar by inert gas fusion method. The Y_2O_3 and excess oxygen contents were estimated as 0.37 and 0.082 in weight percentage, respectively. The excess oxygen is inevitable for ODS steels. It originates from contamination during fabrication process of mechanical alloying and the following degassing. However, the content of excess oxygen was well controlled in the 9Cr-ODS of the present study. The chemical compositions of 9Cr-ODS fulfill the low activation criterion in Table 1-3 for RAFM steels for fusion application.

Table 2-3 Detailed chemical composition of 9Cr-ODS (wt.%).

C	Si	Mn	P	S	Ni	Cr	W
0.14	0.06	0.09	<0.005	0.004	0.03	9.08	1.97
Ti	Y	O	N	Ar	Y_2O_3	Ex.O	
0.23	0.29	0.16	0.013	0.005	0.37	0.082	

Mechanical alloying is an important process for the fabrication of 9Cr-ODS steel. It controls the size distribution of nano-scale oxide particles, the dispersion hardening effect and microstructure controllability in the following fabrication of plates with hot extrusion and hot forging. Repeated severe plastic deformation occurred for the alloy powders during mechanical alloying process with high energy ball milling. It provides stored energy for recrystallization and nucleation for precipitation. During the following hot extrusion and hot forging process, Ti, Y, and O precipitated out to form finely dispersed complicated nano-scale oxide particles. The microstructure of 9Cr-ODS taken by optical microscopy (OM), scanning electron microscopy (SEM), and transmission electron microscopy (TEM) is displayed in Figure 2-3. The grain size of the steel is 1 to 2 μm. High density carbides are homogeneous distributed on the grain boundaries. TEM observation showed that the steel has tempered martensitic structure with carbides and dislocations. The size and density of nano-scale oxide particles are 3.1 nm and 1.2×10^{23} m^{-3}, respectively.

The strain-stress curves of 9Cr-ODS are depicted in Figure 2-4. The yield strength is about 1170 MPa at RT and 270 MPa at 700°C. The strength of 9Cr-ODS is much higher than that of conventional RAFM steels.
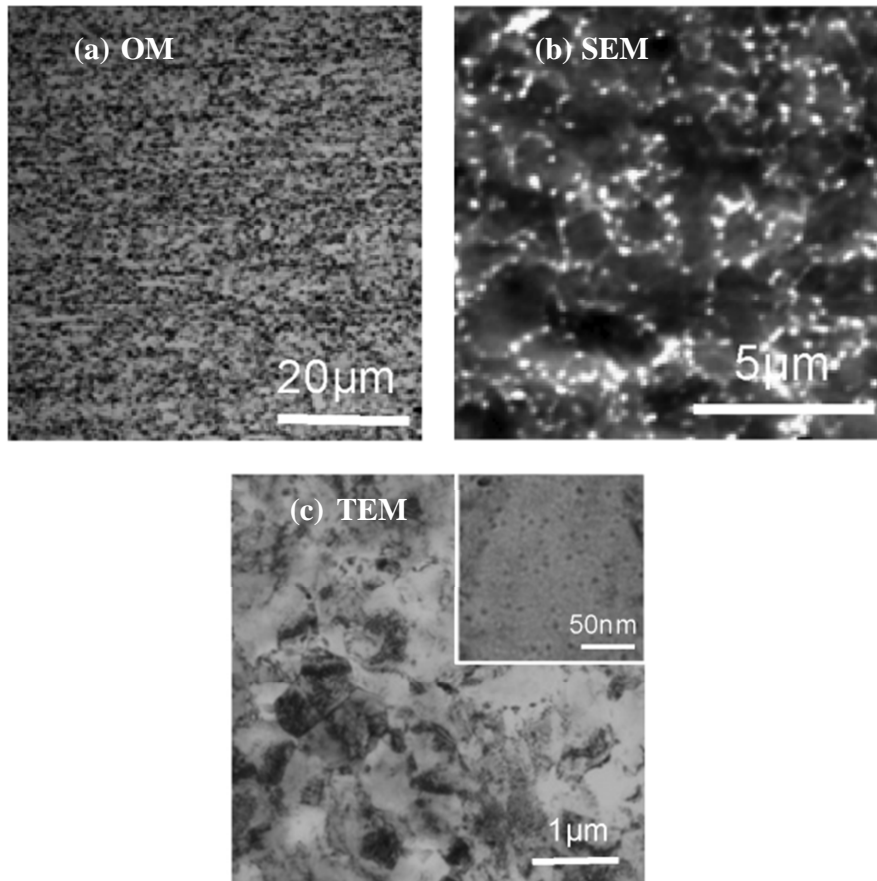
Figure 2-3 Microstructure of 9Cr-ODS taken by OM, SEM, and TEM[56].
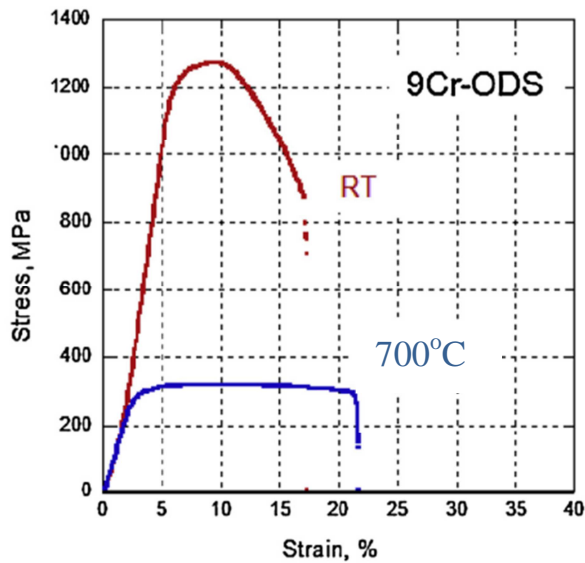
Figure 2-4 Tensile curves of 9Cr-ODS at RT and 700°C[56].

2.1.3 316L austenitic stainless steel

316L austenitic steel is chosen as the out-vessel component material for heat exchanger, and tritium extractor in fusion reactors. Elements of Ni and Mn in the steel extend the γ-loop in the Fe-C phase diagram. Adding Ni into the Fe-Cr alloys can widen the austenite existing window and increase its stability at low temperatures. It contains more than 15 wt.% Cr and enough Ni to maintain a stable austenitic structure over the temperature window from 1100°C to room temperature (RT). Cr not only retards the kinetics of the γ→α transformation, but also has corrosion resistance because of the formation of a very thin stable oxide film on the surface of austenitic steel[103].

Usually, conventional austenitic stainless steels are more susceptible to stress-corrosion cracking (SCC) at high operation temperature 300°C. In the presence of an aqueous solution in nuclear-reactor environments, SCC attack easily occurs by a mechanism of inter-granular failure, and is aggravated by the precipitation of carbides and depletion of alloy, and the segregation of impurities at the grain boundaries. Nuclear-grade 316L austenitic stainless steels have been developed worldwide to solve the problem of SCC attack.

The austenitic steel used in the present work is the nuclear grade 316L steel. It contains less C, Si, and S than conventional 316L steel to increase resistance of SCC sensitization, as shown the chemical composition comparison in Table 2-4. Co is limited to a maximum of 0.05% to minimize neutron radioactivity due to the (n, γ) reaction. B is limited to maximum 0.004% because of its neutron-capture properties, which influence the neutron economy adversely.

The detailed chemical composition of the nuclear grade 316L steel used in the present work is shown in Table 2-5. H, N, and O were analyzed by inert gas fusion method, C by combustion-infrared absorptiometry, Zr, Nb, and Ta by inductively coupled plasma atomic emission spectroscopy, and the others by glow discharge mass spectrometry.

Table 2-4 Chemical composition comparison between conventional 316L steel and nuclear grade 316L steel (wt.%)[104].

	Conventional 316L steel	Nuclear grade 316L steel
C	Max. 0.03	Max. 0.02
Mn	Max. 2.0	Max. 2.0
Si	Max. 1.0	Max. 0.75
S	Max. 0.03	Max. 0.01
P	Max. 0.03	Max. 0.03
Cr	16-18	16-18
Ni	10-14	10-14
Mo	2-3	2-3
N		Max. 0.14
B		Max. 0.004
Co		Max. 0.05

Table 2-5 Detailed chemical composition of the nuclear grade 316L steel in this work (wt.%).

H	C	N	O	Al	Si	P	S
<0.005	0.014	0.0375	0.0645	0.0034	0.745	0.0224	<0.005

Ti	V	Cr	Mn	Fe	Co	Ni	Cu
0.0017	0.0855	18.5	1.23	66	0.0544	11.4	0.0945

As	Nb	Mo	Sn	W
<0.01	0.0823	1.91	0.0055	0.0033

2.2 Hot isostatic pressing (HIP) and post-weld heat treatment (PWHT)

HIP is a kind of solid-state diffusion bonding process. The temperatures for HIP process are commonly beyond the AC_3 line in the Fe-C phase diagram. During the HIP process, the elements would be diffused at the interface, and then the BMs are bonded together. Materials for HIP in this work were 9Cr-ODS and JLF-1 by considering large area bonding during component fabrication of plate-shape blanket structure in future. The 9Cr-ODS disks were 5 mm thick and 24 mm in diameter. The JLF-1 blocks were 20 mm thick and 24 mm in diameter. The blocks were electro-polished to remove the contamination of the surfaces with solution of 13% $HClO_4$, 13% ethylene glycol monobutyl ether, and 74% acetic acid, at 15 V below 5^oC. After cleaned and dried, as shown in Figure 2-5 (a), one 9Cr-ODS disk was sandwiched between two JLF-1 blocks and sealed into a SS300 type soft steel capsule using EBW. As illustrated in Figure 2-6 the HIP procedure, three groups of HIP were carried out at 1000^oC, 1050^oC, and 1100^oC for 3h under the pressure of 191 MPa with a cooling rate of $5^oC/min$, respectively. After HIP, no defects like pores were found by OM (Figure 2-5(b)). Specimens were machined for microstructure and mechanical properties evaluation. As illustrated in Figure 2-7 the machining instruction, the interface of the joints was located at the center of tensile specimens. The gauge size of tensile specimens is 0.25 mm×1.2 mm×5 mm. φ3 mm TEM specimens were machined in 9Cr-ODS and JLF-1 BMs. Coupon specimens (0.5 mm×4 mm×15 mm) were also machined for hardness tests and SEM microstructural analysis.
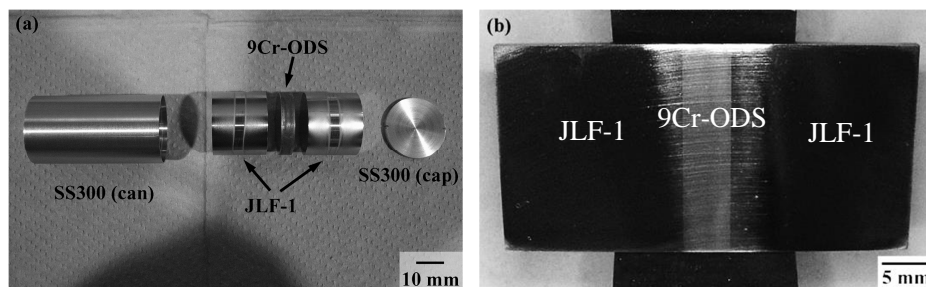
Figure 2-5 Materials of 9Cr-ODS and JLF-1 before and after HIP.
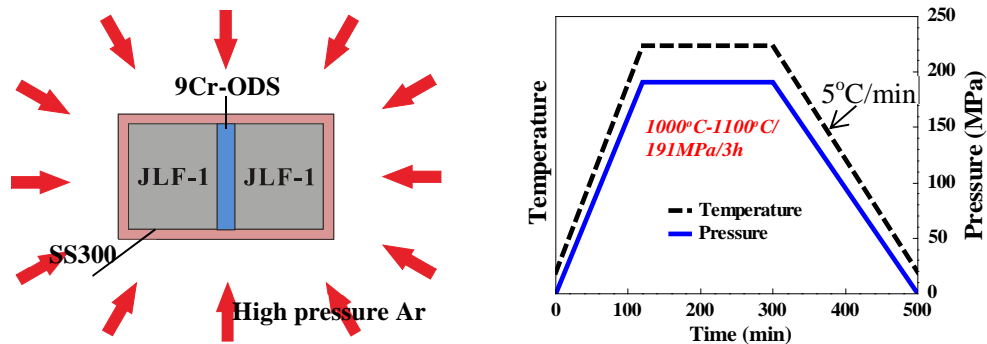
Figure 2-6 Illustration of the HIP process.
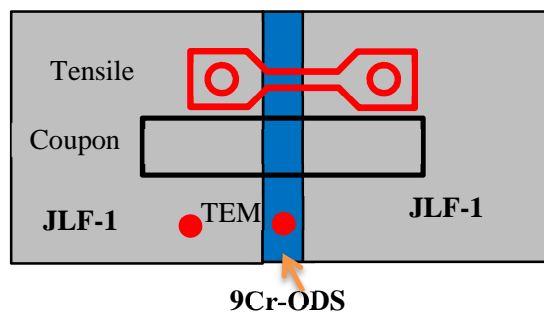
Figure 2-7 Machining of specimens for the HIPed joints.

The HIP treatment may change the microstructure and mechanical properties of the joints. PWHT was carried out for recovery of microstructure and mechanical properties by normalization (N) at 1050°C for 1h and tempering (T) at 720-820°C for 1h with a fast cooling rate of 36°C/min (compared with the one in the HIP process mentioned above) in an image furnace with the vacuum less than $3*10^{-4}$ Pa. After PWHT for these joints, microstructural characterization was conducted by OM, SEM, and TEM. Mechanical properties evaluation was carried out by tensile tests and hardness tests.

2.3 Electron-beam welding (EBW) and PWHT

EBW is different from HIP. It is a kind of fusion welding process. The metals are melted by the high-temperature focused electron beam. The BMs are bonded together robustly after rapid cooling of the melted liquid. In this study, EBW was executed for the joints between 9Cr-ODS and JLF-1, and between F82H and 316L, as illustrated in Figure 2-8 and Figure 2-9.

The electron beam was located at the butting position between 9Cr-ODS and JLF-1. After EBW, machining was conducted for tensile, coupon, and bending specimens with the WM located at the center. Because the high heat during EBW would induce microstructural disruption of WM and HAZs, PWHT with normalization and tempering (N&T) or only tempering (T) was carried out for hardening relief of WM and HAZs, as shown in Table 2-6.
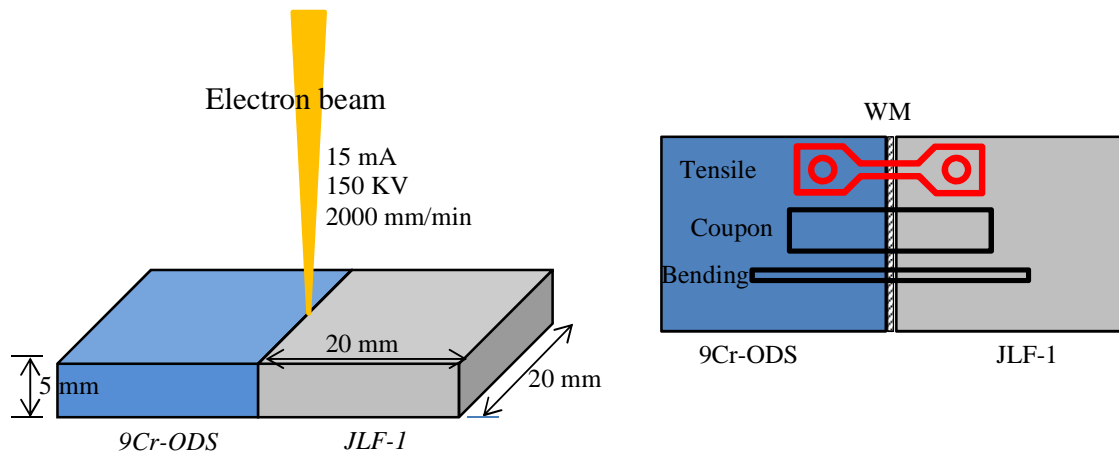
Figure 2-8 Schematic illustration of EBW process and machining instruction of the joints between 9Cr-ODS and JLF-1.
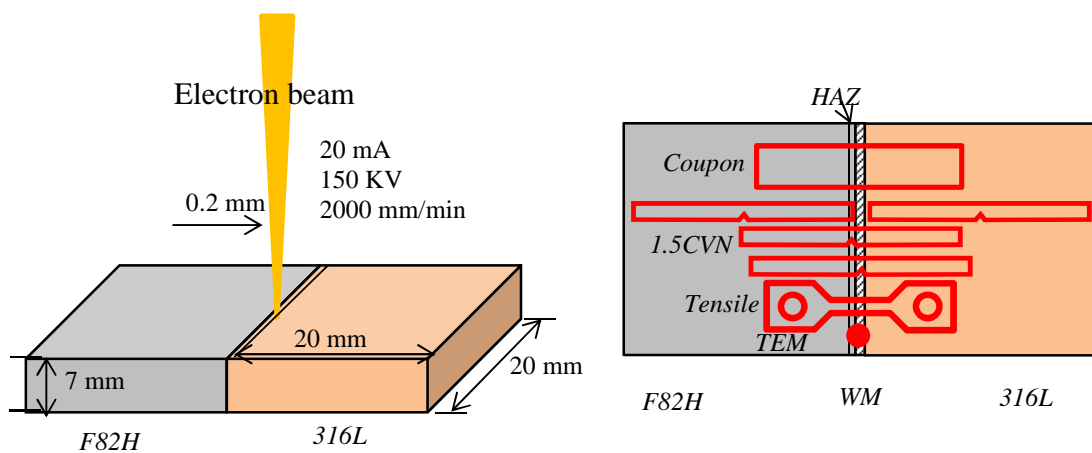
Figure 2-9 Schematic illustration of the EBW process and machining instruction of the joint between F82H and 316L.

Table 2-6 PWHT of the EBW joints.

Joints	PWHT
9Cr-ODS—JLF-1	Normalization and tempering (N&T): $1050^{o}C\times1h+780^{o}C\times1h$
	Tempering (T): $720\text{-}780^{o}C\times1h$
F82H—316L	Tempering (T): $640\text{-}750^{o}C\times1h$

For the joint between F82H and 316L, the electron beam was 0.2 mm shifted towards the 316L side according to the previous study[96]. Tensile, coupon, φ3mm TEM specimens were also machined for microstructure and mechanical properties evaluation. In addition, 1.5CVN Charpy impact specimens (1.5 mm×1.5 mm×20 mm) were also machined with the V-notch located at positions of WM, HAZ of F82H, and BMs of 316L and F82H. The 1.5CVN specimens were designated according to the position of the V-notch, as shown in Table **2-7**. PWHT was also carried out for the joint between F82H and 316L at $640\text{-}750^{o}C$ for 1h, as shown in Table 2-6. Evolution of hardening relief in the HAZ of F82H was studied.

Table 2-7 Naming of the 1.5CVN specimens

Position of the V-notch	ID of the 1.5CVN specimens
BM of F82H	F82H-BM
BM of 316L	316L-BM
HAZ of F82H	F82H-HAZ
WM	WM

DBTT of the 1.5CVN specimens was evaluated for the EBW joint between F82H and 316L after PWHT and after neutron irradiation. DBTT is defined as the temperature when the absorbed energy is half of the upper shelf energy (Figure 2-10). Below this temperature, the material is brittle. DBTT is an important property for the evaluation of a material's ductility especially after neutron irradiation.

38
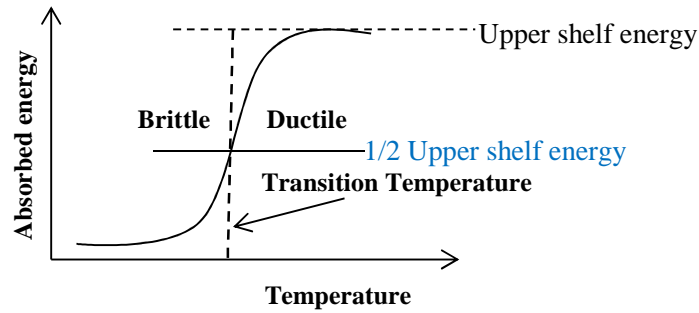
Figure 2-10 Definition of DBTT.

2.4 Neutron irradiation on the dissimilar-metal joint of F82H steel—316L steel

Neutron irradiation of the dissimilar-metal joint between F82H and 316L after PWHT at 680°C for 1h was executed in the water cooled facility CALLISTO at the reactor BRII in Belgium.

The dissimilar-metal joint is expected to be located behind fusion blanket. Therefore neutron irradiation condition should be similar to the vacuum vessel and magnets. The neutron irradiation was carried out at 300°C for the dose of 0.1 dpa (for Fe). The detail is shown in Table 2-8. Mechanical properties of hardness and impact properties were evaluated after neutron irradiation. Impact properties were evaluated for the 1.5CVN specimens with the V-notch at the WM, HAZ of F82H, and BMs of F82H and 316L.

Table 2-8 Irradiation condition for the joint between F82H and 316L.

Irradiation facility	CALLISTO, BRII
Fluence (E> 1MeV)	5.5 to 5.7×10^{23} n/m^2
Irradiation time	40 days, 2 cycles
Damage	0.1 dpa (for Fe)
Irradiation temperature	295 ± 12°C
Specimens	1.5CVN

2.5 Microstructural characterization and mechanical property tests

Microstructural characterization was carried out for the dissimilar-metal joints in the conditions of as-HIPed, as-welded, and after PWHT. The coupon specimens for the joints were etched, and then observed with OM and SEM.

Table 2-9 shows several kinds of etchant for the joints. For the joint between F82H and 316L, because the microstructure of 316L and WM is austenite, different with that of F82H, tempered martensite, the ordinary etching solution does not have effect on 316L and WM for microstructure display. Oxalic acid solution can be used to reveal grain structures of F82H, 316L, and the WM. But it makes the carbides in F82H dissolved. Thus according to different purpose, different solution can be selected for microstructural analysis of the dissimilar-metal joints in this study. For better estimation of carbides in the joints between 9Cr-ODS and JLF-1, and BM of F82H, the first 3 kinds in the table can be considered. For grain size estimation, the fourth with oxalic acid can be chosen.

Table 2-9 Etchant for microstructural display of the dissimilar-metal joints.

	Etchant	For the joints between 9Cr-ODS and JLF-1, F82H BM	For 316L BM	For WM of F82H-316L
1	1g Picric acid + 5ml Hydrochloric acid + 100ml Ethanol, RT	Laths + carbides	No effect	No effect
2	13% Perchloric acid + 74% Acetic acid + 13% 2-butoxyethanol, 0-10°C, electro-etching, 30V, 10s	Laths + carbides	No effect	No effect
3	25% Hydrofluoric acid + 25% Nitric acid + 50% Ethanol, RT	Laths + carbides	No effect	No effect
4	10g Oxalic acid + 100ml water, 0-10°C, electro-etching, 10V, 20s	Lath+ grain boundaries, carbides disappeared.	Grain boundaries	Dendritic structure

Microstructural analysis with TEM was also carried out for the joints. The TEM specimens were 3 mm in diameter and 0.25 mm in thickness. After electro-polishing in

the electrolyte with 5% Perchloric acid and 95% acetic acid at RT, TEM observation was operated at a voltage of 200 kV.

Hardness tests were carried out for the dissimilar-metal joints with a load of 100g for 30s. In order to distinguish the interface or fusion boundary for better locating and without disturbance of grain boundaries on hardness results, the coupon specimens were mechanical polished, and etched with about 20% diluted etching solution with picric acid shown in Table 2-9. Hardness across the interface or WM of the dissimilar-metal joints was measured to evaluate hardening or softening probably happened on the BMs, HAZs, WM, or interface during HIP or EBW and the following PWHT process.

Uniaxial tensile tests, as illustrated in Figure 2-11, with an initial strain rate of $6.7 \times 10^{-4} \, s^{-1}$ were carried out at RT and 550^oC for the dissimilar-metal joints between 9Cr-ODS and JLF-1, and at RT and 300^oC for the joint between F82H and 316L. 550^oC and 300^oC are the maximum operation temperatures of the joints between 9Cr-ODS and JLF-1, and the joint between F82H and 316L, respectively. The high-temperature tensile tests were executed in a vacuum less than 10^{-6} torr with the specimens surrounded by Zr foil to scavenge O and N gas. The tensile specimens are SSJ specimens, as shown in Figure 2-12. The gauge size of the tensile specimens is 5 mm×1.2 mm.
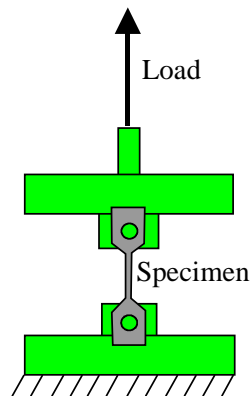
Figure 2-11 Illustration of tensile test.
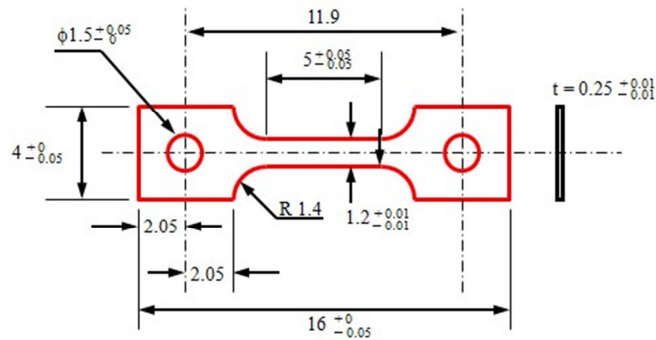
Figure 2-12 Dimension of SSJ tensile specimen.

For the dissimilar-metal joints which fractured at BM, not at the interface or WM, tensile tests cannot be utilized to obtain the bonding strength of the joints anymore. In this case, symmetric four-point bend experiments (Figure 2-13) which can concentrate the stress inside the inner span including the WM were carried out to get the bonding strength of the joints. Besides the dissimilar-metal joints, bend experiments of the BMs were also carried out to get friction coefficient between BMs and jig, as explained in detail in Chapter 4. The size of the bending specimens is 1.5 mm×1.5 mm×20 mm, as illustrated in Figure 2-14.
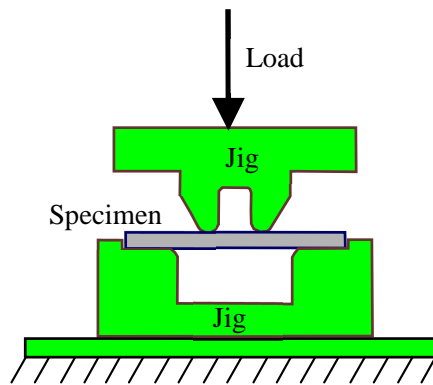
Figure 2-13 Illustration of symmetric four-point bend test.
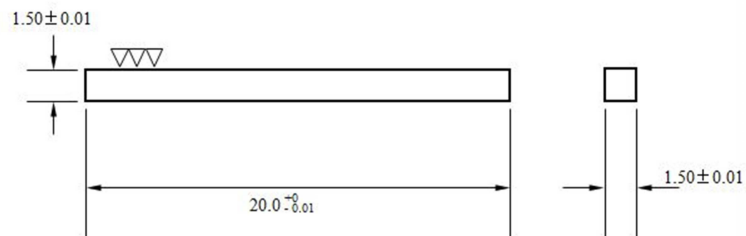
Figure 2-14 Dimension of the bending specimen.

2.6 Summary

Dissimilar-metal joints between ODS-RAFM steel, 9Cr-ODS, and conventional RAFM steel, JLF-1, between RAFM steel F82H and austenitic steel 316L were fabricated by HIP or EBW. PWHT was utilized to recover microstructure and mechanical properties. It is beneficial to understand the bonding mechanisms and provide proper bonding conditions and bonding strength for blanket design. Neutron irradiation on the joint between F82H and 316L is helpful to estimate irradiation resistance and understand irradiation hardening mechanism on this joint.

3. Results and discussion

3.1 The HIP joints of 9Cr-ODS steel—JLF-1 steel

3.1.1 Effect of PWHT

The effect of PWHT was investigated for the dissimilar-metal joint which was HIPed at 1000°C under a pressure of 191 MPa for 3h. The cooling rate after the HIP is 5°C/min as illustrated in Figure 3-1.
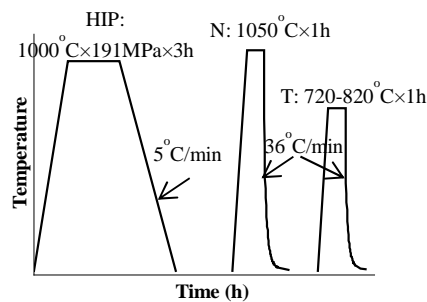
Figure 3-1 History of the HIP and PWHT procedure.

According to the continuous cooling transformation (CCT) diagram for 9Cr-ODS and conventional RAFM steel, as shown in Figure 3-2, after HIP with the cooling rate of 5°C/min (i.e., about 10^4 s would be taken cooling from the HIP temperature), the microstructure should be ferrite for 9Cr-ODS BM, while quenched martensite for JLF-1 BM. The hardness result after the HIP at 1000°C is depicted in Figure 3-3 (a). The hardness before HIP is about 350 HV for 9Cr-ODS, and 210 HV for JLF-1. After the HIP, the 9Cr-ODS was a little softened, while JLF-1 was much hardened compared with that before HIP with hardness about 400 HV. PWHT is necessary to recover both 9Cr-ODS and JLF-1 BMs to that before HIP with tempered martensitic structure. As shown in Figure 3-1, PWHT with a fast cooling rate of 36°C/min was carried out for the dissimilar-metal joint. Normalization (N) was executed at 1050°C for 1h, followed by tempering (T) at 720-820°C for 1h. After PWHT with normalization, both 9Cr-ODS and JLF-1 was hardened (Figure 3-3 (a)), this means quenched martensite induced for both 9Cr-ODS and JLF-1 (about 10^3 s was taken after cooling down from 1050°C normalization in the CCT diagram in Figure 3-2 (a)). After the following tempering, as temperature increases,

hardness slightly decreases, as shown in Figure 3-3 (a). The tempering temperature at 740-780°C is proper for the hardness recovery without obvious softening of the BMs. The optimum PWHT condition was chosen to be 1050°C×1h + 780°C×1h. In this case, the hardness of JLF-1 BM was recovered the most close to that before HIP.

As shown in Figure 3-3 (b), the grain size of JLF-1 BM increased after the HIP, and increased further after the following PWHT with normalization. However, the grain size of 9Cr-ODS BM did not change during the HIP and PWHT process; this may be due to high density nano-scale oxide particles in the matrix which impeded the growth of grains[105].
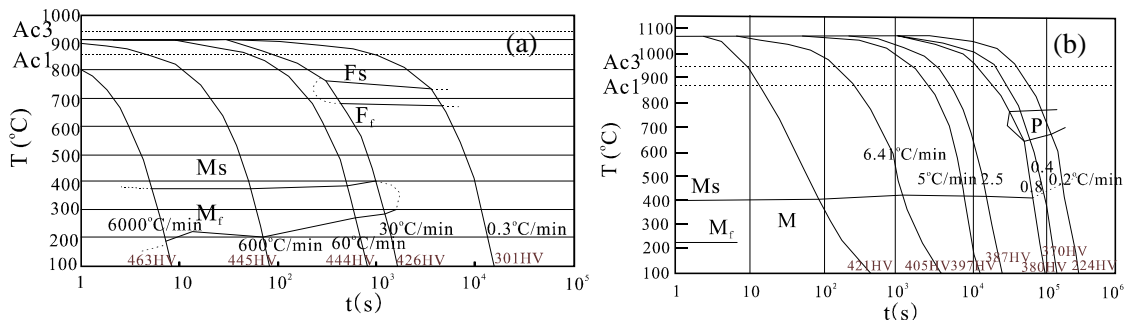
Figure 3-2 Reproduced continuous cooling transformation (CCT) diagram for (a) 9Cr-ODS[106] and (b) RAFM steel[107].
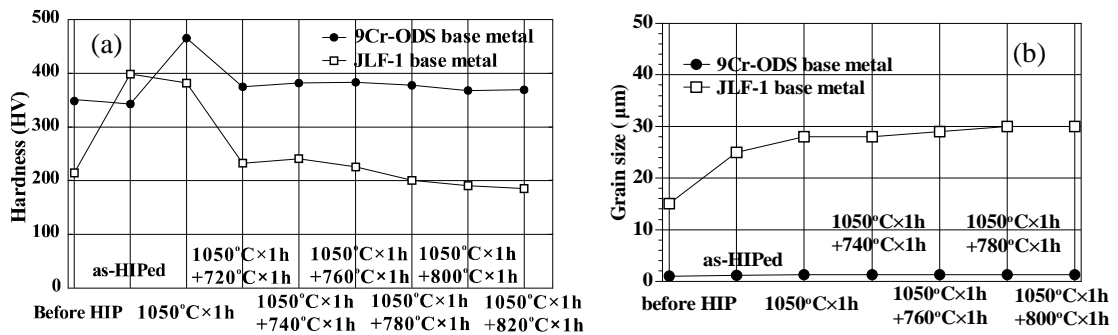
Figure 3-3 (a) Hardness and (b) grain size evolution of the BMs before and after PWHT.

Figure 3-4 shows the SEM microstructure of the BMs after the HIP and PWHT procedure. The as-received materials of 9Cr-ODS and JLF-1 (before HIP) are tempered martensite with carbides (mainly $M_{23}C_6$) on the grain and lath boundaries. After HIP at

1000°C, quenched martensite formed in the JLF-1 BM, coincident with the assumption by the CCT diagram in Figure 3-2. No carbides existed on lath and grain boundaries. However, there are coarse carbides in the 9Cr-ODS BM. The similar coarse carbides were also observed by S. Noh et al.[72] in the single-metal bonding of 9Cr-ODS by HP at 1150°C under 25 MPa for 60 min with the same cooling rate of 5°C/min. The coarse carbides found in the present work are 150-400 nm long, 60-180 nm wide, gathered on the grain boundaries. The clusters with several carbides together are 0.15-1.8 µm in size, comparable to the grain size of 9Cr-ODS. The formation of coarse carbides may be due to the slow cooling rate after the HIP process. The cooling rate of the following PWHT was increased to 36°C/min which is to be expected to recover the microstructure to tempered martensite with mainly $M_{23}C_6$ carbides. After PWHT with normalization at 1050°C for 1h with the fast cooling rate, the microstructure of both 9Cr-ODS and JLF-1 BMs is quenched martensite with elements dissolved into the matrix. After the following tempering at 780°C for 1h, the microstructure of both BMs has recovered to tempered martensite with $M_{23}C_6$ carbides on grain and lath boundaries.

TEM images of the BMs before HIP, after HIP, and after the following PWHT with N&T are listed in Figure 3-5. It can be seen that, before HIP, it is tempered martensitic structure for 9Cr-ODS BM with high-density nano-scale oxide particles, carbides, and dislocations. For JLF-1 BM, the structure is also tempered martensite with carbides and dislocations. However, after HIP at 1000°C with the slow cooling rate of 5°C/min, the 9Cr-ODS BM is ferritic structure with few dislocations but still high density dispersions of nano-scale oxide particles; The JLF-1 BM is quenched martensite with high-density tangled dislocations and without carbides. While after PWHT with N&T, the microstructure of both 9Cr-ODS and JLF-1 has recovered to that before HIP with tempered martensitic structure of carbides and dislocations. The nano-scale oxide particles still kept high density in the matrix of 9Cr-ODS BM.

	9Cr-ODS BM	JLF-1 BM
Before HIP		
As-HIPed		
1050°C×1h		
1050°C×1h +780°C×1h	5μm	
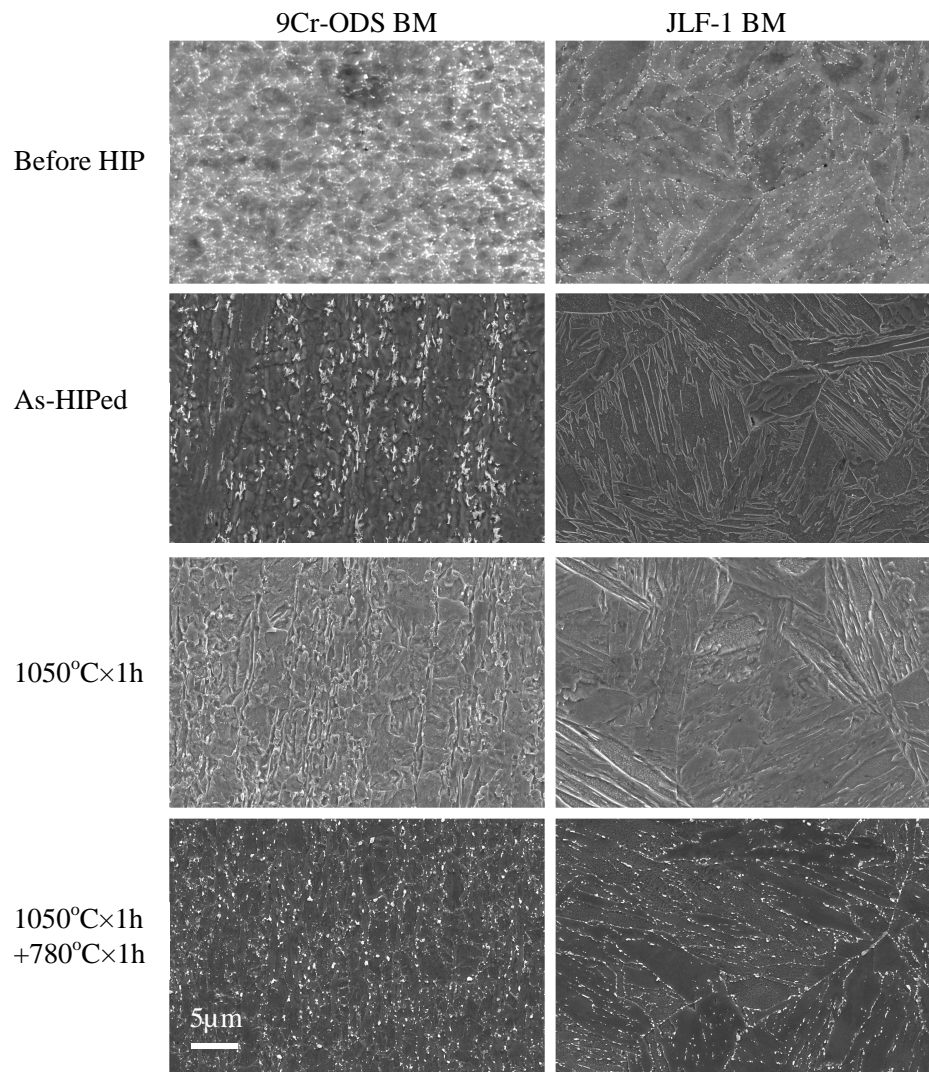
Figure 3-4 SEM microstructure of 9Cr-ODS and JLF-1 BMs.

	9Cr-ODS BM	JLF-1 BM

As-received

As-HIPed

PWHT: N&T
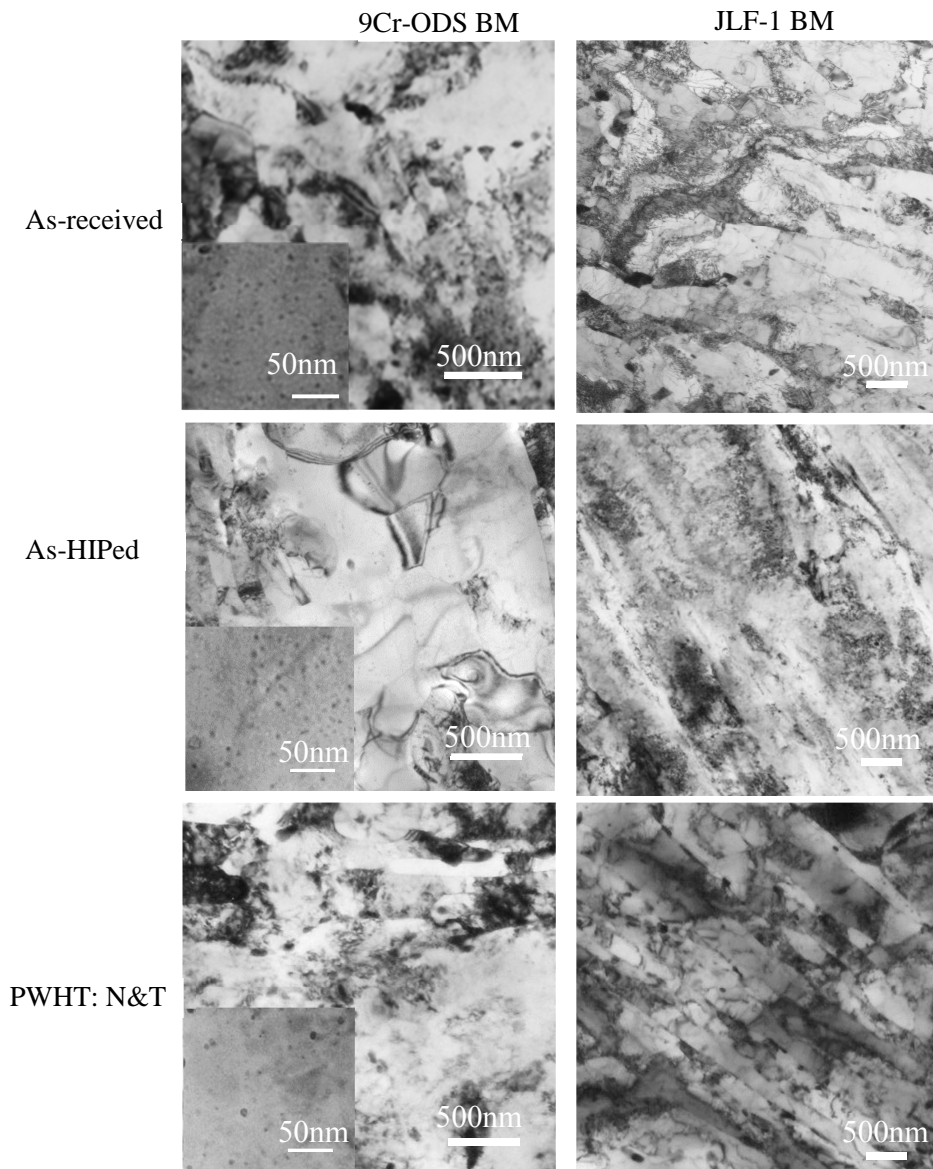
Figure 3-5 TEM images of 9Cr-ODS and JLF-1 BMs.

Figure 3-6 depicts the solution curve of $M_{23}C_6$ carbides in steels. The carbon content in 9Cr-ODS (0.14%) is higher than that in JLF-1 steel (0.09%), and the high number density of nano-oxide dispersions in 9Cr-ODS may impede the decomposition of $M_{23}C_6$ carbides, thus the complete decomposition temperature of $M_{23}C_6$ carbides for 9Cr-ODS ($>1100^{o}$C) is much higher than that for JLF-1 ($<1000^{o}$C). Therefore, during the 1000°C-HIP, $M_{23}C_6$ carbides were already completely decomposed in JLF-1 BM. Its microstructure is quenched martenste without any carbides. However, for 9Cr-ODS,

during the 1000°C-HIP, $M_{23}C_6$ was not completely decomposed. There were still some carbides remaining in the 9Cr-ODS BM. During the slow cooling with 5°C/min, the residual $M_{23}C_6$ carbides can be nucleation sites to form the coarse carbides with irregular shape as shown in Figure 3-4. After the PWHT with N with rapid cooling, both 9Cr-ODS and JLF-1 was quenched martensite. There may be still a few residual $M_{23}C_6$ carbides in 9Cr-ODS. However because of the rapid cooling rate, there was no chance for the residual carbides to be nucleation sites to form coarse carbides. After the following tempering, new $M_{23}C_6$ carbides formed in both 9Cr-ODS and JLF-1 BMs. The microstructure of them was recovered to that before HIP with tempered martensite (the lath width in JLF-1 is larger than that before HIP). The above mentioned microstructure evolution of 9Cr-ODS and JLF-1 BMs was illustrated in Figure 3-7 and summarized in Table 3-1.
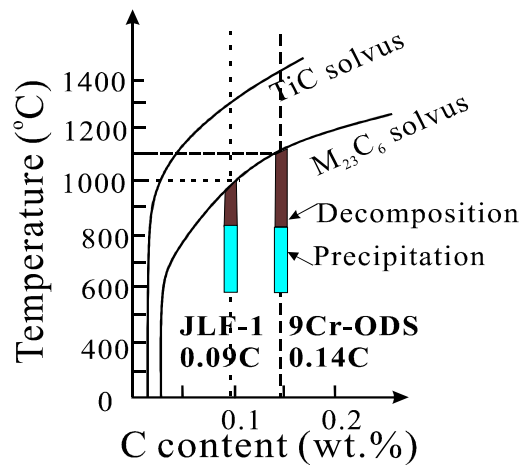
Figure 3-6 Solution curve of $M_{23}C_6$ carbides in steels, produced referring to[108][109].
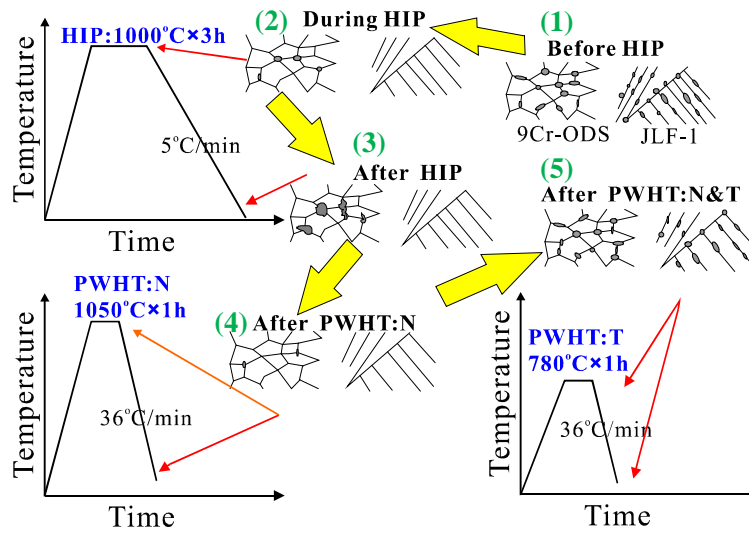
Figure 3-7 Schematic of the formation of microstructure in 9Cr-ODS and JLF-1 BMs during the process of HIP and PWHT.

Table 3-1 Summary of microstructure evolution of 9Cr-ODS and JLF-1 BMs during the 1000°C-HIP and the following PWHT.

BM	Before HIP	During 1000°C-HIP	After HIP	After PWHT: N	After PWHT: N&T
9Cr-ODS	Tempered martensite	Incomplete decomposition of carbides	Ferrite + coarse carbides	Quenched martensite	Tempered martensite
JLF-1	Tempered martensite	Complete decomposition of carbides	Quenched martensite	Quenched martensite	Tempered martensite

3.1.2 Effect of HIP temperature

Figure 3-8 depicts the hardness evolution for the joints HIPed at different temperatures from 1000 to 1100°C. Hardness before HIP is about 350 HV for 9Cr-ODS, 210 HV for JLF-1. HIP always induced quenched martensite for JLF-1 with hardness of above 400 HV. HIP at 1000°C induced a little softening for 9Cr-ODS BM. However, HIP at higher temperatures of 1050°C and 1100°C also resulted in hardening for 9Cr-ODS BM. As mentioned in Section 3.1.1, the microstructure for JLF-1 after HIP at 1000°C with the slow cooling rate is quenched martensite, and is ferrite for 9Cr-ODS BM. HIP at higher temperatures of 1050°C and 1100°C for 9Cr-ODS induced more decomposition of $M_{23}C_6$ carbides than HIP at 1000°C. Thus, more elements were dissolved into matrix,

and quenched martensite also occurred for 9Cr-ODS to induce hardening after the higher-temperature HIP conditions. After PWHT with normalization (N) with rapid cooling rate, both 9Cr-ODS and JLF-1 BMs was hardened. While after the following PWHT with normalization and tempering (N&T), the hardness of both 9Cr-ODS and JLF-1 BMs recovered to that before HIP.

Note that, the interface is soft for all the as-HIPed joints. For the 1000°C-HIP joint, the interface is still soft even after PWHT with N or N&T. After PWHT with N, for the joints HIPed at higher temperatures of 1050°C and 1100°C, the hardness of the interface is comparable to that of JLF-1 BM. While after PWHT with N&T, the hardness of the interface is not the smallest any more. Instead, JLF-1 BM is the softest.
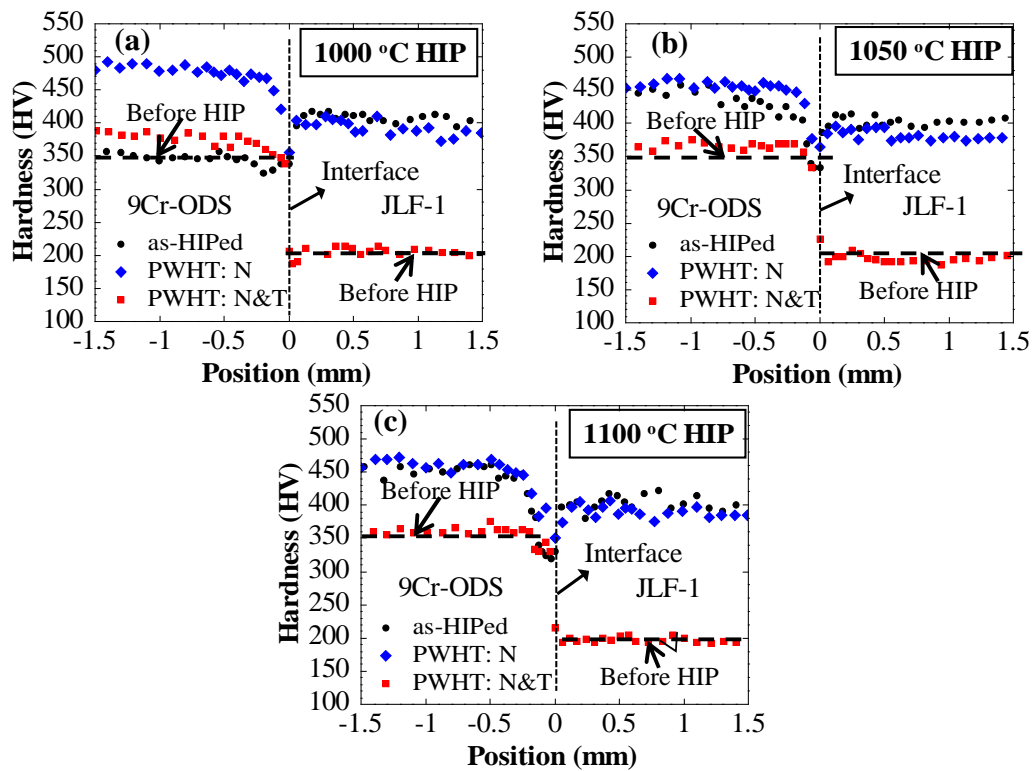
Figure 3-8 Hardness of the joints between 9Cr-ODS and JLF-1 HIPed at (a) 1000°C, (b) 1050°C, and (c) 1100°C. PWHT: N—normalization (1050°C×1h), N&T—normalization+ tempering (1050°C×1h+780°C×1h).

Figure 3-9 shows the tensile results of the joints. The hardness distribution of the joints depicted in Figure 3-8 has an important relationship with the fracture behavior during tensile tests. The tensile specimens fractured at the softest site. For the 1000°C-

HIP joint, after PWHT with N or N&T, the tensile specimen fractured at the interface (i.e. the softest site) before yield point with brittle facture mode. The fracture strength is about 32% of the yield strength of 9Cr-ODS BM. The 68% reduction in strength is not coincident with the 14% reduction in hardness at the soft layer near the interface as shown in Figure 3-8 (a). This means that, 1000°C is too low to bond well the joint even after PWHT. There may be un-bonded areas existed at the interface for the 1000°C-HIP joint. The un-bonded areas can induce much high stress at the interface. It was assumed spherical voids. For the specimen after PWHT with N&T, the tensile stress at the fracture, 370 MPa, can induce 3 times more stress, 1110 MPa, which can be comparable to the yield strength of the 9Cr-ODS BM, 1172 MPa[56].

However, for the joints HIPed at higher temperatures of 1050°C and 1100°C, the tensile specimens fractured on the 9Cr-ODS side at the interface after yield point with ductile mode. The tensile property was summarized in Table 3-2. The 1050°C-HIP joint showed the best bonding strength and reduction of area. HIP at 1100°C decreased the bonding strength may be due to grain coarsening of JLF-1 as also shown in Table 3-2. After PWHT with N, the specimens still fractured at interface when tested at 550°C, but fractured at the JLF-1 BM at RT. After PWHT with N&T, all the specimens fractured outside the interface at JLF-1 the BM at both RT and 550°C. PWHT with normalization followed by tempering was believed to further improve the bonding property of the joints.
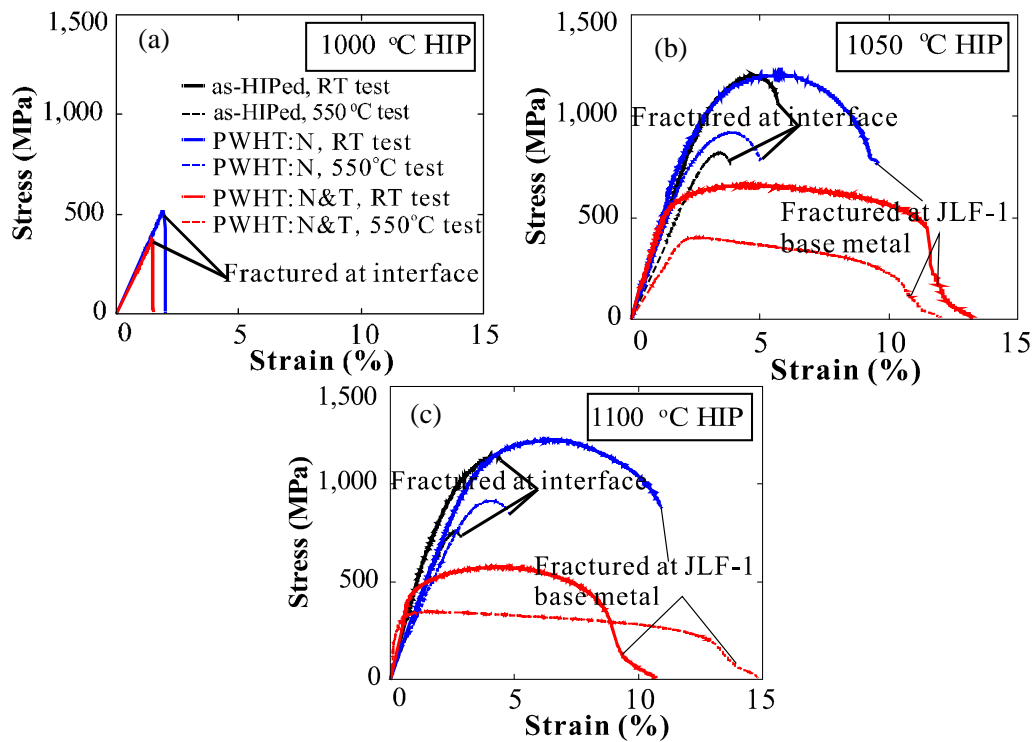
Figure 3-9 Tensile curves of the HIP joints

Table 3-2 Tensile properties of the HIP joints fractured at the interface.

HIP temperature	Condition	Test temperature	Bonding strength	Reduction of area	JLF-1 grain size
1000°C	PWHT: N	RT	520 MPa	7.3%	28μm
	PWHT: N&T	RT	370 MPa	9.8%	
1050°C	as-HIPed	RT	1200 MPa	39%	30μm
	as-HIPed	550°C	820 MPa	43%	
	PWHT: N	550°C	920 MPa	64%	
1100°C	as-HIPed	RT	1140 MPa	15%	45μm
	as-HIPed	550°C	755 MPa	15%	
	PWHT: N	550°C	915 MPa	33%	

Macroscopic fracture surfaces of the joints are shown in Figure 3-10. It can be seen that, the 1000°C-HIP joint after PWHT with N and N&T fractured at the interface. The fracture surfaces are flat and no necking with brittle characteristic. However, the microstructure of the fracture surfaces shows ductile characteristic, as shown in Figure 3-11(a). Lots of particles existed in the shallow dimples. The particles are of Y-Ti-O type detected by energy dispersive X-ray spectroscopy (EDS). For the 1050°C- and 1100°C-

HIP joints, they also fractured at the interface. Y-Ti-O particles were also detected in the dimples. As shown in Figure 3-10, the fracture surfaces showed ductile characteristic with necking. The microstructure of the fracture surfaces are inter-granular mode for the 1050°C-HIP joint (Figure 3-11 (b)), and cleavage and sallow dimples for the 1100°C-HIP joint (Figure 3-11(c)). The ductility of the 1050°C-HIP joint is better than that of the 1100°C-HIP joint. For the joints after PWHT, they fractured at the JLF-1 BMs, the fracture surfaces showed excellent ductility with necking (Figure 3-10) and deep dimples (Figure 3-11 (d)).
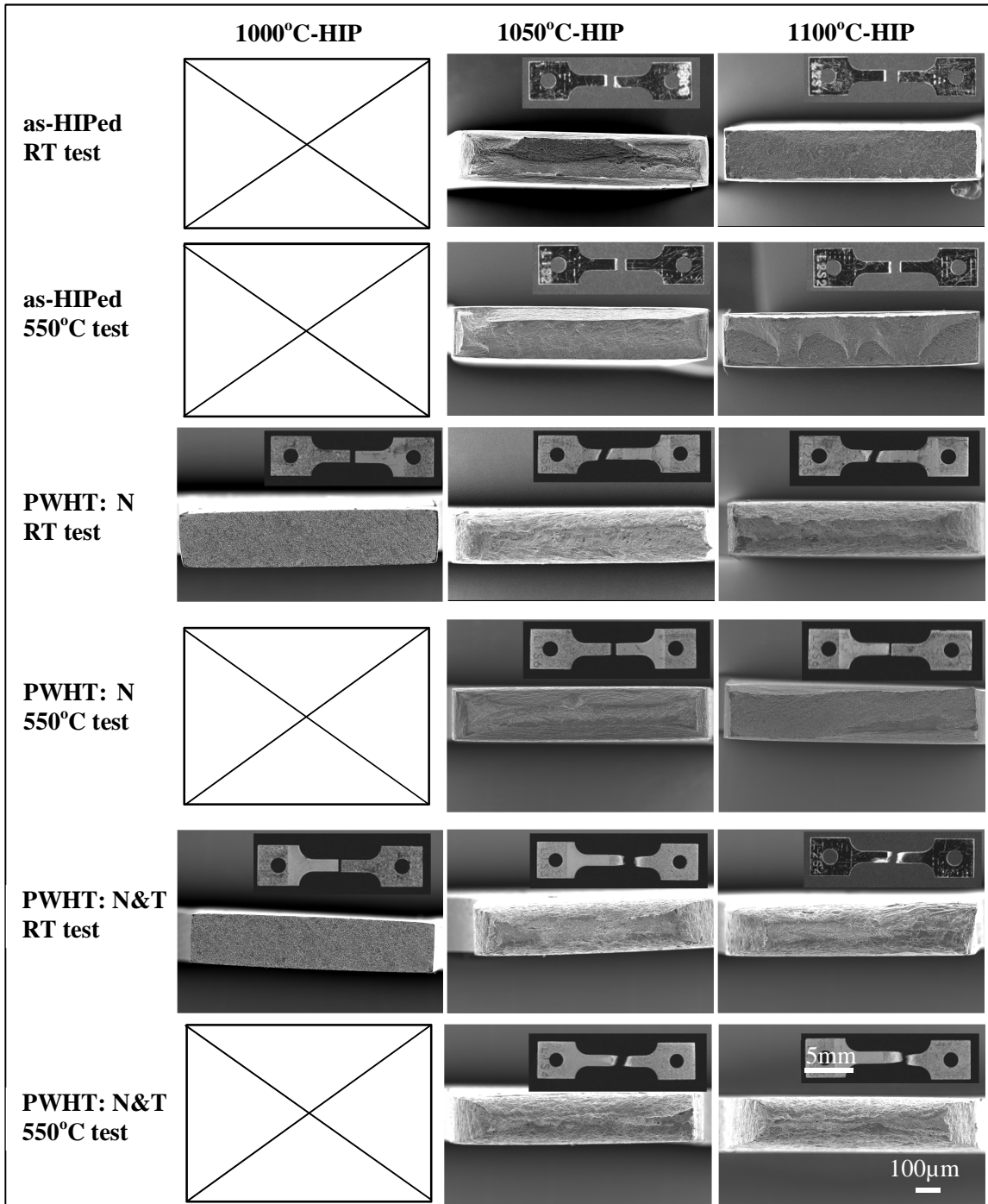
Figure 3-10 Macrostructure of the fracture surfaces for the joints at different HIP and PWHT conditions.
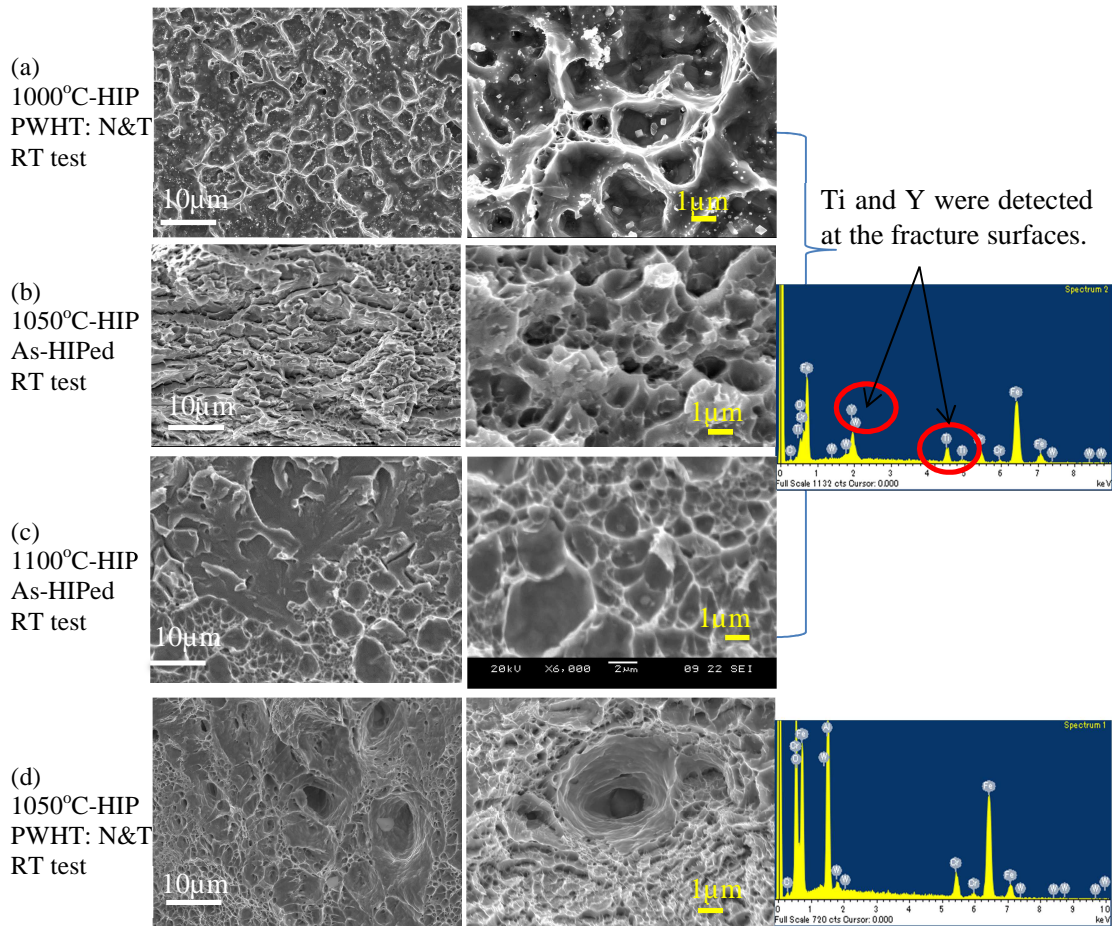
Figure 3-11 Microstructure of the tensile fracture surfaces.

Figure 3-12 depicts the microstructure across the interfaces taken by SEM. It is shown that, for all the as-HIPed conditions, quenched martensite without any carbides appeared on the JLF-1 side, while coarse carbides on the 9Cr-ODS side. As the HIP temperature increased, the density and size of coarse carbides decreased. HIP at higher temperatures induced more decomposition of $M_{23}C_6$ carbides for 9Cr-ODS BM, more elements have dissolved into matrix, and quenched martensite formed, thus the hardness of the 9Cr-ODS BM after HIP at 1050^oC and 1100^oC was much higher than that HIPed at 1000^oC. While after PWHT with N&T, all the joints across the interfaces have recovered to tempered martensite with normal carbides (mainly $M_{23}C_6$) on lath and grain boundaries.

	As-HIPed	PWHT: N&T
1000°C-HIP	(a) 9Cr-ODS | JLF-1	(b) 9Cr-ODS | JLF-1
1050°C-HIP	(c)	(d)
1100°C-HIP	(e) 5μm | Interface	(f) Interface
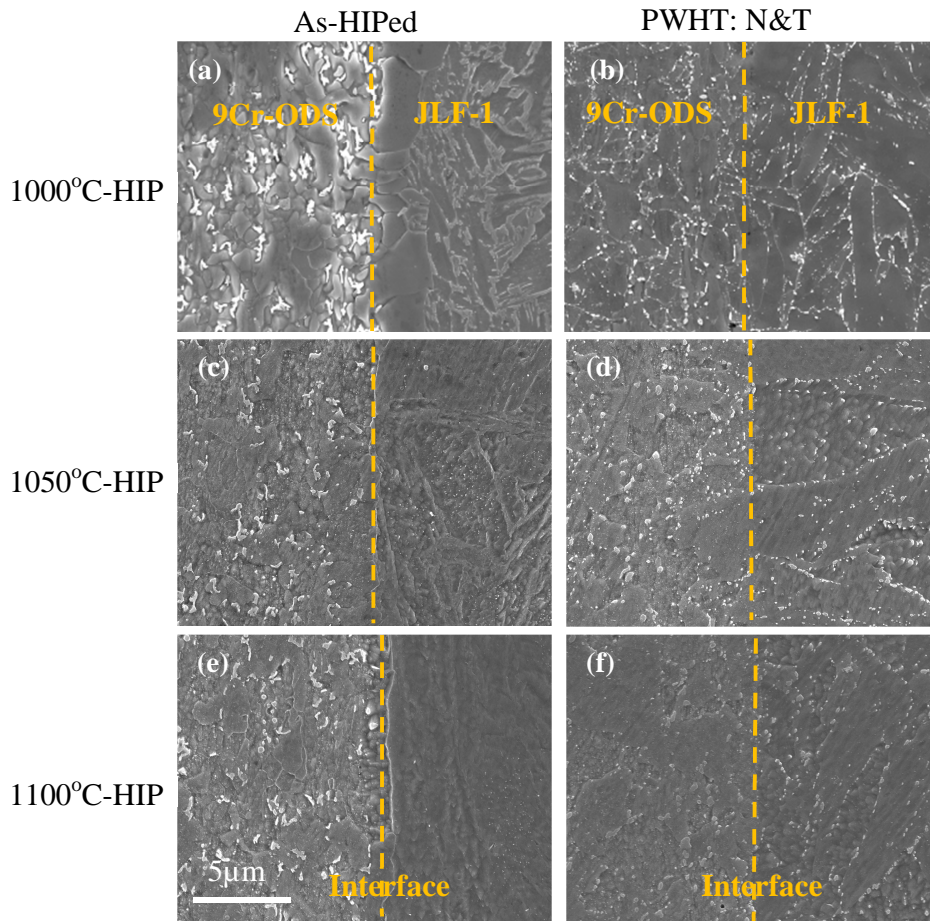
Figure 3-12 SEM microstructure of the interfaces HIPed at different temperatures before and after PWHT with N&T

A few-particle layer was found at the interface on the JLF-1 side while HIP at 1000°C, as shown in Figure 3-12 (a) and Figure 3-13, which contains almost no MX particles. It seems to be ferritic structure, different from the JLF-1 BM of quenched martensite with MX particles in the laths. This ferritic structure with lower hardness and with width of 50 μm was also found by Hirose et al.[77] at the interface for a dissimilar-metal joint between W and F82H made by spark plasma sintering (SPS). However, formation mechanism of the ferrite layer has not been explained yet in their work. In the present work, the formation of the few-particle layer may be due to decarburization when heating in vacuum during the HIP. Thus softening was induced there at the interface. Enhancement of carbon diffusion and carbides decomposition at higher HIP temperatures of 1050°C and 1100°C is effective to homogenize carbon distribution and eliminate this few-particle layer, as shown in Figure 3-12.
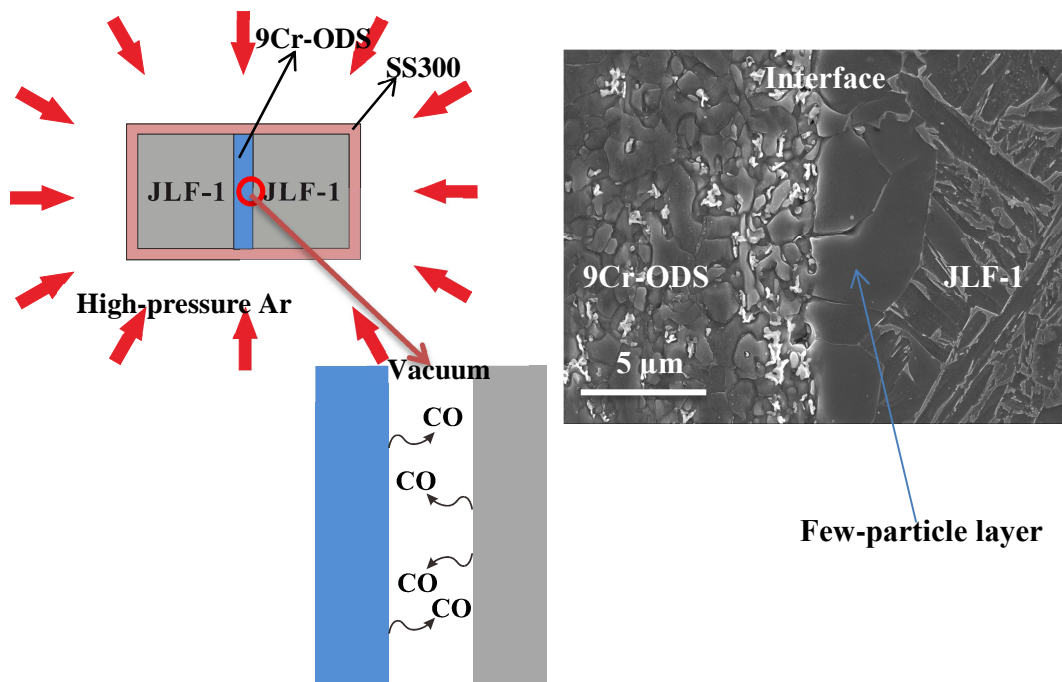
Figure 3-13 A few-particle layer was found when HIP at $1000^{o}C$, which might be induced by decarburization during the HIP process.

Why the interface is soft? For all the as-HIPed joints, the specimens always fractured on the 9Cr-ODS side at the interface due to local softening. Figure 3-14 and Table 3-3 depict the size distribution, mean size, and density of coarse carbides in 9Cr-ODS at BM and at the interface after HIP at different temperatures. It can be seen that, for all the HIP conditions, coarse carbides with size >0.6 µm are more at the interface than at the BM. This means that, at the interface, the decomposition of $M_{23}C_6$ carbides is less than that in the BM. Therefore, the interface is soft. During tensile tests, the specimens fractured at the soft area at 9Cr-ODS near interface.

As illustrated in Figure 3-15, before HIP, 9Cr-ODS and JLF-1 are tempered martensitic structure with $M_{23}C_6$ carbides. There are also rough surfaces for the materials before HIP. For the $1000^{o}C$-HIP, the temperature is too low. There may be un-bounded areas after HIP due the incomplete contact of the rough surfaces. The following PWHT cannot even "heal" the un-bonded areas. These un-bonded areas can be crack initiation during tensile tests. On the other hand, the denser coarse carbides at 9Cr-ODS near the interface can also be potential fracture sites during tensile tests. However, as the HIP temperatures increased to $1050^{o}C$ and $1100^{o}C$, more decomposition of $M_{23}C_6$ carbides

occurred during the HIP, re-distribution of carbon happened at the interface, and the interface was bonded completely. Thus, after the higher-temperature HIP, the size of the coarse carbides decreased. The bonding strength was improved.
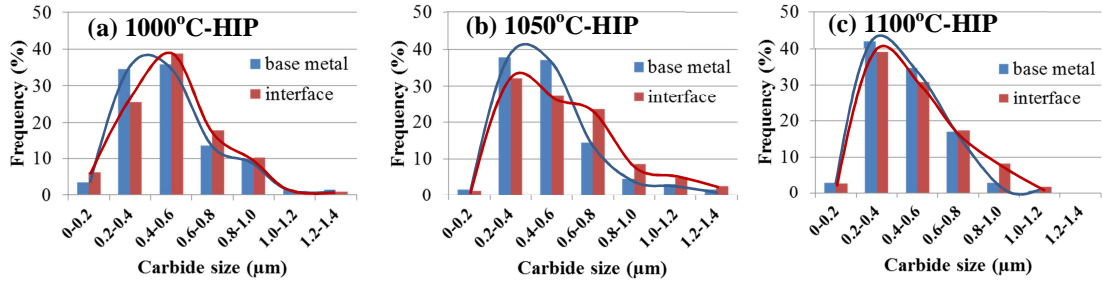
Figure 3-14 Size distribution of coarse carbides in 9Cr-ODS at BM and near the interface when HIP at (a) 1000^oC, (b) 1050^oC, and (c) 1100^oC.

Table 3-3 Size and density of coarse carbides in 9Cr-ODS at interface and BM.

HIP Temperature	Interface		BM	
	Density ($n/\mu m^2$)	Size (μm)	Density ($n/\mu m^2$)	Size (μm)
1000^oC	0.66	0.65	0.45	0.65
1050^oC	0.36	0.41	0.32	0.4
1100^oC	0.30	0.42	0.38	0.35

Figure 3-15 Schematic of carbides evolution after HIP at different temperatures.

The HIP temperature and cooling rate has significant influence on microstructure and hardness of 9Cr-ODS. S. Noh et al.[72] also have found coarse carbides in the single-metal joint of 9Cr-ODS when diffusion bonded by HP under a uniaxial pressure of 25 MPa at 1150°C for 1h with a cooling rate of 5°C/min (furnace cooling). The coarse carbides disappeared after the following PWHT with N&T with a fast cooling rate (air cooling). In this study, additional heat treatment at 800-1100°C for 3h was carried out for the as-received 9Cr-ODS with the cooling rate ranged from 0.5^{o}C/min to 36°C/min. The effect of temperature and cooling rate on hardness was investigated, as shown in Figure 3-16. The result showed that when the cooling rate is very slow as 0.5^{o}C/min, hardening can be never induced. The microstructure of 9Cr-ODS would be ferrite with coarse carbides. When the cooling rate is 5°C/min, the HIP temperature can be no less than 1050°C to obtain quenched martensitic structure for hardening. When the cooling rate is 36°C/min, the HIP temperature can be no less than 1000°C for quenched martensite. Next, the critical cooling rate would be investigated to get quenched martensite without any coarse carbides. Thus, the following PWHT with only tempering is necessary to recover the microstructure of 9Cr-ODS to tempered martensite. In this case, the PWHT with normalization to eliminate coarse carbides can be avoided to reduce the cost of the blanket fabrication in the future.
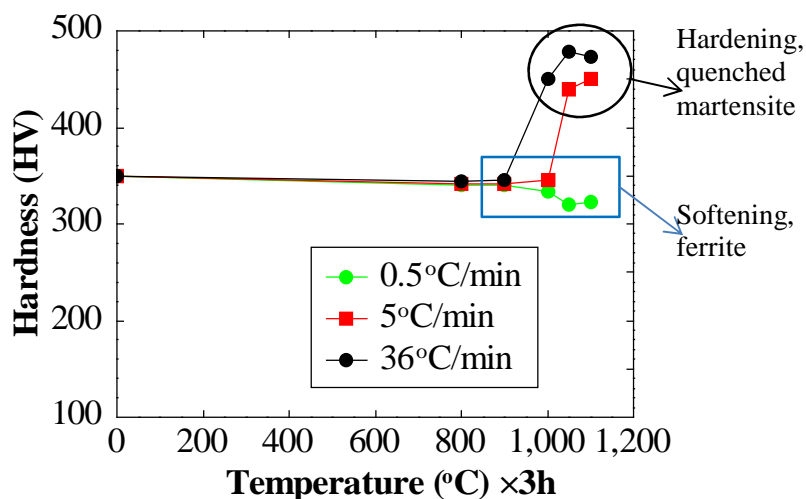
Figure 3-16 Effect of temperature and cooling rate on hardness of 9Cr-ODS.

Figure 3-17 depicts the microstructure evolution after PWHT for the joint HIPed at 1050°C. For the as-HIPed joint, the microstructure was quenched martensite without any carbides for JLF-1, and was quenched martensite with coarse carbides for 9Cr-ODS. The size of the carbides size was a little larger near the interface than that in the BM. After PWHT with normalization at 1050°C with fast cooling rate of 36°C/min, the carbides were almost decomposed and the elements were dissolved into the matrix. Both 9Cr-ODS and JLF-1 was quenched martensite without any coarse carbides. After the following tempering, new $M_{23}C_6$ carbides precipitated out. Thus, the microstructure of the whole joint was recovered to that before HIP with tempered martensite with $M_{23}C_6$ carbides on lath and grain boundaries.
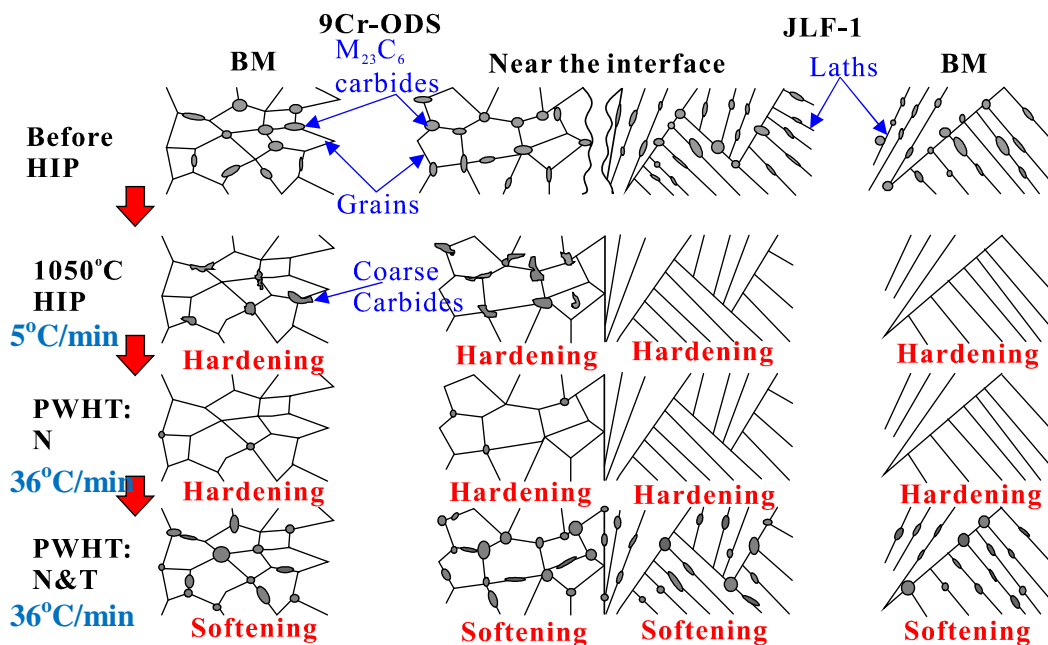
Figure 3-17 Schematic of microstructure evolution after PWHT.

Furuya et al.[110] have investigated the diffusion bonding of F82H by HIP at 1040°C under the pressure of 150 MPa for 2h followed by PWHT with tempering at 740°C for 2h. Grain coarsening and large inclusions were found at the interface. This induced deterioration of impact property of the joint. The large inclusions at the interface are similar to the coarse carbides in this study, which may be formed due to contamination before HIP. It was suggested that surfaces cleaning and grain refining is very important to improve toughness of the HIP joints.

There are also research work of dissimilar-metal bonding between ODS Eurofer and Eurofer by HIP in Europe. Comparison between the activity in Europe and this work is shown in Table 3-4. The HIP temperature range is almost the same but under different pressure. The optimum HIP temperature to get the best bonding property was at 1100°C in the Europe work, larger than that in this study, 1050°C. However, the former was under lower pressure of 150 MPa than the latter (191 MPa) to achieve the similar bonding effect. During the following PWHT process, normalization was carried out at 1040°C for avoiding the grain coarsening of Eurofer steel, similar to that at 1050°C for JLF-1. Systematic PWHT has not been studied for the activity in Europe yet. However, in this work tempering after normalization was investigated systematically for the hardness recovery of the BMs of 9Cr-ODS and JLF-1. The optimum bonding condition for the activity in Europe is HIP at 1100°C for 3h under 100 MPa, followed by PWHT at 1040°C for normalization and at 740°C for tempering. The optimum bonding condition in this work is HIP at 1050°C for 3h under the pressure of 191 MPa, followed by PWHT at 1050°C for normalization and at 780°C for tempering.

For the Europe activity, more mechanical properties evaluation such as tensile, impact tests was carried out. In this study the microstructural evolution at different positions at BMs and near the interface at different HIP temperatures and different PWHT conditions was investigated in detail. The microstructural characterization is effective to understand the bonding mechanism and to provide guidance to improve the bonding properties. For example, in the future for the large component fabrication of the blanket structure with HIP, besides proper higher HIP temperature, fast cooling rate is also necessary to keep the formation of coarse carbides which would deteriorate the bonding properties. If slow cooling rate is unavoidable, appropriate PWHT should be executed to redeem bonding properties of the joints.

Table 3-4 Comparison of the present work with the similar work in Europe.

	In Europe[63]	In this work
Dissimilar-metal joint	ODS Eurofer—Eurofer	9Cr-ODS—JLF-1
HIP investigation	980-1100°C×3h×100MPa	1000-1100°C×3h×191MPa
PWHT investigation	980-1040°C×30min +750°C×2h	1050°C×1h+720-780°C×1h
Mechanical properties	Tensile (RT, 700°C)	Tensile (RT, 550°C)

	Charpy impact test	
Optimum bonding condition	HIP: 1100°C×3h×100MPa PWHT:1040°C×30min+750°C×2h	HIP: 1050°C×3h×191MPa PWHT: 1050°C×1h+780°C×1h
Comments	More mechanical properties evaluation was carried out, such as creep, impact tests.	Microstructure evolution during HIP and the following PWHT was investigated in detail.

3.2 The EBW joint of 9Cr-ODS steel—JLF-1 steel

3.2.1 Characterization of weld metal and heat-affected zones

Figure 3-18 shows the microstructure of the EBW joint in as-welded condition. The WM is about 0.8 mm in width. It is mainly quenched martensite with (Y, Ti)-rich particles. Some δ-ferrite also exists in the WM occasionally. The illustration of formation of the WM is shown in Figure 3-19. The quenched martensite and δ-ferrite were formed by rapid cooling from very high temperature after EBW. The width of the HAZs of both 9Cr-ODS and JLF-1 is about 0.3 mm. The HAZs are also quenched martensitic structure. The carbides in the HAZs are coarser and fewer than in the BMs because they are going to be decomposed at the temperature influence during welding.

Table 3-5 Phase transformation temperatures for RAFM steel from DSC results[111].

Transformation reaction	Temperature (^{o}C) estimated from DSC
α→α+γ	831
α+γ→ γ	877
γ→ δ+ γ	1302
δ+ γ→ δ	1457
δ→ δ+ L (Liquid)	1480
δ+ L (Liquid) → L (Liquid)	1532

S. Sam et al.[111] have investigated the δ-ferrite in the WM of RAFM steel. The transformation temperatures from differential scanning calorimetry (DSC) are shown in Table 3-5. δ-ferrite is formed at high temperature above 1302°C. The hardness at

different positions in the joint of the present study is shown in Table 3-6. The hardness of δ-ferrite in the center of the WM is higher than that near the fusion boundary.
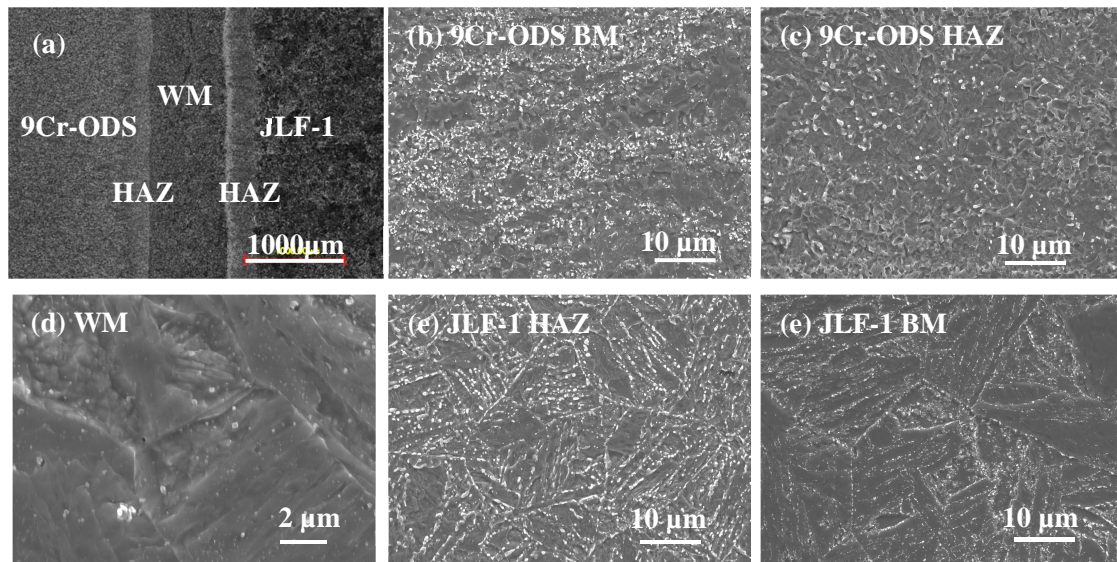
Figure 3-18 Microstructure of the as-welded EBW joint between 9Cr-ODS and JLF-1.
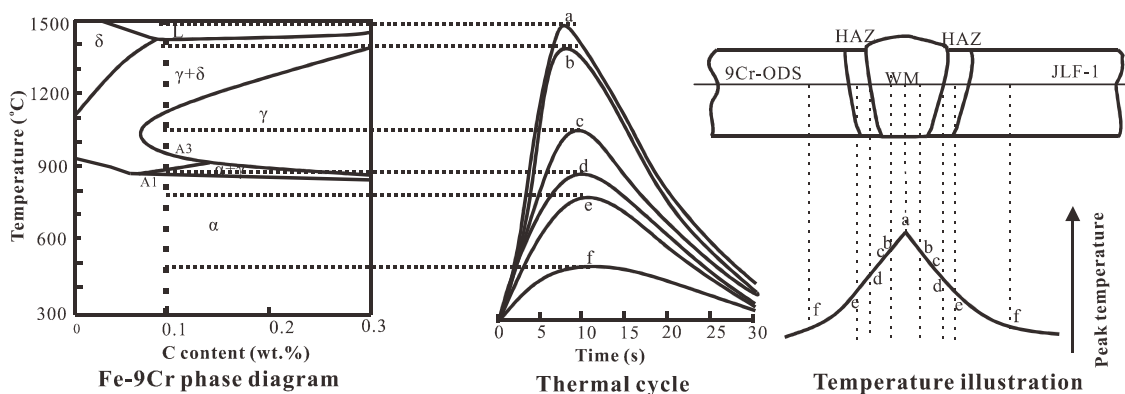
Figure 3-19 Fe-9Cr phase diagram reproduced from[112], thermal cycle, and temperature illustration of 9Cr-ODS—JLF-1 joint during EBW.

Table 3-6 Hardness at different positions of the EBW joint between 9Cr-ODS and JLF-1.

Position	Microstructure	Hardness (HV)
WM	Quenched martensite	420
	δ ferrite (at center)	378
	δ ferrite (near fusion boundary)	330
HAZs	Quenched martensite with carbides decomposition, 9Cr-ODS	481
	Quenched martensite with carbides decomposition, JLF-1	440
BMs	BM of 9Cr-ODS	350

3.2.2 Effect of PWHT

Two kinds of PWHT were carried out for the EBW dissimilar-metal joint between 9Cr-ODS and JLF-1. One is only tempering (T), as shown in Figure 3-20 the microstructure; more carbides arise for HAZs of 9Cr-ODS and JLF-1. And the δ-ferrite still remained in the WM. Another PWHT is normalization at $1050^{o}C$ for 1h followed by tempering at $780^{o}C$ for 1h (N&T). In this case, the carbides in HAZs are smaller than the above mentioned PWHT with only tempering, and the ferritic structure disappeared. The normalization process is helpful to decompose the carbides, make the elements dissolve into matrix, and transfer the microstructure of whole joint into quenched martensite. After the following tempering, new carbides precipitated out. Thus the carbides in the HAZs are smaller than that in the before-mentioned PWHT with only tempering.
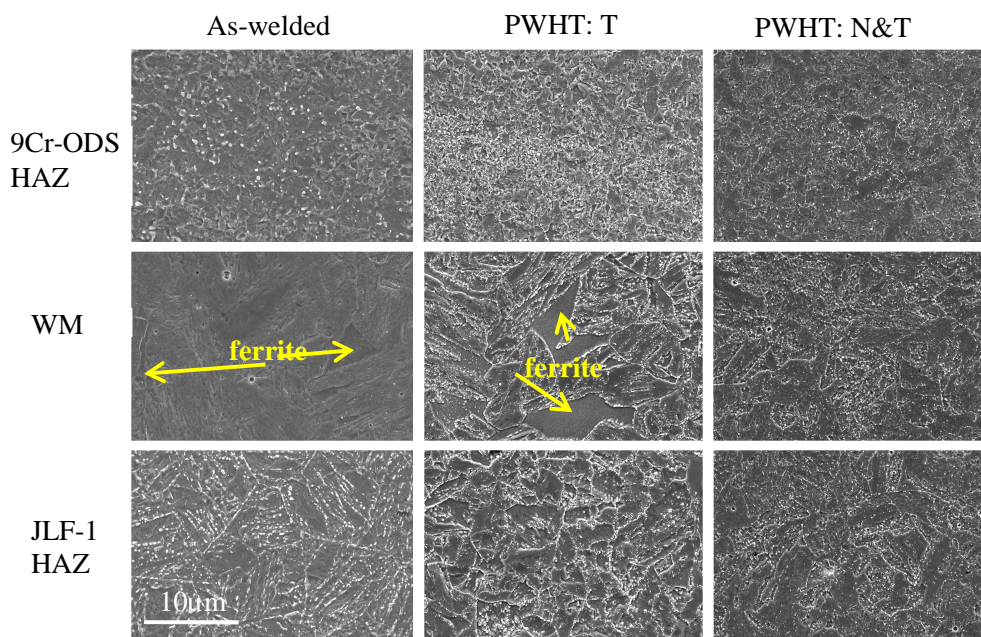
Figure 3-20 Microstructure of the joint in the conditions of PWHT with only tempering and PWHT with N&T.
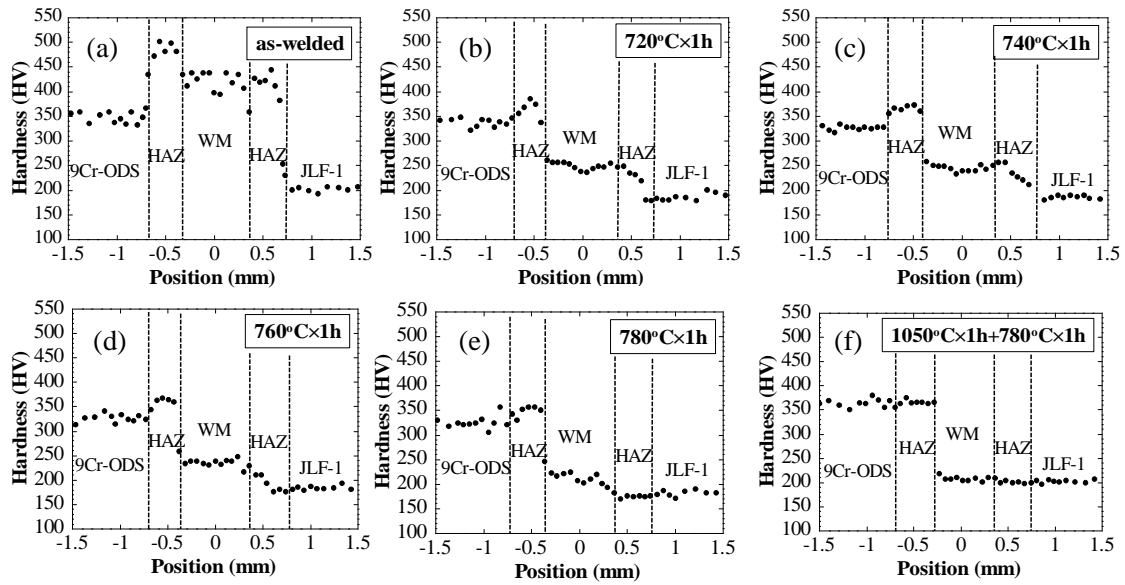
Figure 3-21 Hardness of the EBW joint at different PWHT conditions.

Figure 3-21 shows the hardness evolution of the EBW joint. Hardness before EBW is about 350 HV for 9Cr-ODS and 210 HV for JLF-1. Hardening was induced for the WM and HAZs after EBW. During the following PWHT, as the tempering temperature increased, the hardening of the WM and HAZs decreased. After tempering at $780^{\circ}C\times1h$, the hardening was almost relieved. However, softening of BMs was caused. As shown in Table 3-7, hardness was decreased to 327 HV for 9Cr-ODS BM, to 185 HV for JLF-1 BM. Another kind of PWHT with N&T, as shown in Figure 3-21 (f) and Table 3-7, is useful to avoid softening of BMs, and keep the hardness of WM, HAZ, and BM of JLF-1 similar to that of JLF-1 before EBW in a flat level, and the hardness of HAZ and BM of 9Cr-ODS similar to that of 9Cr-ODS before EBW as well.

Table 3-7 Mean hardness of the EBW joint at different positions and under different conditions.

Condition		9Cr-ODS BM	9Cr-ODS HAZ	WM	JLF-1 HAZ	JLF-1 BM
As-welded		350	479	418	418	210
PWHT: T	$720^{\circ}C\times1h$	338	364	250	233	189
	$740^{\circ}C\times1h$	327	365	245	230	186
	$760^{\circ}C\times1h$	327	360	237	204	184
	$780^{\circ}C\times1h$	327	346	210	175	185
PWHT:N&T	$1050^{\circ}C\times1h$ $+780^{\circ}C\times1h$	366	365	208	200	202

Tensile tests of the dissimilar-metal joint were carried out at RT and 550°C. The engineering strain-stress curves are shown in Figure 3-22. All the specimens fractured at JLF-1 BM after tensile tests. Table 3-8 summarized the tensile properties of the joint under different conditions. PWHT with tempering at 780°C×1h showed lower strength than the as-welded because of softening of JLF-1 BM. However PWHT with normalization and tempering (N&T) improved the strength. Because the specimens fractured not at the WM, but at the BM of JLF-1, the bonding strength cannot be obtained by uniaxial tensile tests. It is estimated lager than the ultimate tensile strength of JLF-1 BM. It is necessary to make the better estimation of the bonding strength to provide the margin of the bonding strength compared to the strength of BM (how much the bonding strength is larger than the strength of BM). This can make sure the safety of structure if the joint is located at higher load condition (more stress concentration than the BM). Besides the bonding strength, the parameter of plastic strain in the WM is also an important parameter for the blanket structure. The plastic strain in the WM cannot be obtained by uniaxial tensile tests, but can be obtained by four-point bend tests (which can concentrate the stress inside the inner span including the WM) combined with finite element method (FEM) simulation. This will be introduced in Chapter 4.
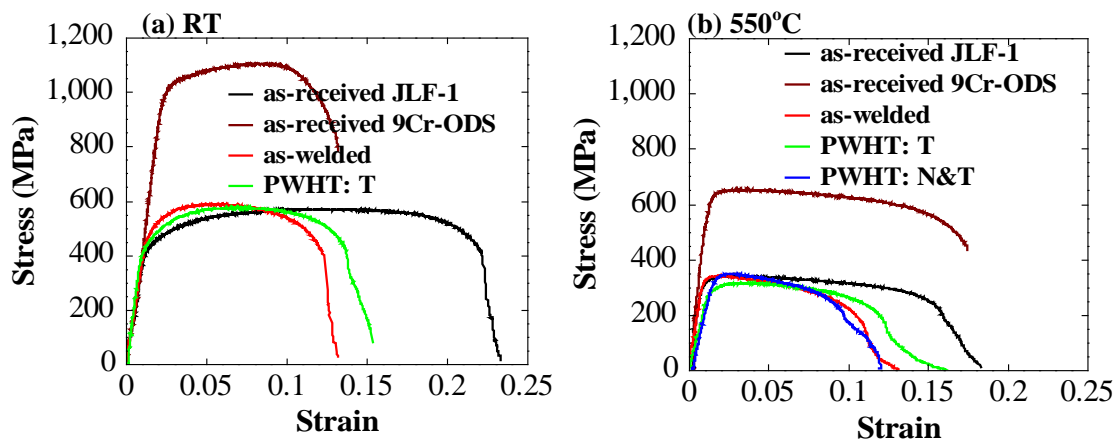
Figure 3-22 Tensile curves of the EBW joint at RT and 550°C.

Table 3-8 Tensile properties of the EBW joint under different conditions.

Condition	Test temperature	Total elongation (%)	Reduction of area (%)	Yield strength (MPa)	Ultimate tensile strength (MPa)
As-welded	RT	12	78	500	590
As-welded	550°C	11	90	330	340
PWHT:T	RT	16	79	450	580
PWHT:T	550°C	15	87	300	320
PWHT:N&T	550°C	12	84	305	350

L. Commin et al.[90] have developed a dissimilar-metal joint between ODS Eurofer and Eurofer by EBW. In their work, two conditions of PWHT were studied, i.e. tempering at 770°C for 2h (T), and normalization at 1050°C for 1h and tempering at 770°C for 2h (N&T), similar to the PWHT conditions in the present work. In this work, the hardness evolution as tempering temperature increased was studied more systematically. 780°C for tempering is a proper PWHT condition to eliminate hardening in the WM and HAZs. However, it induced softening of BMs. In L. Commin et al.'s work, the hardness of ODS Eurofer BM was decreased by 120 HV. The hardness of 9CrODS BM was decreased by only 20 HV in this work. PWHT with N&T is effective to keep the strength of BMs. The hardness of 9Cr-ODS and JLF-1 BMs can be kept in the same level as that before EBW. However, the hardness was decreased from 400 HV to 300 HV for ODS Eurofer BM, from 240 HV to 180 HV for Eurofer BM, due to grain coarsening after the PWHT with N&T. The grain size of HAZs, WM, and BM was increased after the PWHT with N&T. Especially that of Eurofer BM was increased significantly from 20 µm to 150µm. The microstructure of the materials in the present study showed more stable than ODS Eurofer and Eurofer. In addition, the present work showed the effect of two PWHT conditions on the microstructure of WM and HAZs. PWHT with N&T can eliminate the ferrite in the WM, and keep smaller carbides in the whole joint including HAZs, WM, and BMs. No significant grain coarsening was found in this work.

More mechanical property tests were conducted in L. Commin et al.'s work, such as Charpy impact test, creep test, etc. The Charpy V-notch was located at the WM of the joint. The EBW dissimilar-metal joint between ODS Eurofer and Eurofer showed higher DBTT than Eurofer BM, ODS Eurofer BM, and EBW Eurofer, because of quenched

marteniste in the WM. However, the impact properties can be improved by the following PWHT due to the recovered tempered martensite in the WM. The dissimilar-metal joint showed higher Laser-Miller parameter than EBW Eurofer, comparable to Eurofer BM. However, their work has not evaluated the bonding strength of the dissimilar-metal joint yet. In this work, more evaluation on mechanical properties for the EBW dissimilar-metal joint between 9Cr-ODS and JLF-1 should be done in the future. However, bonding strength of the joint was evaluated successfully by four-point bend tests and FEM simulation, as depicted in Chapter 4.

EBW is a proper technique to bond 9Cr-ODS and JLF-1 in the present study. Generally, fusion welding is not suitable for the single-metal bonding for ODS-RAFM steels, since the strengthening agent for ODS steels, nano-scale oxide particles, are decomposed in the WM due to the melting. Their joint is usually fabricated with non-melting process, such as HIP, PRW, FSW, etc. However, the nano-scale oxide particles are not necessarily required for the WM of the present dissimilar-metal joint between 9Cr-ODS and JLF-1, because the conventional RAFM steel does not contain nano-scale oxide particles and accepts no oxide-dispersion strengthening if the WM is not softer than the BM of the conventional RAFM steel. In the present study, the electron beam is located at the butting position of the 9Cr-ODS and JLF-1 blocks. After the EBW, the microstructure of the WM in the dissimilar-metal joint is mainly quenched martensite with 9% Cr. This quenched martensitic structure would never cause softening of the WM. Instead, hardening was induced. After PWHT with T or N&T, the microstructure is recovered to the same as that of the JLF-1 BM with tempered martensite. Actually, during the EBW process, the electron beam located at any position is expected appropriate for the dissimilar-metal bonding between 9Cr-ODS and JLF-1, such as at the butting position, or towards 9Cr-ODS side, or towards JLF-1 side. Since 9Cr-ODS and JLF-1 steels are both martensitic steels, after EBW, even if the nano-scale oxide particles in 9Cr-ODS are decomposed by the welding, however, because of the specific chemical composition with 9% Cr, the WM is always martensitic structure. This would never make the loss of the strength in the WM of the joint.

However, if the dissimilar-metal bonding is between ODS ferritic steel, such as 12Cr-ODS or 15Cr-ODS, and conventional RAFM steel, it should be noted that, the electron

beam should not be at the butting position or shifted towards ODS steel side to form ferritic structure without nano-particle dispersions. This would induce the loss of strength in the WM. Instead, the electron beam should be shifted towards the conventional RAFM steel side to make the whole WM form quenched martensitic structure. Thus, the softening of WM can be avoided. After the following PWHT, the microstructure of the WM can be recovered same as that of the BM of conventional RAFM steel with tempered martensitic structure.

3.3 The EBW joint of F82H steel—316L steel

3.3.1 Characterization of weld metal and heat-affected zones

Figure 3-23 shows the macroscopic image of the as-welded joint between F82H and 316L. The WM is dendritic structure with about 0.76 mm in width. The width of HAZ of F82H is about 0.37 mm. Because 316L has austenite structure, it has no microstructural evolution during the EBW. Therefore, the boundary of the HAZ of 316L cannot be distingushied.
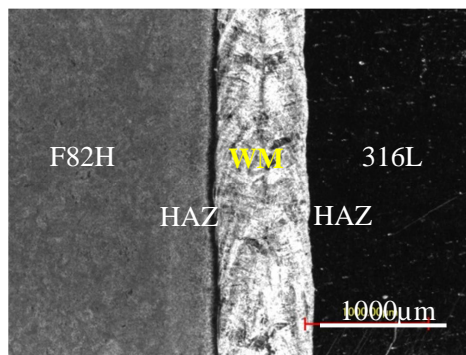
Figure 3-23 Macroscopic image of the EBW joint between F82H and 316L.

The HAZ of F82H can be classified into 3 regions: interlayer (IL), fine-grain HAZ, and coarse-carbide HAZ according to the distance from the fusion boundary, as shown in Figure 3-24. The IL is located between F82H and the WM with about 10µm in width. Its structure may be δ-ferrite according to S. Nogami's investigation[95]. The fine-grain HAZ with about 90 µm in width, is quenched martensitic structure with grain size of 9µm. The width of the coarse-carbide HAZ is about 270 µm. The grain size in corase-carbide HAZ is 57 µm, same as that in the BM of F82H. The coarse-carbide HAZ formed due to

the temperature there during welding was above the decomposition temperature of $M_{23}C_6$ carbides in F82H. Incomplete decompostion of carbides occurred there. The WM is austenite phase, same as that in the BM of 316L. It is dendritic structure with grain size of 8 µm, much smaller than that in the BM of 316L being 35 µm in size. There is no microstructure change for the HAZ of 316L, because there is no phase transformation during the EBW process, as illustrated the phase diagram and thermal cycle during the welding in Figure 3-25.
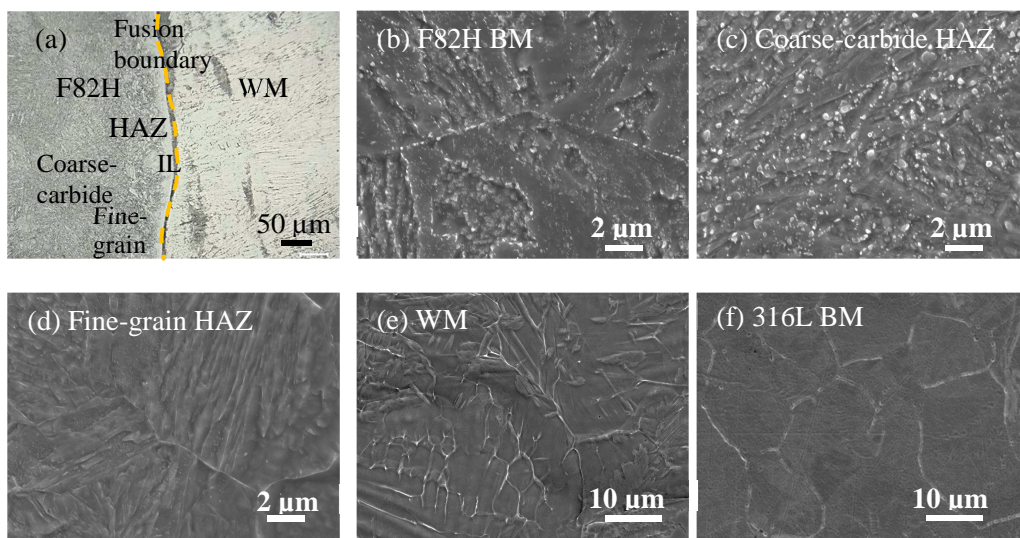
Figure 3-24 Microstructure of the as-welded joint between F82H and 316L.
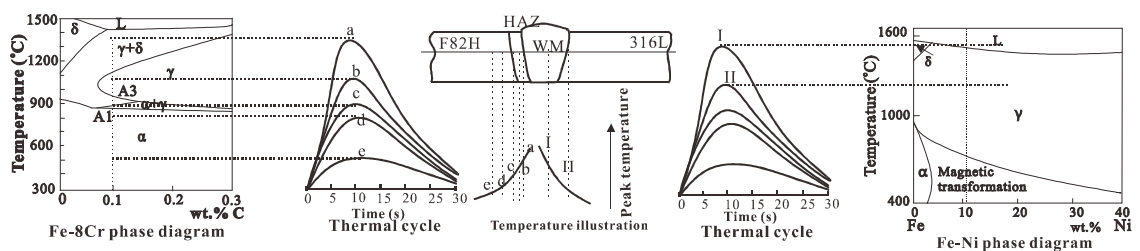
Figure 3-25 Phase diagram and thermal cycle of the joint between F82H and 316L during the EBW process.

3.3.2 Effect of PWHT

Figure 3-26 shows the hardness of the EBW joint between F82H and 316L. The microstructure of both the WM and HAZ of 316L was always austenitic structure because

no phase transformation happened during the EBW process, thus there was no hardening for the WM and HAZ of 316L. However, hardening was induced for the HAZ of F82H. The hardness was up to 400 HV. After PWHT with tempering, as the tempering temperature increased, hardness of the HAZ of F82H decreased. After PWHT with tempering at 750°C, hardening in HAZ of F82H was almost relieved, except the IL which kept the hardness of 245 HV after the PWHT.
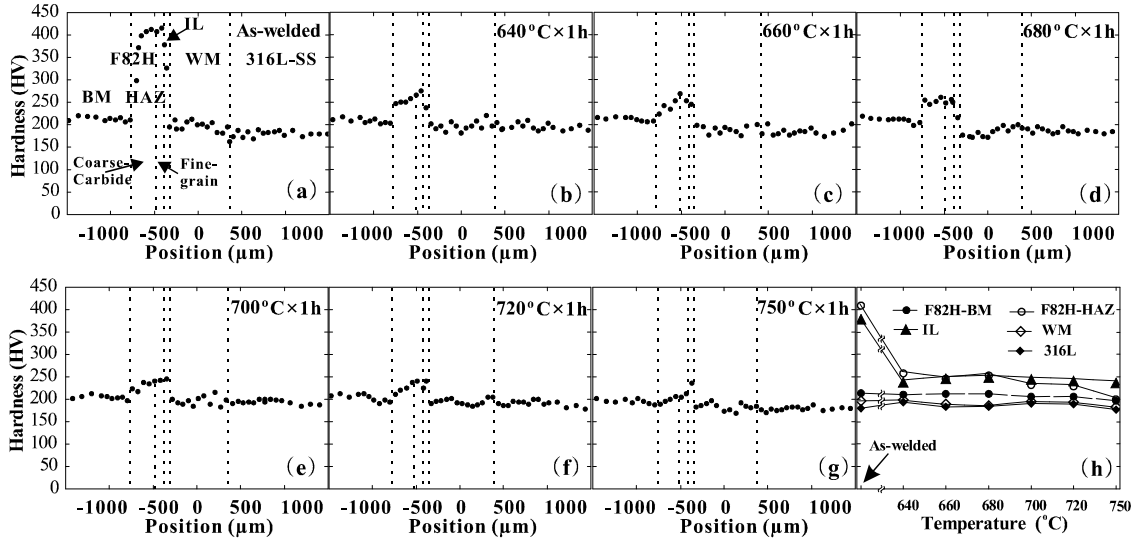
Figure 3-26 Hardness evolution of the joint between F82H and 316L.

The microstructure of the fine-grain HAZ of F82H is shown in Figure 3-27. In the as-welded condition, the microstructure was of quenched martensitic phase with high-density dislocations and laths (Figure 3-27 (a) and (c)). After PWHT at 680°C, the microstructure was tempered martensitic phase with $M_{23}C_6$ carbides on lath and grain boundaries (Figure 3-27 (b) and (d)).

Table 3-9 summarized size and density of carbides in the fine-grain HAZ, the coarse-carbide HAZ, and the BM of F82H under different conditions from SEM images. In the as-welded condition, there are no $M_{23}C_6$ carbides in the fine-grain HAZ because its structure is quenched martensite. In the coarse-carbide HAZ, the carbides density is smaller but carbide size is larger than those in the BM of F82H. This is because the carbides in the coarse-carbide HAZ were partly decomposed at the temperature during the welding. After PWHT at 680°C, the size and density of carbides in the fine-grain HAZ are smaller than those in the BM and in the coarse-carbide HAZ. This means that

more elements were kept in the matrix, not completely precipitated out in the fine-grain HAZ. After PWHT at 750°C, the carbide size and density in the fine-grain HAZ were increased to close to those in the BM of F82H. PWHT at higher temperature of 750°C made carbides completely precipitate out in the fine-grain HAZ. Thus the hardening in the HAZ can be completely eliminated. However, over-tempering was induced for BM of F82H when PWHT at 750°C. The carbide size increased compared to that in the as-welded condition and PWHT at lower temperature of 680°C. The over-tempering made softening of the BM of F82H.
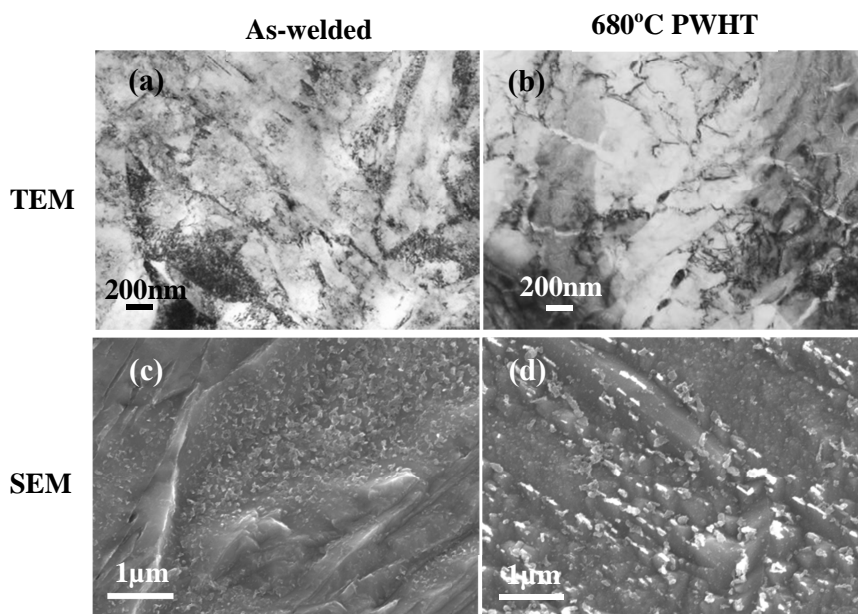
Figure 3-27 Microstructure of the fine-grain HAZ of F82H.

Table 3-9 Size and density of carbides in the BM, the coarse-carbide HAZ, and the fine-grain HAZ of H82H at the conditions of as-welded and after PWHT at 680°C and 750°C.

Position	Carbide conditions	As-welded	680°C PWHT	750°C PWHT
BM	Mean size (W×L, nm×nm)	55×100	55×100	60×100
	Number density (N/m^2)	$3.58×10^{13}$	$3.20×10^{13}$	$2.42×10^{13}$
Fine-grain	Mean size (W×L, nm×nm)	—	40×90	85×138
HAZ	Number density (N/m^2)	—	$1.86×10^{13}$	$1.74×10^{13}$
Coarse-carbide	Mean size (W×L, nm×nm)	84×170	60×100	90×120
HAZ	Number density (N/m^2)	$0.94×10^{13}$	$1.93×10^{13}$	$2.12×10^{13}$

Tensile tests were carried out at RT and 300°C for the joint at different conditions. The strain-stress curves are shown in Figure 3-28, and the tensile properties are summarized in Table 3-10. According to the distribution of element Cr and Ni in the joint, line scanning of the specimens after tensile tests can reveal the fracture site as shown in Figure 3-29. The specimens fractured at the soft site during tensile tests. For the conditions in as-welded and PWHT at 680°C, the tensile specimens fractured at the WM or 316L BM. The WM and 316L BM are both austenite structure. In the conditions of as-welded and 680°C PWHT, the BM of F82H still kept the strength higher than the WM and 316L BM, thus the specimens fractured at the softer WM or 316L (austenite structure). However, after PWHT at higher temperature of 750°C, the specimen fractured at F82H BM, i.e. fractured at tempered martensite, not at the austenite structure any more. As mentioned above, 750°C made over-tempering for the BM of F82H. The specimen fractured at F82H BM because of the softening induced by the over-tempering.
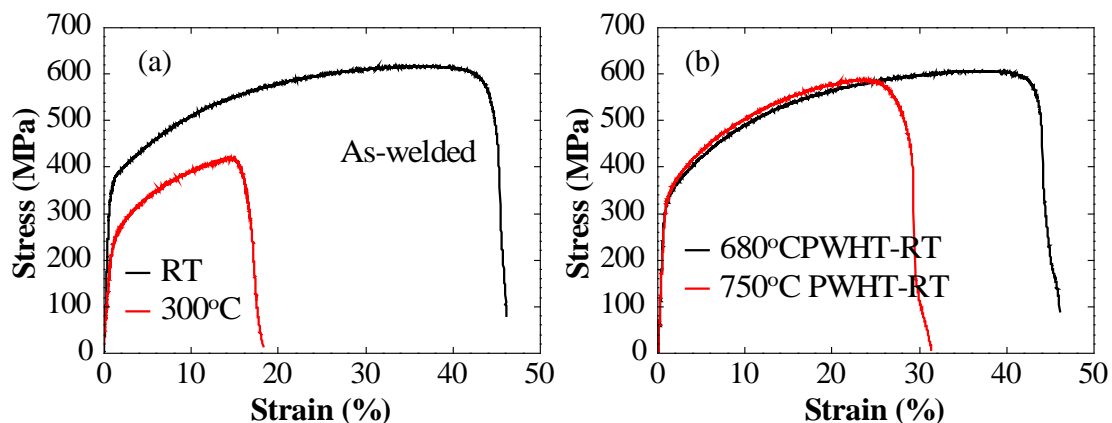
Figure 3-28 Strain-stress curves of the EBW joint between F82H and 316L (a) in as-welded condition and (b) after PWHT.

Table 3-10 Tensile properties of the EBW joint between F82H and 316L.

Condition	Test temperature	Total elongation (%)	Reduction of area (%)	Fracture site	Yield strength (MPa)	Ultimate tensile strength (MPa)
As-welded	RT	45	88	316L	360	610
As-welded	300°C	15	92	WM	250	420
680°C×1h PWHT	RT	46	82	316L	340	610

| 750°C×1h PWHT | RT | 24 | 81 | F82H | 350 | 590 |
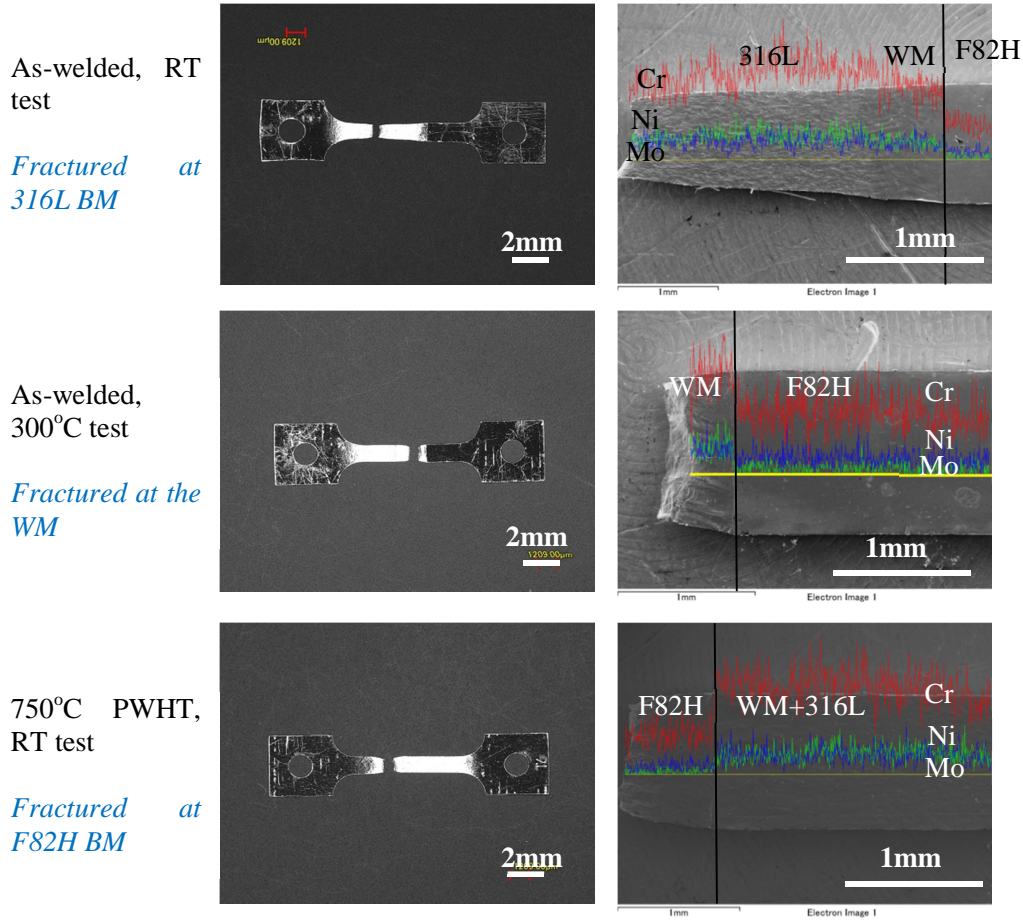
Figure 3-29 Line scanning of the specimens to indicate the fracture sites during tensile tests.

3.3.3 Effect of neutron irradiation

After PWHT at 680°C, the joint between F82H and 316L was neutron irradiated at 300°C for a dose of 0.1 dpa. Because of the limited volume during neutron irradiation, the joint was chosen at the condition of PWHT at 680°C from the viewpoint of avoiding softening of BM of F82H. However, other PWHT conditions are still remaining to be investigated in the future if possible.

Figure 3-30 depicts the hardness evolution after the neutron irradiation. Neutron irradiation induced hardening for the whole joint, such as BMs, WM, and HAZs. As-shown in Table 3-11, hardness of F82H BM after irradiation increased by 20 HV, while

that of the WM and 316L increased by 50-60 HV. According to S. Nogami et al.'s investigation of proton irradiation experiment on the joint, the number density and size of dislocation loops in austenitic structure of the WM and 316L BM can reach saturation earlier than that in the F82H[95]. One possible explanation is that, the original high density dislocations and lath boundaries in the F82H retarded the dislocation loop evolution during irradiation compared with the austenite structure in the WM and 316L BM. Thus the irradiation hardening in the WM and 316L BM was larger than that in the BM of F82H.

Interestingly, for the HAZ of F82H, the neutron irradiation hardening there is almost comparable to that in the as-welded condition. The hardness was increased by 100 HV after the irradiation for the IL and coarse-carbide HAZ. Especially, significant hardening happened in the fine-grain HAZ. The hardness was increased by 200 HV in the limited region of the fine-grain HAZ with about 50 µm in width.

One of possible mechanisms for the significant hardening in the fine-grain HAZ of F82H is irradiation induced precipitations from the carbon generated by the dissolution of prior carbides during the welding, as illustrated in Figure 3-31. The PWHT condition with 680°C was determined mainly from the viewpoint to avoid softening of F82H BM by over-tempering. However, the temperature was not enough to complete the recovery of the hardness in the fine-grain HAZ. The incomplete hardness recovery during PWHT at 680°C indicates the presence of residual carbon atoms to be precipitated out during the neutron irradiation.   For ferritic/martensitic steels, the irradiation induced precipitates can be fine M_6C (η) (diamond-cubic (E9$_3$, Fd3m) structure), α'(Cr-rich bcc ferritic phase), χ phases (Fe-Cr intermetallic), M_2X (hexagonal (L'3, P6/mmm) structure, needle shape), σ phase[113].   These fine precipitates retarded the motion of dislocations. Thus the hardening is significant at the fine-grain HAZ of F82H. In such a mechanism, the significant hardening would be reduced by higher temperature PWHT, such as 750°C. According to S. Nogami et al.'s[95] results of proton irradiation experiment on the joint, as depicted in Figure 1-15, after PWHT at 720°C for nearly complete relief of hardening induced by EBW (Figure 1-14), only irradiation hardening on the WM and 316L was found obviously. There was no significant hardening was observed for the HAZ of F82H.

Therefore, in this study, PWHT at 750°C for 1h is supposed to suppress the significant irradiation hardening from the viewpoint of precipitation control. If possible, this would be examined under neutron irradiation in future.
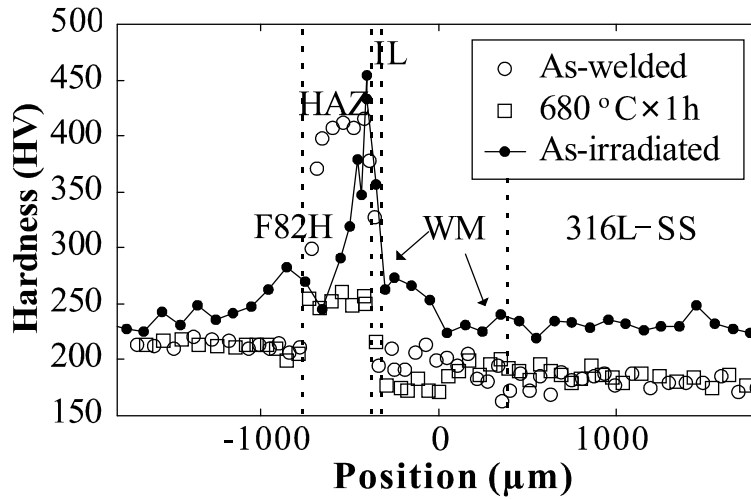
Figure 3-30 Hardness of the dissimilar-metal joint between F82H and 316L after neutron irradiation.

Table 3-11 Hardness at different positions before and after neutron irradiation (HV).

Condition	F82H BM	HAZ of F82H			WM	316L BM
		Coarse-carbide	Fine-grain	IL		
As-welded	220	406	415	327	197	179
PWHT: 680°C	214	253	254	249	184	183
As-irradiated	236	364	444	356	246	232
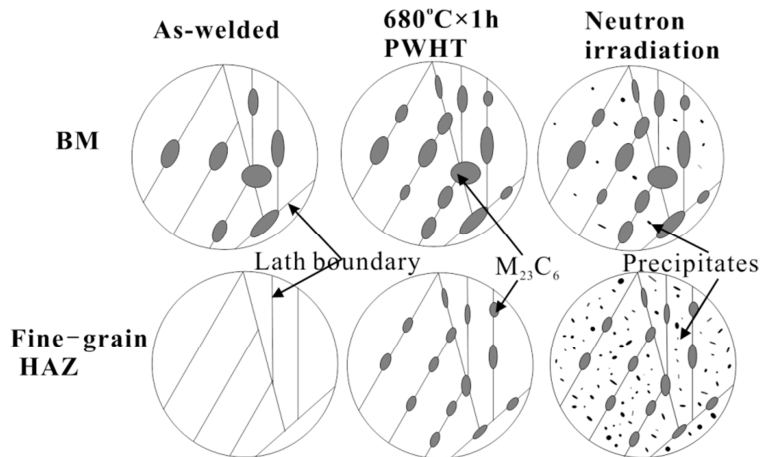
Figure 3-31 Schematic of the neutron irradiation induced precipitates in the fine-grain HAZ of F82H.

Charpy impact property of the joint before and after neutron irradiation is shown in Figure 3-32. The upper-shelf energy decreased after irradiation for all the CVN

78

specimens of BMs, WM, and F82H-HAZ. Both the WM and BM of 316L are of austenitic phase with excellent ductility. The impact properties did not change significantly by the irradiation. In these cases, the DBTT was estimated as less than -196°C. However, DBTT of F82H-BM and F82H-HAZ increased from -103°C to -20°C and from -143°C to -110°C, respectively, after irradiation. The impact property of the 1.5CVN specimen of F82H-HAZ degraded due to the irradiation hardening in the HAZ of F82H, but is still better than that of F82H-BM. Generally, hardening leads to degradation of impact properties. However, the significant irradiation hardening observed in the fine-grain HAZ of F82H did not degrade the impact property significantly. This is probably because the hardening area was very limited as several tens micron in size. In addition, 316L BM part of the specimens maintained much ductility and assisted the deformation of the joint during the impact test.
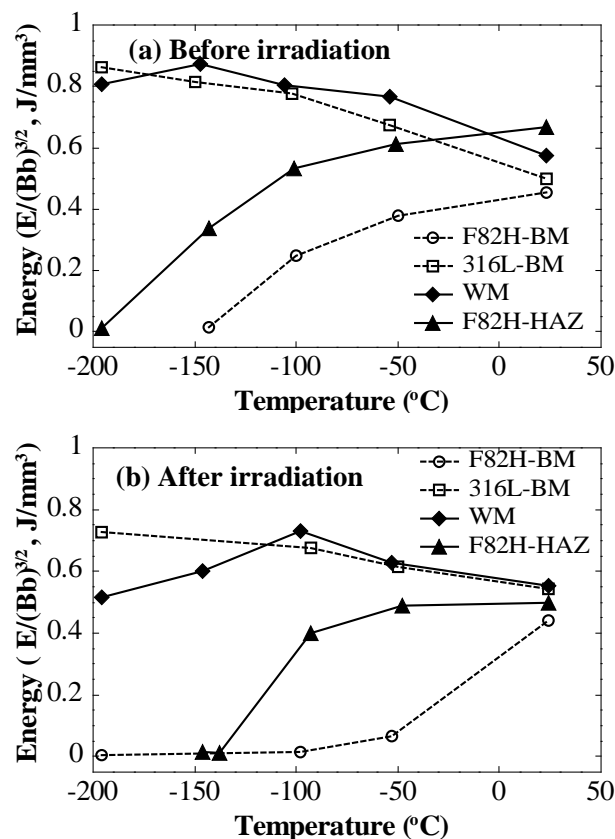
Figure 3-32 Charpy impact property of the joint (a) before and (b) after neutron irradiation.

Figure 3-33 shows the fracture morphology of the irradiated specimens after impact tests at -100°C. When the notch was located at the BM of 316L and the WM, the

specimens showed plastic deformation with good ductility after impact tests. When the notch was located at the BM of F82H, the fracture showed more brittle than that when the notch was at the HAZ of F82H. As explained above, the 316L part assisted the deformation of F82H-HAZ specimen during the impact tests. Thus the F82H-HAZ specimens showed better impact properties than the F82H-BM specimens.
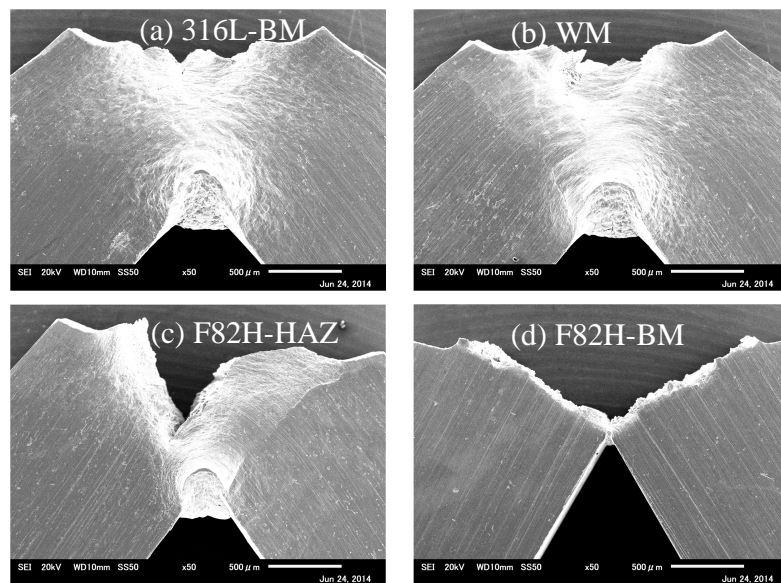
Figure 3-33 Fracture morphology of the irradiated V-notch specimens after Charpy impact tests at -100°C. The V-notch was located at (a) the BM of 316L, (b) the WM, (c) the HAZ of F82H, and (d) the BM of F82H, respectively.

The present work has investigated the effect of PWHT with tempering on the hardness recovery of the HAZ of F82H, as depicted in Figure 3-26. The complete hardness recovery needs higher temperature of 750°C. However, the neutron irradiation experiment was carried out with the PWHT at lower temperature of 680°C, from the view point of keep strength of the BM of F82H. The difference between the two PWHT conditions is shown in Table 3-12. PWHT at 750°C induced over-tempering of F82H BM. However, it was supposed no significant hardening in the HAZ of F82H after neutron irradiation experiment, because at this condition, hardening there was almost completely eliminated. There is no residual carbon to be precipitated out during irradiation. Trade-off

between "the significant hardening in the fine-grain HAZ" and "over-tempering of F82H BM" should be evaluated by more investigation in the future work.

Table 3-12 Comparison between PWHT at 680°C and 750°C.

Item	680°C PWHT	750°C PWHT
1	Keep the strength of BM of F82H	Over-tempering of BM of F82H
2	Still remain hardening in the HAZ of F82H	Almost completely relief the hardening of F82H
3	After neutron irradiation, significant hardening occurred in the fine-grain HAZ of F82H	It was supposed no significant hardening after neutron irradiation. This needs further investigation.
4	The significant neutron hardening did not deteriorate the impact property of the joint.	Needs further investigation for impact property after neutron irradiation.

One difference of this work from S. Nogami et al.'s[95] work is that, the microstructure of the HAZ of F82H was classified more in detail to IL, fine-grain HAZ, and coarse-carbide HAZ to investigate the mechanism of neutron irradiation induced significant hardening. The IL is δ ferrite. In their work, as the temperature in PWHT with tempering increased, the hardness of IL was decreased from 370 HV to 200 HV, similar level as that in BM. However, in this work, the hardness of IL kept stable as 250 HV after tempering from 640 to 750°C. There was still hardening in the IL. After the following neutron irradiation, the IL also showed significant hardening as hardness of 350 HV. However, in S. Nogami et al.'s work, no hardening was observed in the IL. This is may be caused by the effect of indentation size and its interval in hardness test. The interval for the indentation in hardness test by S. Nogami et al. was 100 μm, which is larger than the typical size of the hardening area, 50 μm, while the interval was comparable to the size of the hardening area in our tests. In addition, indentation size in their test was 10 μm, which is smaller than 30 μm in our test. Higher resolution for the position by the smaller interval, and larger interaction volume with surrounding area due to the larger indentation size can result in the detection of the localized hardening in our test.

Another difference from S. Nogami et al.'s work is that, no hardening was observed after proton irradiation at 300°C for 0.1 dpa in their work, but significant hardening was

found in the present work after neutron irradiation with the same 300°C for 0.1 dpa. Neutron irradiation for the present joint was after PWHT at 680°C (lower than S. Nogami et al.'s 720°C), to avoid over-tempering of base metal of F82H. At this condition, the hardening at the fine-grain HAZ of F82H was not completely eliminated. Significant neutron irradiation hardening was found in this area. One of possible mechanisms for the significant hardening is irradiation induced precipitations from the carbon generated by the dissolution of prior carbides during the welding. The incomplete hardness recovery during PWHT at 680°C indicates the presence of residual carbon atoms to be precipitated out during irradiation. However, S. Nogami et al.'s PWHT before proton irradiation was selected at 720°C. At this condition the hardening in the HAZ of F82H was almost eliminated, and hardness recovery was almost completed. No residual carbon atoms to be precipitated out during the following proton irradiation.

S. Nogami et al.'s proton irradiation experiments on the dissimilar-metal joint can only make the irradiation damage range from the surface of the specimens to 4 µm below the surface. Thus only microstructural analysis and hardness tests can be applied for the joints. Other mechanical property tests cannot be executed. In addition, to date, there is no work about neutron irradiation experiments on the dissimilar-metal joint between F82H and 316L was found. The present work demonstrated excellent neutron resistance of the joint by Charpy impact tests. The dissimilar-metal joint between F82H and 316L in the present study is expected to be located behind fusion blanket; therefore neutron irradiation condition should be similar to the vacuum vessel and magnets. The maximum dose for the vacuum vessel in ITER has been estimated as 0.027 dpa[114]. The neutron flux at the magnets in DEMO-grade reactor design has been obtained as, for example, 6×10^{22} n/m^2[115] and 1×10^{23} n/m^2[116]. Since the present irradiation dose was more than these conditions, the resistance of the dissimilar-metal joint to neutron irradiation has been demonstrated from the practical view point. However, the growth of the severe hardening region in the fine-grain HAZ has to be investigated if the joint is located at high dose position or other temperature area than the present irradiation temperature.

The behavior of the EBW dissimilar-metal joint between F82H and 316L (F82H—316L) in this work is different from that of the single-metal joint of F82H (F82H—F82H), as summarized in Table 3-13. For the joint of F82H—F82H after EBW,

the WM and two HAZs of F82H showed hardening[117] because of quenched martensitic structure. PWHT with tempering can eliminate the hardening in both the WM and HAZs. However, for the joint F82H—316L in the present work, the WM is austenite without hardening. Only the HAZ of F82H showed hardening. The data on impact property of F82H—F82H under similar neutron irradiation conditions in this work is not found. For the EBW joint of F82H—F82H with PWHT of tempering, after neutron irradiation at 300°C for 2.5 dpa, the DBTT is -15°C[118] at the WM (notch was located at WM), comparable to the DBTT in the BM of F82H in this study, -20°C. For the EBW joint of F82H—316L in this work, after neutron irradiation at 300°C for 0.1 dpa, because of austenite structure in the WM, the DBTT at the WM is <-196°C.

Table 3-13 Difference between the joint of F82H—316L and F82H—F82H.

	F82H—F82H	F82H—316L
WM	Martensite, hardening	Austenite, no hardening
HAZ	Two HAZs for F82H, martensite with carbide decomposition, hardening	HAZ for F82H, hardening. No evolution in HAZ of 316L, same with 316 BM
PWHT	Eliminate hardening in WM and HAZs	Eliminate hardening in HAZ of F82H
Impact properties	Notch in WM and HAZs: lower absorbed energy because of tempered martensitic structure	Notch in WM, high absorbed energy because of austenite structure Notch in HAZ of F82H, higher absorbed energy because of the support of the 316L side with large deformation
Neutron irradiation	Significant hardening in both HAZs if the PWHT is not sufficient	Significant hardening in HAZ of F82H if the PWHT is not sufficient

3.4 Optimum welding condition for the dissimilar-metal joints

1. The HIP joints between 9Cr-ODS and JLF-1

Dissimilar-metal joints between 9Cr-ODS and JLF-1 were fabricated by HIP at 1000°C, 1050°C, and 1100°C, under a pressure of 191 MPa for 3h with a cooling rate of 5°C per minute after the heating. The HIP process induced undesirable hardening in the BM of JLF-1, and also undesirable softening at the bonding interface, irrespective of the HIP temperatures.

The hardening is due to the formation of quenched martensite, which is an iron metal phase with super-saturated carbon in solid solution, because the cooling rate after the HIP was enough for quenching before carbon diffusion in the BM of JLF-1. While, it was too slow for 9Cr-ODS when HIP at 1000°C, where coarse carbides observed on the grain boundaries evidently indicated much diffusion of the carbon before quenching. In the 1000°C-HIP condition, no quenching and the carbide coarsening resulted in the softening of the BM of 9Cr-ODS. PWHT with a rapid cooling at 36°C per minute was effective to recover both the hardening and softening in the BMs. It is revealed that full recovery required the PWHT at 1050°C for 1h for normalization followed by 780°C for 1h for tempering.

On the other hand, the softening at the interface was attributed to decarburization of the specimen surface during the HIP process and less decomposition of carbides on the 9Cr-ODS side, which produced soft layer there. The decarburization layer with few particles was clearly observed in the 1000°C-HIP specimen. Furthermore, 1000°C-HIP also induced un-bonded areas at the interface. Both the soft layer and the un-bonded areas can lead to very local deformation and almost no elongation of the joint in tensile tests. Even PWHT cannot eliminate the un-bonded areas. However, the elongation was improved very much at higher HIP temperatures, such as 1050°C and 1100°C. The interface was completely bonded. Disappearance of the few-particle layer was also observed at the temperatures. It is probably promoted by the decomposition of the $M_{23}C_6$ carbides at the high temperatures and the following diffusion of carbon into the few-particle layer. Actually, the 1100°C-HIP resulted in slight lower strength of the joint than the 1050°C HIP. This is likely because of coarsening of grain structures. Therefore, 1050°C is the optimum HIP temperature for the present dissimilar-metal bonding.

In conclusion, PWHT after the HIP can control the recovery of the BMs of the joint. However, the improvement of joint interface requires higher HIP temperature to

eliminate the few-particle layer and unbounded areas at the interface. The optimum condition is, HIP at 1050°C followed by normalization at 1050°C and tempering at 780°C.

2 The EBW joint between 9Cr-ODS and JLF-1

The hardness of the WM and both the HAZs in 9Cr-ODS and JLF-1 was much higher than the BMs. The WM is quenched martensitic phase with occasionally some ferritic phase (iron metal phase with thermal equilibrium carbon in solid solution). The HAZs are also quenched martensitic phase with carbides decomposition. The quenched martensite in the WM and HAZs contributes the hardening and can induce embrittlement for the joint. Ferritic phase is soft and does not induce embrittlement by the formation itself. However, it is known that ferritic phase induces more irradiation hardening and embrittlement under neutron irradiation condition, compared with martensite. Therefore, both the quenched martensitic phase and the ferritic phase should be eliminated. Two conditions of PWHT were carried out for the joints to recover the hardening and the microstructure of WM and HAZs to the levels close to the BMs.

One was only tempering at 720-780°C for 1h. The tempering removed a part of carbon in solid-solution and hardening by it, and changed the quenched martensite into tempered martensite. As the tempering temperature increased, the hardening of the WM and HAZs was relieved. The PWHT necessary for the complete recovery of the hardening was obtained as 780°C for 1h. However, the ferritic phase remained after the PWHT. Therefore, the other condition based on the 780°C PWHT was examined.

The other condition of PWHT was a combination of normalization at 1050°C for 1h and then tempering at 780°C for 1h. Because of the normalization, residual ferrite disappeared. The whole microstructure including the WM, the HAZs, and the BMs was quenched martensite just after the normalization. After the following tempering, the whole microstructure was tempered martensite. No residual ferrite existed anymore. The PWHT with combination of normalization and tempering is the optimum to relief the hardening of WM and HAZs, and eliminate the residual ferrite at the same time.

3. The EBW joint between F82H and 316L

PWHT with tempering was carried out at 640-750°C for the dissimilar-metal joint between F82H and 316L made by EBW. PWHT at 680°C can suppress softening and keep the strength of F82H BM. However, the hardening in the fine-grain HAZ cannot be

completely eliminated. This resulted in the significant neutron induced hardening in this area. The significant neutron hardening did not deteriorate the impact property of the joint in the present irradiation condition at 300°C for 0.1dpa, though it should be seriously evaluated if the joint is used in other severe conditions such as at higher temperatures or higher irradiation doses.

PWHT at 750°C made a little softening of F82H BM. But the hardening induced by EBW in the HAZ of F82H was almost completely eliminated. It is supposed that, after neutron irradiation, there is no significant irradiation hardening existed in the fine-grain HAZ of F82H anymore. However, this should be evaluated by neutron irradiation experiments in the future.

In conclusion, from the viewpoint of avoiding significant neutron induced hardening in the HAZ of F82H, 750°C is a better choice for the PWHT condition of the dissimilar-metal joint between F82H and 316L.

3.5 Schaeffler diagram and carbon behavior of the joints

Schaeffler diagram[119] as shown in Figure 3-34, plots the compositional limits at RT of austenite (A), ferrite (F), and martensite (M) according to nickel and chromium equivalents. It is often used to predict phase composition during fusion welding. In the Schaeffler diagram, Cr and Ni equivalent is calculated as follows,

Cr equivalent= (Cr) +2(Si) + 1.5(Mo) + 5(V) + 5.5(Al) + 1.75(Nb) + 1.5(Ti) + 0.75(W)

Ni equivalent= (Ni) + (Co) + 0.5(Mn) +0.3(Cu) + 25(N) + 30(C)

All element concentrations are expressed in weight percentages.

EDS in SEM can roughly estimate the chemical composition at different positions in the dissimilar-metal joints made by EBW in the present study. Table 3-14 shows the chemical compositions and the corresponding Cr and Ni equivalent in the WM and HAZs of the joints developed in the present work. According to the Cr and Ni equivalent, the WM of the dissimilar-metal joint between F82H and 316L is austenite structure, the WM of the joint between 9Cr-ODS and JLF-1 is martensite with ferritic structure. The HAZs of F82H, 9Cr-ODS, and JLF-1 also shows martensite with ferritic structure. This is

agreed with the microstructure observation by SEM, which is mentioned in Section 3.2.1 and 3.3.1.

WM of F82H—316L

A

A+M

A+F

M

HAZ of F82H
WM of 9CrODS—JLF-1

F+M

M+F

A+M+F

F

HAZ of 9CrODS, JLF-1

Ni equivalent

20

10

0

0   10   20   30
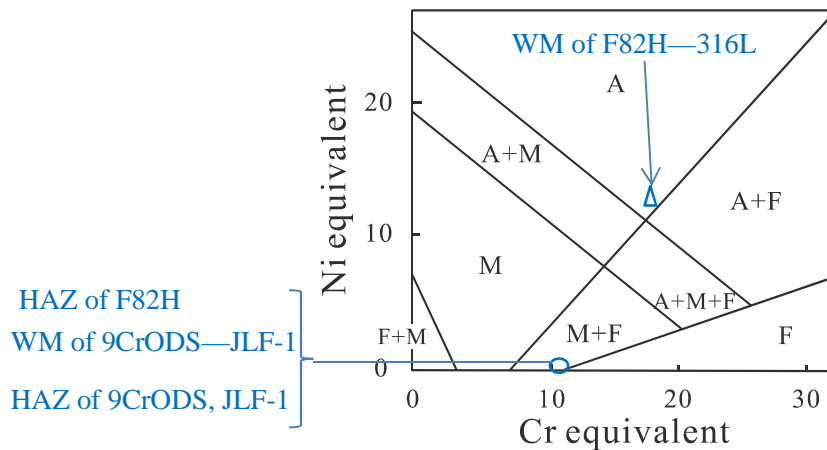
Cr equivalent

Figure 3-34 Schaeffler diagram recomposed from[119].

Table 3-14 Chemical compositions at different positions in EBW joints detected by EDS (wt.%).

	Cr	Ti	W	Ni	Mn	Si	Cr equivalent	Ni equivalent	Phase
WM of 9Cr-ODS—JLF-1	9.45	0.27	2.16				11.5		M+F
HAZ in 9Cr-ODS	9.06	0.23	1.85				10.8		M+F
HAZ in JLF-1	9.53		2.24		0.53		11.21		M+F
WM of F82H—316L	16.37			11.16	1.78	0.9	18	12.05	A
HAZ of F82H	9.09		3.18				11.5		M+F

The mechanical properties of the joints in this study were controlled by the carbon behavior, as summarized in Figure 3-35. If carbon was dissolved in the matrix to form quenched martensite, the joint would be hardened. If carbon was precipitated out in carbides (especially in coarse carbides) the joints would be softened. For instance, when HIP at low temperature of 1000°C, the incomplete decomposition of carbides (carbon was kept in coarse carbides, not in matrix) and ferritic structure induced softening of 9Cr-ODS BM; complete decomposition (carbon was kept in matrix) made hardening of JLF-1 BM after the HIP; and decarburization (escape of carbon in matrix) also induced softening at the interface after HIP. In addition, carbon dissolution (quenched martensite) made hardening of WM and HAZs of the EBW joints between 9Cr-ODS and JLF-1 and

between F82H and 316L. Proper PWHT can recover the mechanical properties of the above-mentioned joints from the undesirable hardening or softening.

Moreover, after neutron irradiation, more precipitates come out from the carbon generated by the dissolution of prior carbides during the welding at the fine-grain HAZ of F82H, and induced significant hardening at this area. The incomplete hardness recovery during PWHT at 680°C indicates the presence of residual carbon atoms to be precipitated out during neutron irradiation.
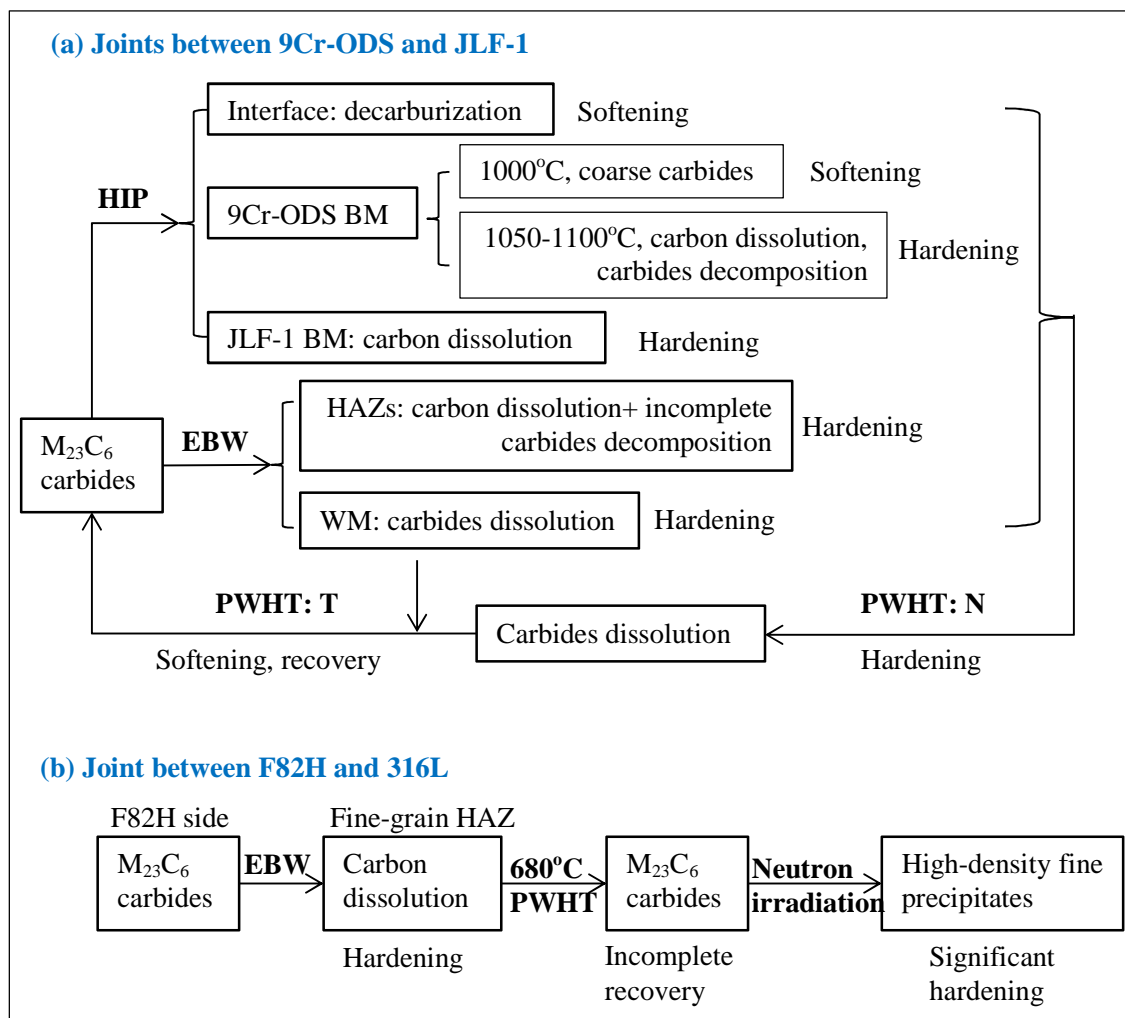
Figure 3-35 Carbon behavior in the dissimilar-metal joints at different conditions.

3.6 Scenario for the construction of blanket

In the present work, for the blanket fabrication with conventional design concept in Figure 1-8 (a), the scenarios are shown in Figure 3-36 (a). Conventional RAFM steels are fully selected as the blanket material in this concept. The blanket fabrication process can be as follows, (1) the whole blanket system with rectangular coolant tubes and the first wall panels which are made of RAFM steels, are capsuled and sealed into soft steel, and then HIP is carried out at such as the optimum condition of $1050^{o}C$ for 3h under 191 MPa with cooling rate of $5^{o}C$/min. And then, because the cooling rate is enough for conventional RAFM steels to form quenched martensite without any carbides, PWHT with only tempering ($780^{o}C$) is necessary to recover the mechanical properties of the blanket. Bending of the coolant tubes in the blanket structure can be applied before or after the HIP. If it is after the HIP, final heat treatment with N&T or only T is necessary to recover any possible material deterioration and residual stress caused by the bending process[120]. The last step for the blanket construction is the pipes connection between the blanket and the out vessel components which are made of stainless steel. Fusion welding such as EBW, LW, and TIGW can be utilized. TIGW is more suitable for the on-site welding for the blanket construction.

On the other hand, for the construction of the blanket structure with advanced ODS-RAFM steels partly used as the blanket surface, which is depicted in Figure 1-8 (b), the scenarios are also shown in Figure 3-36 (b). The difference of its construction from the blanket with above mentioned conventional concept is that, at first the rectangular coolant tubes of ODS-RAFM steels are joined with tubes of RAFM steels by fusion welding. PWHT is unnecessary after the fusion welding in this step, because the next HIP procedure at high temperature would change the microstructure of the materials, the PWHT after HIP can recover the joint by fusion welding at the same time. And then, the first wall plates with ODS-RAFM steels together with the above mentioned rectangular coolant tubes would be capsuled and sealed into soft steel for HIP. If the cooling rate after HIP is slow as the similar condition in the present work with $5^{o}C$/min, the PWHT after the HIP is different from the blanket with conventional concept. PWHT with normalization ($1050^{o}C$) is necessary to eliminate coarse carbides in ODS-RAFM steels.

However, if the HIP is carried out with a fast cooling rate such as $36^{o}C$/min in the present study to induce full martensite for ODS-RAFM steels, only PWHT with tempering is enough for recovery of microstructure and mechanical properties of the blanket with ODS-RAFM steels.

After HIP, the capsule can be not removed to avoid atmosphere contamination during the following PWHT. The PWHT after HIP can be carried out by seeking the collaboration with large corporations, such as corporations for steel production. Bogie Hearth Furnace can be used for the PWHT which can bear a load of up to 40 tons. In this case, if one blanket module weighs 2 tons, twenty blanket modules can be heat treated at a time. For example, the Japanese DEMO reactor concept, Slim CS, will require about 3500 tons[121] of RAFM steel such as F82H. About 90 batches PWHT for HIP are necessary for the blanket fabrication. The temperature of Bogie Hearth Furnace can be up to 1300°C, and can fulfill the PWHT requirement in the present study ($1050^{o}C$ for normalization, $780^{o}C$ for tempering). The large components are loaded outside the furnace. Afterwards, the hearth moves into the furnace housing. As soon as the furnace door is closed, the bottom side of the bogie hearth seals itself automatically against the bottom side of the furnace. After the heat treatment, the bogie hearth is moved through the open furnace door and out of the furnace to be unloaded.

After the fusion welding between blanket (RAFM) and out-vessel components (stainless steel) for coolant tubes connection, local circumferential PWHT can be used for the joints to eliminate hardening in the weld metal and heat affected zones. Low/high voltage electric resistance heaters (contact pads or radiation elements supported on a structure), high velocity gas combustion burners (high velocity gas, luminescent flame, and infrared burners), induction coils, and quartz lamps can be used to perform the local PWHT. Local heating is also useful during on-site fabrication and repair of components for the fusion blanket.

① HIP + PWHT → Bending

First wall plates + Rectangular tubes

RAFM steel

② Bending → HIP + PWHT

Fusion welding + PWHT

With Stainless steel

(b)For advanced design blanket

Rectangular tubes   **ODS steel + RAFM steel**

Fusion welding

ODS First wall plates + Rectangular tubes

① HIP + PWHT → Bending

② Bending → HIP + PWHT

Fusion welding + PWHT

With Stainless steel
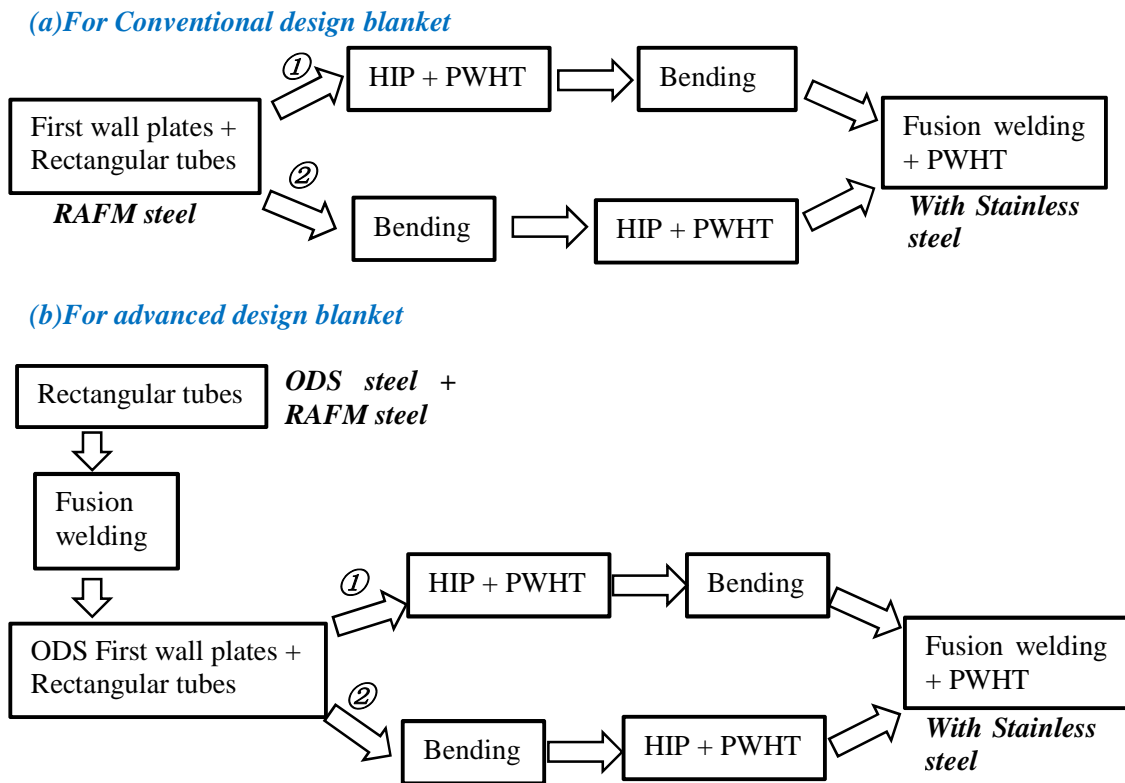
Figure 3-36 Scenarios for the blanket construction in the present study.

However, the breeding blanket systems containing tritium breeder and neutron multiplier have more complicated structure with a lot of joints than the present condition depicted in Figure 1-8. HIP is a matured technology, and can be utilized to fabricate full scale blanket systems with cooling channels. Fusion welding can be utilized for butt joint and corner joint in the blanket systems. For RAFM steels such as F82H, there is no big technical issue for fusion welding. Very low hot cracking sensitivity was found and the mechanical properties were not far different from that of BM after PWHT at 720°C for 1h[121]. H. Tanigawa et al.[122] have demonstrated the fabrication technologies for ITER WCSB TBM (water-cooled solid breeding test blanket module) by using F82H. Total net weight of the blanket module is about 2 tons. A variety of plates, pipes, and round and rectangular tubes are required for its fabrication. TIGW is used for sealing of headers of first wall, side wall, and back wall, because it has the largest gap allowance compared to other fusion welding methods. EBW can minimize the volume of weld bead and is preferable for thick-plate welds. LW was selected for fabrication of membrane panel which is required for the breeder and multiplier partition. A. von der Weth et

al.[123] have investigated the fabrication process of the first wall made from Eurofer steel with U-shape plate containing coolant channels. Manufacturing of it can start with flat symmetric half plates with half of the coolant channels milled in each plate. The surfaces are cleaned and degreased by plasma etching or dry ice cleaning. These plates are connected by diffusion bonding and are bent to U-shape. Diffusion bonding is carried out by an industrial scaled triple step process. The first step is homogenization of the plastic creep behavior of the structural material at $1050^{o}C$. The second step applies pressure of 30 MPa and lower temperature of $1010^{o}C$ for plastic deformation of the two half pieces to produce intimate contact. The third step (15 MPa and $1050^{o}C$) forces the diffusion bonding and improvement of the seam quality. PWHT is necessary for martensite transformation ($980^{o}C$, 30min) and then tempering ($760^{o}C$, 90min) for ductility recovery. The FW panel has to be bent twice for U-shape. A second PWHT should be conducted to remove the residual stresses and possible deterioration caused by the bending and to restore ductility. The blanket structure is very complicated. Therefore, in the future for the blanket construction of fusion reactors, the experiences from other scientists should be referred.

3.7 Corrosion problem for the dissimilar-metal joints

The dissimilar-metal joints developed in the present work would undergo corrosion attack in coolants such as water, Li, LiPb, He, or FLiBe, under non-isothermal conditions. Dissolution of material in one region would lead to mass transfer and deposition of solute in another part of the coolant system. Proper coating can be used to resist corrosion, such as coatings of Y_2O_3, Er_2O_3, or multi-layer coating alternated with vanadium and oxide. Nagasaka et al.[124] suggested combination of VPS W coating for simple and large area coating and chromizing for limited but complicated shape section. The coatings indicated suppression of fluoridation in corrosion tests compared to JLF-1 steel without coating.

For the HIPed joints used near the first wall surface and in the breeding blanket (plates with coolant channels) if the joints are fabricated according to the scenario as depicted in Figure 3-36, there is no corrosion problem for the joints because the interface would not contact the coolant. Only corrosion on RAFM structural materials themself

such as 9Cr-ODS and JLF-1 should be considered there. However, as suggested by A. von der Weth et al.[123], if the HIP process was conducted on flat symmetric half plates with half of the coolant channels milled in each plate, corrosion problem should also be considered because the interface would contact the coolant.

For the joints made by fusion welding (pipes connection), elements C and N in coolant would transfer into the joints. This may make coarsening of the carbides in HAZs, and make embrittlement there. Element O in joints would transfer to the coolant. If the WM has more oxygen content in the WM during welding induced by contamination (by TIGW), there may be more severe corrosion in the WM than in the BMs. This would induce softening there. Corrosion resistance of the dissimilar-metal joints should be verified in the future work.

Up to now, few corrosion experiments on dissimilar-joints for fusion blanket were conducted, especially for the joints between ODS-RAM steel and conventional RAFM steel. However, corrosion problem for material itself or similar-metal joints has been widely investigated by scientists. J. Konys et al.[125] have performed corrosion tests for RAFM steels of Eurofer and CLAM in flowing Pb-15.7Li at a flow velocity of about 0.10m/s in the PICOLO loop at Karlsruhe Institute of Technology (KIT). The corrosion attack rate is 220µm/yr. The dissolved amount of material (2 $kg/m^2 yr$) is significant and precipitates formed at cooler loop sections are a serious risk for plugging. A combination of corrosion barriers, which also act as tritium permeation barriers, would be necessary to control circulating precipitates. Y.F. Li et al.[126] have investigated 9Cr-ODS in static Li at 600^oC for 250h. 9Cr-ODS showed slight weight loss and decrease in hardness near surface. The corrosion attack also induced loss of ductility and decrease of creep lifetime. Microstructural analysis demonstrated a non-uniform corrosion behavior by preferential grain boundary attack and pronounced nodule-like morphology. Slight depletion of Cr was detected to about 15um in depth. The nano-scale oxide particles of TiO_2 in 9Cr-ODS are thermodynamically less stable, and can be decomposed to form Li_2O in Li environment. Y_2O_3 in 9Cr-ODS may be reacted with Li to form $YLiO_2$. The mechanism of corrosion was proposed as the dissolution of Cr and Fe in matrix into liquid Li, chemical interaction of nano-scale oxide particles with Li, preferential grain boundary attack and penetration of Li, and finally development of extreme nodule-like structure.

Austenitic stainless steels are easy to produce transformation to ferrite in surface layer when exposed to Li due to preferential dissolution of austenite stabilizing elements of Mn and Ni[127]. In Q. Xu et al.'s results[128], RAFM steel JLF-1 also showed phase transformation from tempered martensite to ferrite in the near surface at 600-700°C in Li because of decarburization. Selective depletion of Cr and W was also detected on the surface. The decarburization and element depletion induced softening on the surface. Their results also revealed corrosion rate in a thermal convection Li loop was significantly larger than that in the static Li. The flowing Li enhanced the weight loss, phase transformation, and hardness reduction due to mass transfer. T. Muroga et al.[129] reported that corrosion rate of JLF-1 steel was enhanced with the increase of the N content in Li. When exposed in liquid FLiBe, both fluoridation and oxidation were observed. In addition, the weight loss was much larger in a Ni crucible than in a RAFM crucible may be induced by electrochemical circuit effect. It was suggested that the corrosion rate of RAFM can be reduced by limiting the N impurity in Li and avoiding the use of dissimilar materials in FLiBe coolant systems.

X. Chen et al.[130] have studied an as-welded joint (without PWHT) for RAFM steel CLAM made by TIGW in flowing liquid Pb-17Li at 480°C. There is no penetration of LiPb for long exposure time. The main corrosion attack is caused by the dissolution of the passivated layer. However, the joint showed different behavior from the BM due to effect of welding thermal cycle. The weight loss test showed that corrosion resistance of CLAM steel joint is poor when exposed in up to 1000h dynamic conditions. The thicker martensitic lath in the WM led to higher corrosion amount. With the increasing exposure time, the corrosion rate decreased. The area short of Cr in the thick martensitic lath in the WM is easily corroded. Large residual stress after fusion welding would also lead to more severe corrosion attack in the WM. Thus PWHT after welding is necessary for stress relief to reduce corrosion in liquid coolant.

The corrosion behavior for a dissimilar-metal joint between SUS410 ferrite steel and SUS316 austenitic stainless steel made by TIGW in Li environment at 600°C for 250h was investigated by V. Tsisar et al.[131]. Marked depletion of Cr in ferritic structure and depletion of Ni in austenitic structure was found in near-surface layers. And low-angle sub boundaries transformed into large-angle due to grain boundary corrosion attack.

The WM in the dissimilar-metal joints developed in the present work are supposed to have better corrosion resistance than the BMs, since the microstructure in the WM of the EBW joint between 9Cr-ODS and JLF-1 has smaller grain size and lath width than the JLF-1 BM. The WM in the joint between F82H and 316L has austenitic structure with smaller grain size, different from the F82H BM. It is also believed to have better corrosion resistance than the F82H BM. However, corrosion reaction of these joints is complicated due to different materials and chemical compositions at different positions of WM, HAZs, and HAZs under different corrosion environment of liquid coolant with various temperatures, exposure time, flow speed, etc. For instance, the corrosion behavior of steels in LiPb and pure Li are different. The influence of impurities such as O, N, and C on the compatibility in LiPb is limited contrast to significant effects in Li. A layer of protective corrosion products can form on the surface of RAFM because of lower Li reactivity. The corrosion resistance of the joints developed in the present work should be evaluated in detail by various experiments in the future. More mechanical property tests should be conducted to evaluate degradation of the joints under corrosion environments of coolants such as FLiBe molten salt proposed in NIFS.

3.8 Summary

For the dissimilar-metal joints made by HIP, because of the slow cooling rate after HIP, the microstructure of 9Cr-ODS BM is ferrite with coarse carbides in the 1000°C-HIP condition, while quenched martensite with smaller coarse carbides in the 1050°C- and 1100°C-HIP conditions. However, the microstructure of JLF-1 BM is always quenched martensite in all the HIP conditions. The as-HIPed dissimilar-metal joints, fractured at 9Cr-ODS near the interface during tensile tests because of the local softening induced by less carbides decomposition and the decarburization layer at the interface there. Low temperature HIP at 1000°C also induced un-bonded areas at the interface which made crack initiation during tensile tests. HIP at higher temperatures of 1050°C and 1100°C is effective to heal the un-bonded areas. The optimum HIP temperature is 1050°C, at this condition, the joint showed the best bonding strength. After PWHT with normalization and tempering (1050°C×1h + 780°C×1h) with a fast cooling rate, the

bonding property was improved further, since the joints fractured at JLF-1 BM not at the interface anymore. At the same time the microstructure of both the 9Cr-ODS and JLF-1 BMs was recovered to that before HIP with tempered martensite.

Dissimilar-metal joints between 9Cr-ODS and JLF-1, and between F82H and 316L were fabricated by EBW. Bonding mechanism was realized by microstructural characterization. PWHT was carried out for recovery of microstructure and mechanical properties. Proper PWHT parameter was obtained for the joints. PWHT with normalization and tempering ($1050^{o}C\times1h$ + $780^{o}C\times1h$) for the dissimilar-metal joint between 9Cr-ODS and JLF-1 is good for avoiding softening of the BMs, relieving hardening in HAZs and WM, and eliminating the ferritic structure in the WM. For the dissimilar-metal joint between F82H and 316L, complete relief of hardening in the HAZ of F82H needs PWHT at $750^{o}C$. However, for avoiding softening of F82H BM, PWHT at lower temperature $680^{o}C$ is necessary.

Significant irradiation hardening occurred in the fine-grain HAZ of the joint between F82H and 316L due to irradiation induced precipitations. The joint has good neutron irradiation resistance despite the significant hardening. PWHT at higher temperature at $750^{o}C$ is supposed to avoid the significant irradiation hardening.

The dissimilar-metal joints developed in the present study should be evaluated for corrosion compatibility in coolant systems in the future work.

4. Finite element method (FEM) simulation for deformation behavior of the EBW joint 9Cr-ODS—JLF-1

Up to now, bend tests including three-point and four-point bend tests used to determine bonding strength of dissimilar-metal joints were not found in the field of fusion blanket structures. As summarized in Table 4-1, bend tests were carried out for pure materials (not joints) in the field of biological materials[132], ceramics[133][134], fiberglass[135], wood[136], viscoelastic materials[137], and so on. In their experiments the bending strength was expressed mostly with load "N", not given in the unit of "MPa". Ö.ÜNAL et al.[138] have applied asymmetric four-point bend tests to evaluate shear strength of the solder joints of Sn-Ag alloys. However, in the plastic phase, the shear strength was incorrectly estimated according to elastic theory. C.A Lewinsohn et al.[139] has applied both symmetric and asymmetric four-point bend experiments to evaluate bonding strength of the joints of SiC/SiC composites for fusion application. Because the deformation is still in elastic phase, of course the bonding strength can be calculated according to elastic theory. H. Serizawa et al.[140][141] have investigated the joints of SiC/SiC composites by the simulation of asymmetric four-point bending with finite element method (FEM). The shear stress distribution at the interface of the joint calculated by FEM was almost agreed with elastic analytical theory. However, because of limited plasticity of SiC/SiC composites, their FEM work was mainly focused on small deformation behavior of the joints. K. Ueda et al.[142] and J. Henry et al.[143] have applied bend tests with FEM simulation to evaluate neutron irradiation and He induced embrittlement of Mo, W, and T91 steel up to plastic deformation. As concluded in the table, bend experiments with FEM simulation is a potential technique to evaluate bonding strength of joints especially for dissimilar-metal joints with large deformation. This kind of work has not been found yet in the field of fusion blanket structure and needs to be developed. Thus the objective of the present work is to evaluate bonding strength for the EBW dissimilar-metal joint between 9Cr-ODS and JLF-1 by combination of symmetric

four-point bend experiments and FEM simulation. This work is also necessary for other fusion related dissimilar-metal joints in the future.

Table 4-1 Current status using bend tests to evaluate strength of materials or joints.

	Materials/joints	Status
Other non-fusion fields	Ceramic, wood, glass, epoxy, etc.	Bending with elastic theory or FEM analysis to evaluate strength (small elastic deformation)
	Solder joints	Bending with elastic theory analysis
Fusion field	SiC/SiC joints	Bending with elastic theory or FEM to evaluate bonding strength (small elastic deformation)
	Mo, W, T91 alloys	Bending with FEM (large plastic deformation)
Comments	Bend tests combined with FEM simulation are a potential technique to evaluate bonding strength of joints especially for dissimilar-metal joints with large plastic deformation for fusion application.	

4.1 Simulation model

In Section 3.2, the bonding strength of the EBW joint between 9Cr-ODS and JLF-1 cannot be gained by uniaxial tensile tests because the specimens always fractured at the JLF-1 BM, not at the WM. The bonding strength is only roughly estimated larger than the ultimate strength of JLF-1 BM. In this chapter, symmetric four-point bend tests were carried out to concentrate the stress inside the inner span including the WM, thus bonding strength of the joint can be obtained.

Figure 4-1 depicts the illustration of symmetric four-point bend test. During the bending process, there is no shear stress, only normal stress inside the inner span of the specimen. According to elastic theory, the maximum normal stress occurs at the top and bottom center of the bending specimen, and can be calculated according to the formula as follows[144],

$$\sigma_{max} = \pm \frac{3P(S-L)}{2HB^2} \quad\quad (4\text{-}1)$$

Where, H and B are the thickness and width of the bending specimen, P is the applied load on the upper jig which is contacting the specimen, and S and L are outer span and inner span during bend experiment.
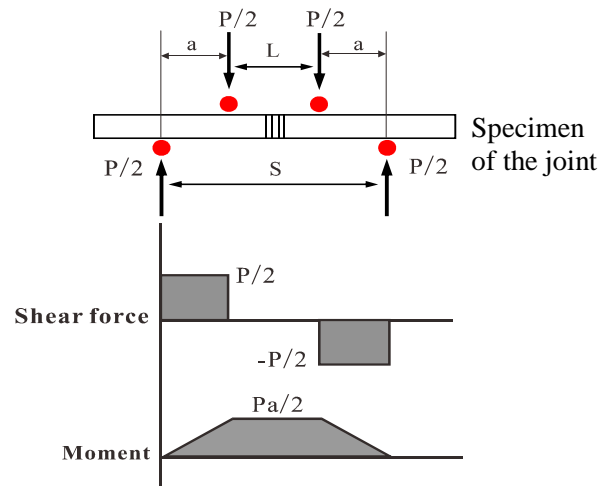
Figure 4-1 Illustration of shear force and bend moment in symmetric four-point bend test.

However, the formula from the elastic theory can only provide the stress condition of the present specimens up to about 0.25% in strain, though the experiments showed larger deformation with more than 10% in strain due to plastic deformation. Therefore, computer simulation with FEM was used to extend the analysis to larger deformation condition in the bend experiments.

The geometric modeling of the bending system including specimen and jigs was constructed in the unit of mm; accordingly, density and Young's modulus of the materials of jig and specimens, which will be mentioned thereafter, should be in the unit of ton/mm^3 and MPa, respectively. And the applied load on the upper jig is expressed in N with time (s).

The procedure for FEM simulation is depicted in Figure 4-2. The pre-process procedure includes modeling, properties setting, and meshing. After that, load with time was applied on the upper jig. Solution was carried out by adjusting options of solution control. The output results would be compared with the experiment results. If not consistent, modeling, meshing, and solution method etc. should be adjusted until the simulation results are satisfied.
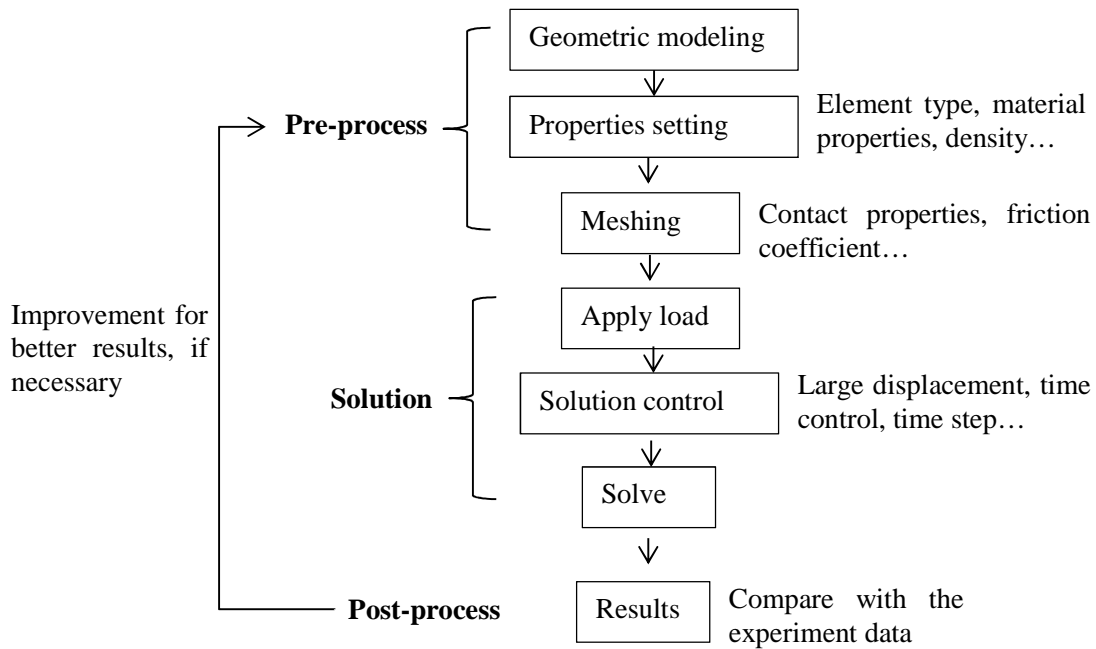
Figure 4-2 Procedure of the FEM simulation.

a Element type

There are two concepts of element property for FEM mechanical simulation, i.e., plane stress and plane strain. Plane stress[145] is defined to be a state of stress in which the normal stress, σ_z, and the shear stresses, σ_{xz} and σ_{yz} directed perpendicular to the x-y plane are assumed to be zero.

Plane strain[145] is define to be a state of strain in which the strain normal to the x-y plane, ε_z, and the shear strain γ_{xz} and γ_{yz}, are assumed to be zero. There is no displacement along the Z direction, and the mechanical response is the same in the planes which are normal to the Z direction (no change with the change of Z). Displacement in X, Y, and Z directions is:

$$Ux=Ux\ (x,y),\ Uy=Uy\ (x,y),\ Uz=0$$

Thus according to the definition the mechanical simulation of symmetric four-point bending behavior of the dissimilar-metal joint in the present study is chosen to be "plane strain" to simplify the model to 2D. And the element type is "Solid/Quad 4 node 182". Software ANSYS APDL 14.5 was utilized for the FEM simulation.

b Density of the materials

The density of a material can be calculated according to the contents of the elements[146],

$$\frac{1}{\rho} = \frac{w_1\%}{\rho_1} + \frac{w_2\%}{\rho_2} + \frac{w_3\%}{\rho_3} + \ldots \frac{w_i\%}{\rho_i}$$

Where, ρ is the density of the material, ρ_i is density of the pure alloying elements. W_i is the corresponding weight percentage.

By calculation, the density of BMs of 9Cr-ODS and JLF-1 at RT is estimated, as shown in Table 4-2. The density of the jig (Mo) at RT is from literature. While, the density of all the materials at 550^oC is estimated according to the ratio of F82H at 550^oC and RT.

Table 4-2 Density (10^{-9} ton. mm^{-3}) of the materials in the FEM simulation.

Materials	RT	550^oC
Jig (Mo)	10. 28[147]	10.05
9Cr-ODS	7.823	7.649
JLF-1	7.852	7.677
F82H[49,148]	7.871	7.695

c Material properties

In the present work the steels 9Cr-ODS and JLF-1 are considered as isotropic materials which have the same mechanical properties in all directions of X, Y, and Z. Because the bending specimens experienced permanent plastic deformation in this study, thus non-linear plastic material model is necessary in the FEM simulation. There are 3 kinds of methods for modeling non-linear plastic material behavior, i.e. bilinear model, multi-linear model, and power law model.

In this work, multi-linear material model was utilized to keep accuracy of the simulation, as shown in Figure 4-3. The strain-stress curve is divided into a number of straight lines and true strain-stress from (ε_1, σ_1) to (ε_i, σ_i) was inputted for plastic properties during FEM simulation.

σᵢ

$(\varepsilon_6, \sigma_6)$

$(\varepsilon_4, \sigma_4)$

$(\varepsilon_5, \sigma_5)$

σ_y

$(\varepsilon_3, \sigma_3)$

$(\varepsilon_2, \sigma_2)$

σ_0 $(\varepsilon_1, \sigma_1)$

0 εₜ
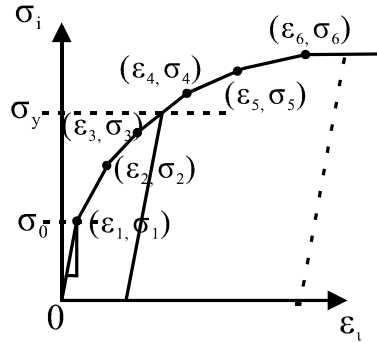
Figure 4-3 Multi-linear model of materials[149].

Elastic properties of Young's modulus and Poison's ratio of the materials are shown in Table 4-3. The elastic properties of Mo and JLF-1 are from literatures. And those of 9Cr-ODS is from the measurement by company with supersonic method[150]. In the multi-linear model, the yield strength of the materials according to experiment data is shown later in Section 4.2.

Table 4-3 Elastic properties of the materials.

Materials	Temperature	Young's modulus (10^5 MPa)	Poison's ratio
Jig(Mo)[151]	RT	3.295	0.294
	550°C	3.126	0.3
9Cr-ODS	RT	2.28	0.29
	550°C	1.82	0.3
JLF-1[101][152]	RT	2.177	0.29
	550°C	1.871	0.3

d Element size

Element size is 0.1 mm of the bending specimen and the contact areas between specimen (BMs part) and jig. The element of other areas is 0.2 mm and 0.5 mm in size.

e Friction coefficient

Friction is the force resisting the relative motion of solid surfaces of materials contacted. In the FEM simulation in this study, at the initial stage, the contact surfaces are

static friction, because of no motion between jigs and joints. Friction coefficient is defined as[153]:

$$\mu = F_f / N \qquad (4-2)$$

Where, F_f = friction force along the surface;

N = Normal reaction perpendicular to the surface.

However, after a while, there may be slipping happened. In this case dynamic friction should be considered. The dynamic friction coefficient should be a little smaller than the static friction coefficient.

The friction coefficient between BMs and jig is unknown. Thus, during the FEM simulation, the first step is for the fitting of friction coefficient between BMs and jig according to the bend experiments of BM-single-material specimens.

f About solution

Because the dissimilar-metal joint exceed more than 10% plastic deformation during the bend experiments, analysis option of "large displacement" was selected for the FEM simulation.

A load step[145] is simply a configuration of loads for which a solution is obtained. Solving an analysis with nonlinearities requires convergence of an iterative solution procedure. Convergence of this solution procedure requires the load to be applied gradually with solutions carried out at intermediate load values. These intermediate solution points within a step are referred to as sub-steps, as illustrated in Figure 4-4. Essentially a sub-step is an increment of load within a step at which a solution is carried out. The iterations carried out at each sub-step to arrive at a converged solution are referred to as equilibrium iterations. Equilibrium iterations are additional solutions calculated at a given sub-step for convergence purposes. They are iterative corrections used only in nonlinear analyses, where convergence plays an important role.
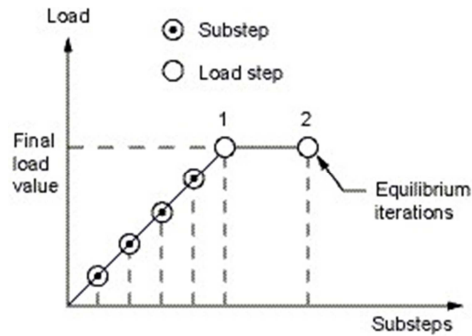
Figure 4-4 Illustration of sub-steps in the FEM simulation.

g Contact Algorithm

Four different contact algorithms can be implemented in the element: pure penalty method, augmented Lagrange method, pure Lagrange multiplier method, and Lagrange multiplier on contact normal and penalty on frictional direction.

Pure Penalty Method: This method requires both contact normal and tangential stiffness. The main drawback is that the amount penetration between the two surfaces depends on this stiffness. Higher stiffness values decrease the amount of penetration but can lead to ill-conditioning of the global stiffness matrix and to convergence difficulties. Ideally, a high enough stiffness is necessary to make that contact penetration is acceptably small, but a low enough stiffness that the problem will be well-behaved in terms of convergence or matrix ill-conditioning.

Augmented Lagrangian Method：The augmented Lagrangian method is an iterative series of penalty updates to find the Lagrange multipliers (i.e., contact tractions). Compared to the penalty method, the augmented Lagrangian method usually leads to better conditioning and is less sensitive to the magnitude of the contact stiffness coefficient. However, in some analyses, the augmented Lagrangian method may require additional iterations, especially if the deformed mesh becomes excessively distorted.

Pure Lagrange Multiplier Method: The pure Lagrange multiplier method does not require contact stiffness. Instead it requires chattering control parameters. Theoretically, the pure Lagrange multiplier method enforces zero penetration when contact is closed and "zero slip" when sticking contact occurs. However the pure Lagrange multiplier method adds additional degrees of freedom to the model and requires additional iterations to stabilize contact conditions. This will increase the computational cost. This algorithm

has chattering problems due to contact status changes between open and closed or between sliding and sticking. The other main drawback of the Lagrange multiplier method is over-constraint in the model. The model is over-constrained when a contact constraint condition at a node conflicts with a prescribed boundary condition on that degree of freedom at the same node. Over-constraints can lead to convergence difficulties and/or inaccurate results. The Lagrange multiplier method also introduces zero diagonal terms in the stiffness matrix, so that iterative solvers cannot be used.

Lagrange Multiplier on Contact Normal and Penalty on Frictional Direction: in this method only the contact normal pressure is treated as a Lagrange multiplier. The tangential contact stresses are calculated based on the penalty method. This method allows only a very small amount of slip for a sticking contact condition. It overcomes chattering problems due to contact status change between sliding and sticking which often occurs in the pure Lagrange Multiplier method. Therefore this algorithm treats frictional sliding contact problems much better than the pure Lagrange method.

The contact stiffness factor, FKN, is used to control contact penetration once contact is initiated. A smaller value provides for easier convergence, but with more penetration. For bending behavior simulation in this study, the normal penalty stiffness (FKN) is chosen to be 1.0, and the penetration tolerance (FTOLN) is 0.1.

4.2 Experiments for determination of input material parameters for simulation

PWHT was carried out at 780°C for 1h for tempering for the tensile and bending specimens of the EBW joint and the BM-single-material specimens of 9Cr-ODS and JLF-1.

a Tensile tests

Tensile tests were carried out to get the yield strength and plastic data of the BMs. The tensile tests were conducted at RT and 550°C with an initial strain rate of 6.7×10^{-4} s^{-1}.

The yield strength of 9Cr-ODS and JLF-1 BMs are shown in Table 4-4. While that of the HAZs and WM is estimated according to the hardness. The yield strength was inputted into the multi-linear model as depicted in Figure 4-3.

Table 4-4 Yield strength (σ_0) of each part in the EBW joint at RT and 550°C.

	9Cr-ODS BM	9Cr-ODS HAZ	WM	JLF-1 HAZ	JLF-1 BM
Hardness (HV)	327	346	210	175	185
RT σ_0 (MPa)	982	1039	478	398	421
550°C σ_0 (MPa)	636	673	359	298	316

The engineering strain-stress of 9Cr-ODS and JLF-1 at RT and 550°C is shown in Figure 4-5. From the engineering total strain-stress curves, plastic data was obtained. True plastic strain and stress can be calculated as follows[144],

$$\varepsilon_{tp}= \ln(1+\varepsilon_{ep}) \qquad (4\text{-}3)$$

$$\sigma_t=(1+\varepsilon_{ep})\sigma_e \qquad (4\text{-}4)$$

Where, ε_{tp} is true plastic strain, σ_t is true stress, ε_{ep} is engineering plastic strain, σ_e is engineering stress.

The true plastic strain-stress can be fitted as power law relationship, i.e., Hollomon equation[144],

$$\sigma_t=K\varepsilon_{tp}^n \qquad (4\text{-}5)$$

Where, n is hardening coefficient, K is strength index. n and K can be calculated from the slope and intercept of the $\ln\varepsilon_{tp}$-$\ln\sigma_t$ linear fit, as shown in Figure 4-6. The linear fit and the corresponding Hollomon equation for BMs of 9Cr-ODS and JLF-1 is shown in Table 4-5. As shown in Figure 4-7, the true plastic strain stress data of the BMs, WM, and HAZs was inputted in the multi-linear model during FEM simulation.
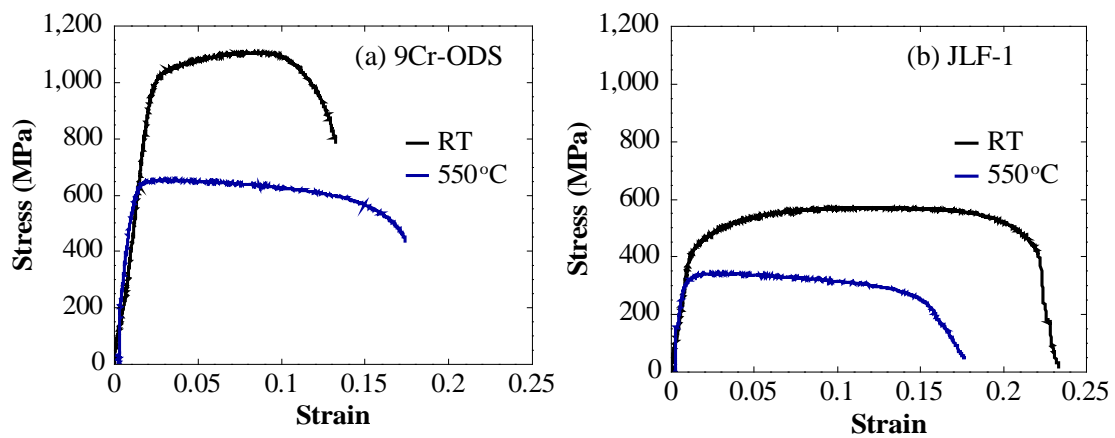
Figure 4-5 Engineering strain-stress of (a) 9Cr-ODS and (b) JLF-1 BMs at RT and 550°C.

106
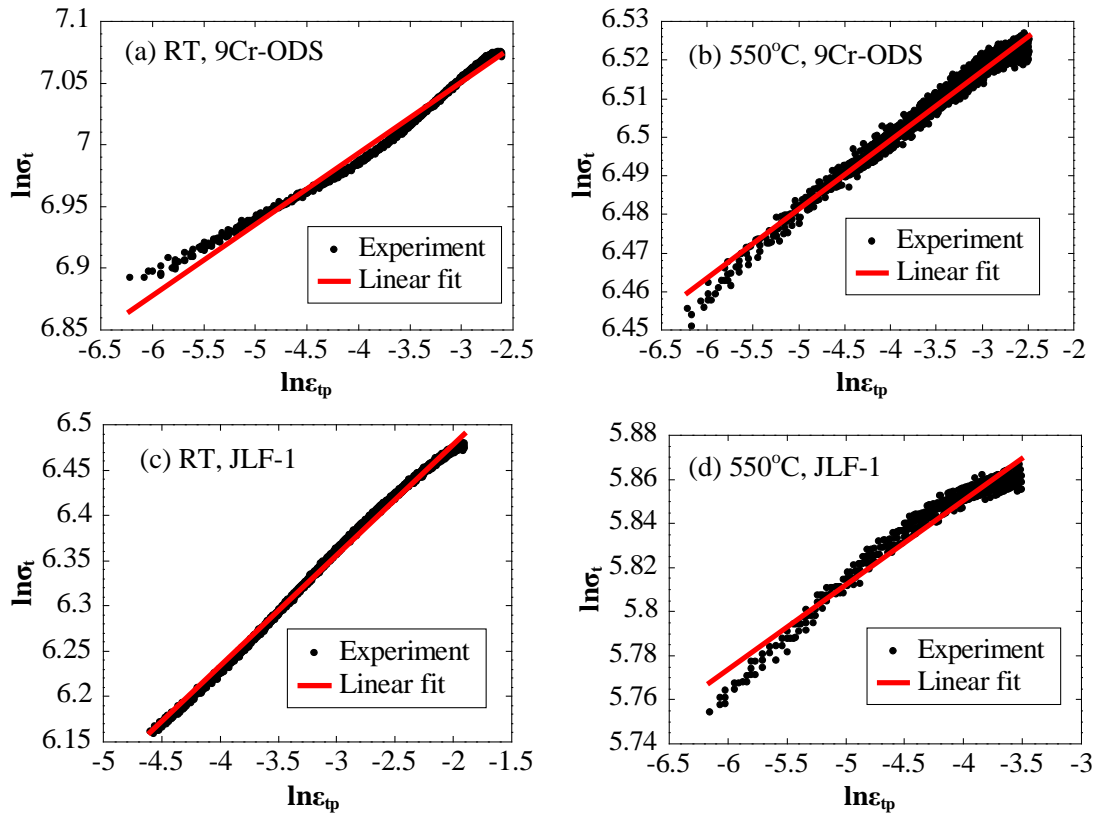
Figure 4-6 Fitting of hardening coefficient n and strength index K in the Hollomon equation for 9Cr-ODS and JLF-1 BMs at RT and 550°C.

Table 4-5 Fitting of Hollomon equation for 9Cr-ODS and JLF-1 BMs.

| | RT | | 550°C | |
	Linear fit	Hollomon equation	Linear fit	Hollomon equation
9Cr-ODS	$\ln\sigma_t=0.0576\ln\varepsilon_t+7.226$	$\sigma_t=1371\varepsilon_{tp}^{0.0576}$	$\ln\sigma_t=0.0179\ln\varepsilon_t+6.5708$	$\sigma_t=714\varepsilon_{tp}^{0.0179}$
JLF-1	$\ln\sigma_t=0.1223\ln\varepsilon_t+6.7233$	$\sigma_t=832\varepsilon_{tp}^{0.1223}$	$\ln\sigma_t=0.0382\ln\varepsilon_t+6.0032$	$\sigma_t=405\varepsilon_{tp}^{0.0382}$
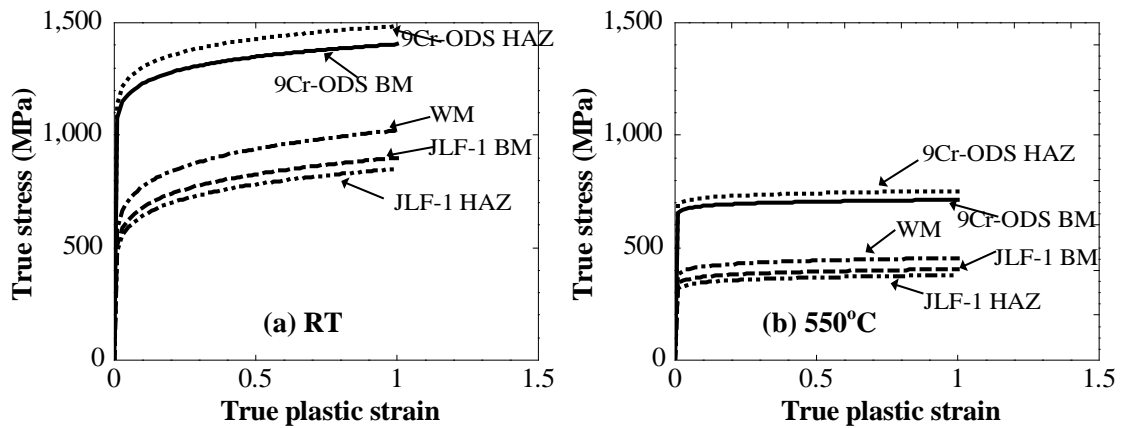
Figure 4-7 True plastic strain-stress of each part of the EBW joint at (a) RT and (b) 550°C.

b Bend tests

The width of the WM and HAZs in the dissimilar-metal joint between 9Cr-ODS and JLF-1 is 0.8 mm and 0.3 mm, respectively. The thickness and length of the joint are 1.5 mm and 20 mm. During bend experiments, the outer span is 12.5 mm, and the inner span is 5mm, as shown in Figure 4-8.

The time and displacement data during bend experiments was recorded to be inputted on the upper jig for the FEM simulation. The displacement and load data of the upper jig which was contacting to the specimens during bend experiments was used for comparison to verify the simulation reliability.
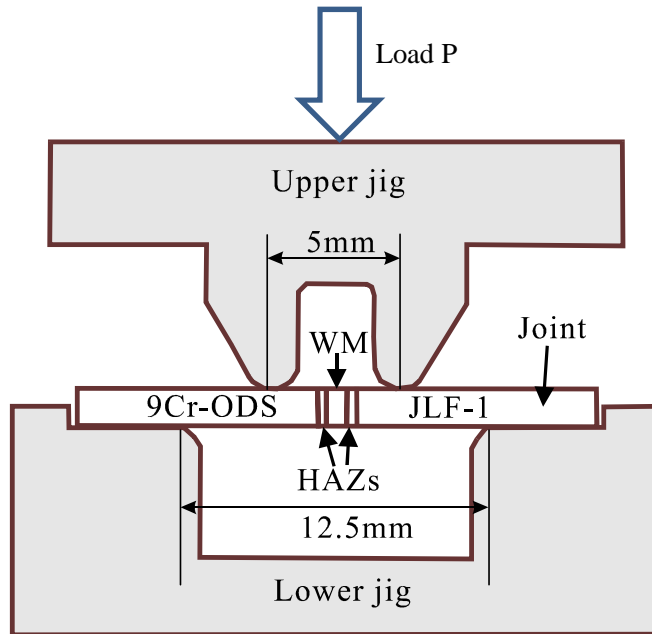
Figure 4-8 Illustration of symmetric four-point bend test.

4.3 Evaluation on bonding strength of the EBW joint of 9Cr-ODS steel—JLF-1 steel

a. Fitting of friction coefficient between the BMs and jig

The displacement and load of the upper jig was simulated at different friction coefficient between BMs and jig, as shown in Figure 4-9. The standard deviation of the results between simulation and experiment can be expressed as[154],

$$S=\sqrt{\frac{1}{n}\sum_{x=0}^{x=i}\Delta P_x{}^2} \quad (4\text{-}6)$$

For the bending of 9Cr-ODS BM-single-material specimen at RT, when the friction coefficient is 0.3, the displacement and load of the upper jig is the most coincident with the experiment, the deviation is about 9 N. Similarly, the friction coefficient is 0.5 at RT and 0.55 at 550°C between JLF-1 BM and jig. The deviation is about 13 N and 11 N respectively. According the ratio of friction coefficient between JLF-1 BM and jig at RT and 550°C, the friction coefficient between 9Cr-ODS BM and jig is estimated as 0.33 at 550°C. The friction coefficient fitted by using the software of ANSYS APDL in the

present study is only suitable in the case of "time-displacement load on the upper jig", not applicable in "time-pressure load on the upper jig". In other cases, such as by using other FEM software, the friction coefficient between BMs and jigs should be fitted again for the right simulation results.

Usually, the friction coefficient between two contact surfaces will be decreased as the temperature increases due to the tribologically generated oxide films. However, in the present work the friction coefficient between BMs and jig at 550°C is larger than that at RT. The possible reasons are, (1) RT tests were conducted in the air, while high temperature tests were in vacuum. The contact surface conditions for both the specimen and the jigs would be changed if the contact surfaces of them were oxidized in the air[155] when the bend tests were carried out at RT. The oxide film can make the friction coefficient at RT smaller than that at 550°C in this work. (2) When tests were carried out high temperature of 550°C, decomposition and evaporation of the oxide film can happen in vacuum, and lead to appearance of fresh metal surfaces[155]. In this condition, the fresh surfaces contacted and adhered directly during bend tests. Thus the friction coefficient increased. The fresh surfaces are difficult to be oxidized again in vacuum. The better the vacuum degree is, the higher the friction coefficient is. (3) On the other hand, the materials of BMs would be softened at high temperature. And because there is no thermal convection in the vacuum environment, the friction heat cannot be emitted. This can make higher temperature at the local contact surfaces. The contact areas between BMs and jig were plastic deformed and adhered at high temperature[153] tests at 550°C compared to RT. Thus the friction coefficient between BMs and jig at 550°C is higher than that at RT.
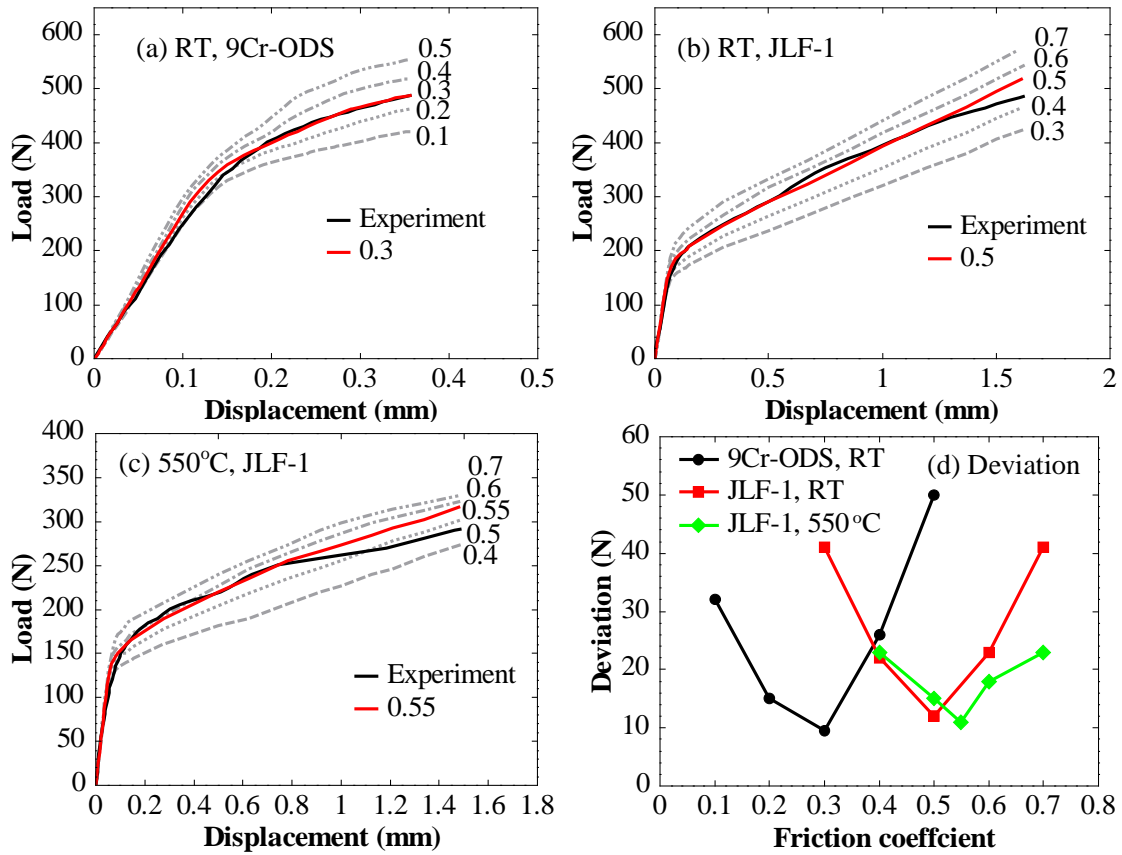
Figure 4-9 Fitting of friction coefficient between 9Cr-ODS and JLF-1 BMs and jig.

By inputting the friction coefficient fitted above mentioned, the simulated displacement and load of the upper jig during the bending of the EBW joint at RT and 550°C was shown in Figure 4-10. The standard deviation between simulation and experiment is 15 N at RT and 10 N at 550°C, respectively.
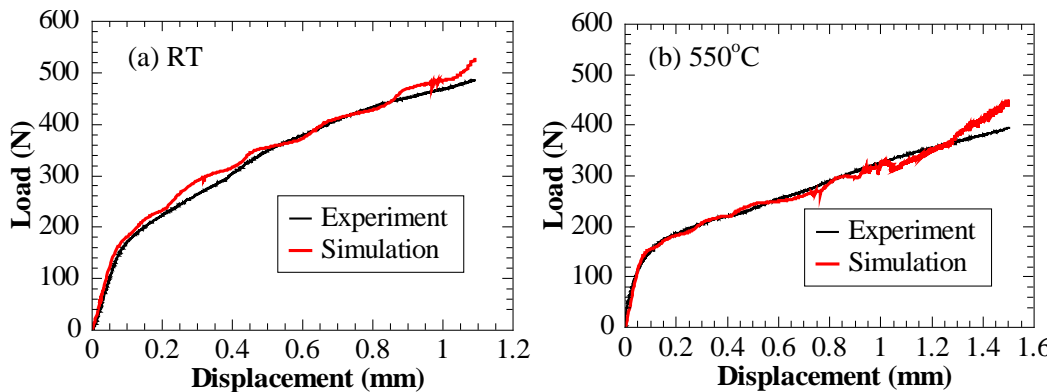
Figure 4-10 Displacement and load of the upper jig during the bending simulation for the EBW joint at (a) RT and (b) 550°C.

b. Bonding properties of the EBW joint

Figure 4-11 shows the relationship between the displacement in Y direction (perpendicular, absolute value) and normal stress in X direction (horizontal) at the bottom center of the joint. At the elastic phase, yield strength in X direction (horizontal) at the bottom center joint can be calculated as 535 MPa at RT and 413 MPa at 550°C, as shown in Table 4-6, according to $\sigma_{elastic}=\pm\frac{3}{2}\frac{P}{H}\frac{S\text{-}L}{B^2}$. The simulation results almost meet the calculation ones. To some extent, it verifies the accuracy of the simulation in this study. The maximum normal stress in X direction at the bottom center of the joint is 854 MPa at RT and 505 MPa at 550°C. Figure 4-11 also shows the distribution of normal stress in X direction at the last time during bend tests. The top of the joint undergoes compression, the bottom of the joint withstands tension, and the neutral surface has the minimum normal stress during bending. In addition, the 9Cr-ODS side and the center area of the joint have more normal stress than the JLF-1 side.
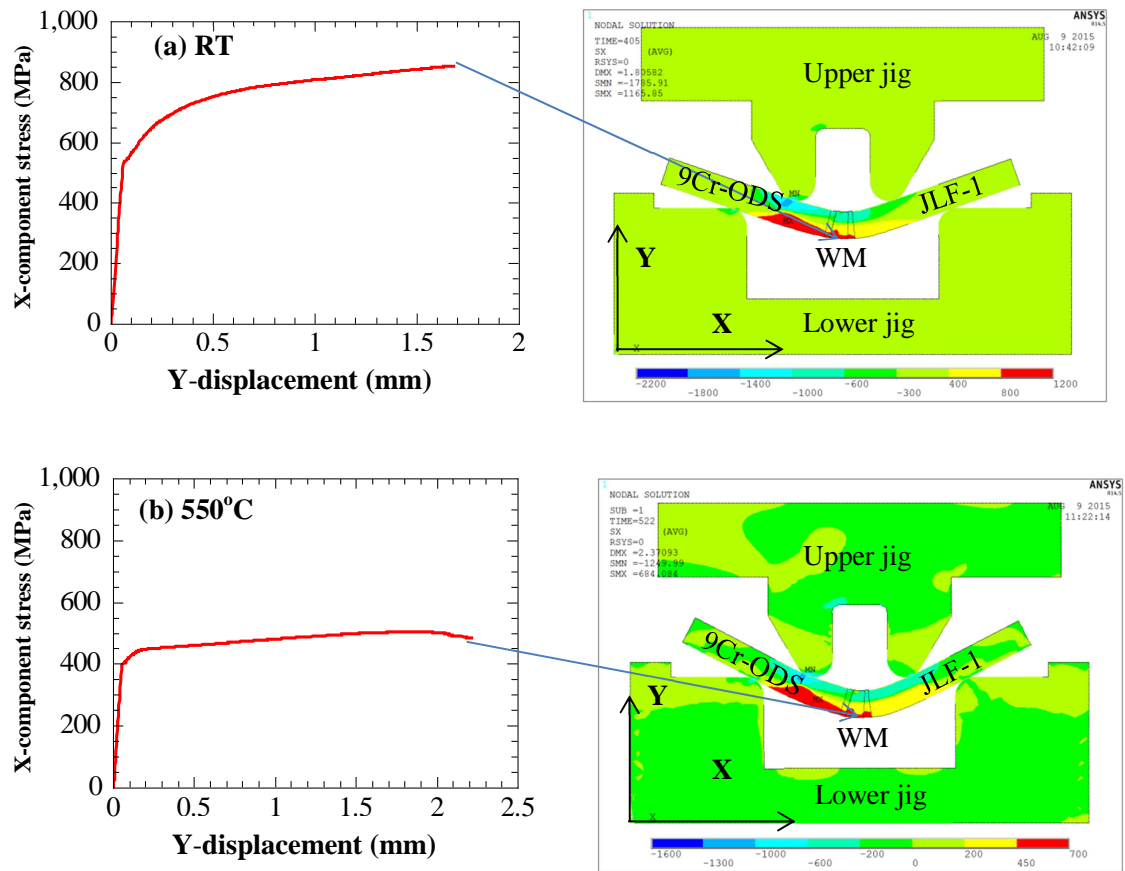
Figure 4-11 The Y-displacement and X-normal stress curve, and the distribution of X-normal stress at the last time during the bending process at the bottom center of the joint at (a) RT and (b) 550°C.

Table 4-6 Comparison of the yield strength at the bottom center of the EBW joint by FEM simulation and by elastic formula.

	Yield strength by FEM	Yield strength by elastic formula
RT	538 MPa	535 MPa
550°C	410 MPa	413 MPa

The normal stress in Y direction (across the thickness of the joint) is tiny as less than 10 MPa, and is ignorable in the present study. However, the normal stress in the Z direction (across the width of the joint) cannot be ignored. Figure 4-12 shows the normal stress in Z direction at the bottom center of the joint. It can be drawn that, the bottom center of the joint reaches the yield point at Z direction later than the X direction. The maximum Z-component stress is 422 MPa at RT and 242 MPa at 550°C. In this work, the simulation was carried out in the condition of 2D plane strain model. It was supposed that the normal stress distribution in the X-Y planes is the same in the Z direction (across

113

width of the joint), and the displacement of the joint in Z direction is zero in the present 2D model simulation. However, the homogeneity of the stress distribution in Z direction should be verified in future by 3D simulation.

Figure 4-12 also shows the von Mises stress at the bottom center of the joint. The maximum von Mises stress is 747 MPa at RT and 444 MPa at 550°C. von Mises stress is defined as follows[144],

$$\sigma_v = \left(\frac{\left(\sigma_1 - \sigma_2\right)^2 + (\sigma_2 - \sigma_3)^2 + \left(\sigma_3 - \sigma_1\right)^2}{2} \right)^{\frac{1}{2}} \qquad (4\text{-}7)$$

In the bending behavior of the present study, $\sigma_1 = \sigma_x$, $\sigma_2 = \sigma_y$, $\sigma_3 = \sigma_z$.

As mentioned above, the normal stress at Y direction (perpendicular), σ_y, is very small as less than 10 MPa at the bottom center of the joint during the four-point bend tests, and can be regarded as zero.

$$\text{Since } \sigma_z < \sigma_x,$$

$$\sigma_z - \sigma_x < 0$$

$$\sigma_z (\sigma_z - \sigma_x) < 0$$

$$\sigma_v = \left(\frac{\left(\sigma_x - \sigma_z\right)^2 + (\sigma_z)^2 + \sigma x^2}{2} \right)^{\frac{1}{2}} = \left(\sigma_x^2 + \sigma_z^2 - \sigma_x \sigma_z\right)^{\frac{1}{2}} < \sigma_x \qquad (4\text{-}8)$$

Therefore, the maximum von Mises stress 747 MPa at RT and 444 MPa at 550°C, must be smaller than the normal stress in X direction, i.e. 854 MPa at RT and 505 MPa at 550°C. von Mises stress is also important for the design of fusion blanket structure. It should be noted that, the von Mises stress should be larger than the yield strength to ensure safety operation of the joints.
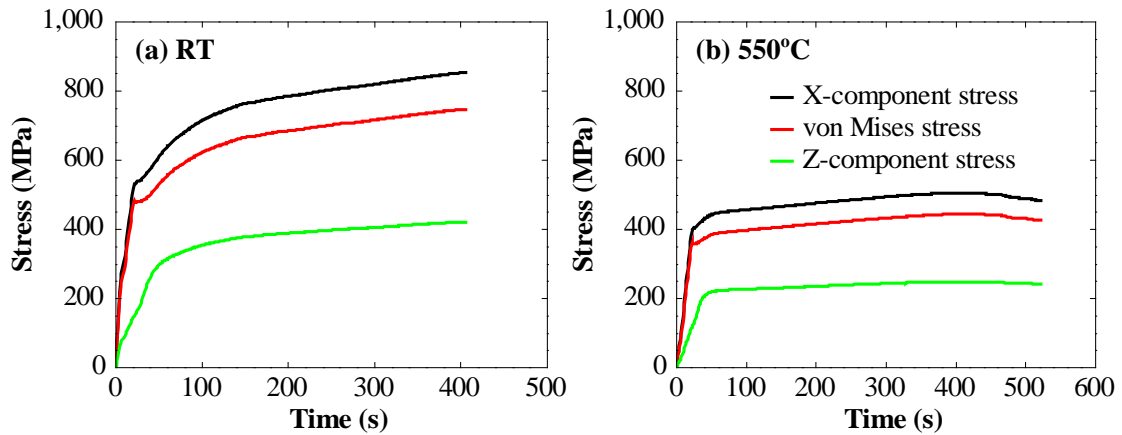
Figure 4-12 Evolution of X-component stress, Z-component stress, and von Mises stress at the bottom center of the joint at (a) RT and (b) 550°C.

The bending specimens of the joint after unloading are shown in Figure 4-13. The final shape of the specimens after simulation is almost coincident with the experiment, especially at the center area of the specimens and the 9Cr-ODS side. However, the deformation of the joint during bend experiments is more complicated than in the FEM simulation. It is impossible make the simulation completely coincident with the experiment. During bend tests the deformation of the whole dissimilar-metal joint was asymmetric. The JLF-1 part had more plastic deformation in the experiment. However, for better convergence during FEM simulation, the top center of the joint was constrained as the displacement in horizontal (X) direction was zero. This leads to the error of the simulation to some extent. By microstructural observation with OM for the joint after bend experiments, deformation traces were found at the center of the joint. It can be seen that, the HAZ of JLF-1 has the most severe local deformation there, because of the softening induced by over-tempering as depicted in Figure 3-20 and Figure 3-21.

The displacement in Y direction (deflection, towards the lower jig side) after bend experiments can be measured from the photos taken by OM, as shown in Figure 4-14. After bending, the final bottom center of the joint is not the original one anymore. The original bottom center (point a) is moved towards the 9Cr-ODS side (to point a'). The final bottom center (point b) is still in the WM, but is about 0.2 mm from the original center of the joint. Figure 4-15 (a) depicts the simulated displacement of the bottom center of the joint in X direction (towards the 9Cr-ODS side). It is 0.23 mm at RT and

115

0.25 mm at 550°C, almost agreed with the experiment. The absolute displacement in Y direction (deflection) of the final bottom center is determined as the blue lines "a-b" in Figure 4-14, i.e. 1.69 mm at RT and 2.25 mm at 550°C. The absolute displacement in Y direction (deflection) of the bottom center of the joint in the FEM simulation, 1.68 mm at RT and 2.21 mm at 550°C, as depicted in Figure 4-15 (b), is almost coincident with the experiment.

The other simulated properties at RT and 550°C at the bottom center joint are summarized in Table 4-7. The EBW joint showed large plastic deformation. The equivalent plastic strain is 0.2316 at RT and 0.27 at 550°C. The bonding strength at the bottom center is estimated larger than the maximum normal stress in X direction, i.e. 854 MPa at RT and 505 MPa at 550°C, since the specimens did not fracture after the bend experiments.
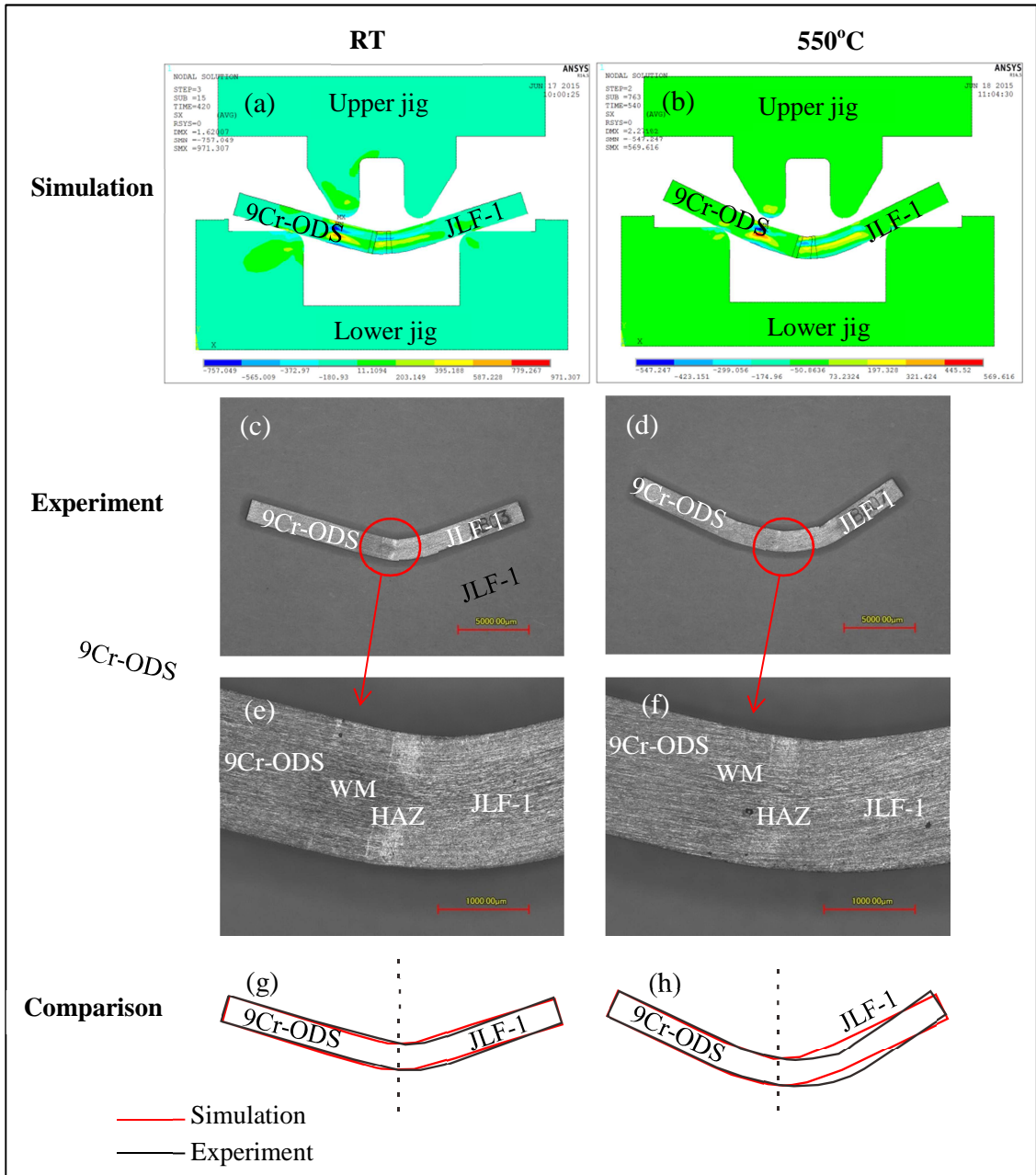
Figure 4-13 Shapes of the EBW dissimilar-metal joint between 9Cr-ODS and JLF-1 after unloading in the simulation and experiment at RT and 550°C.
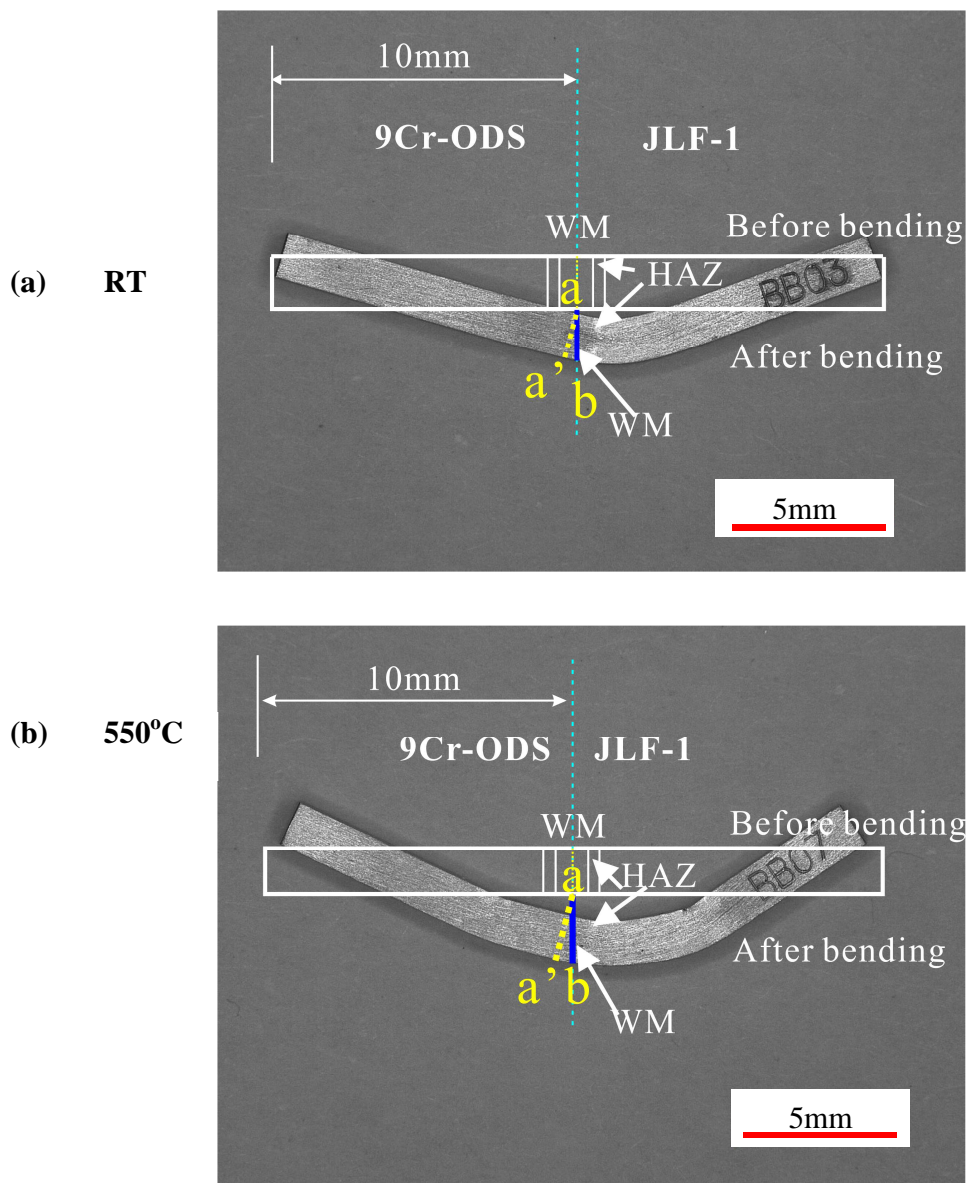
Figure 4-14 Determination of Y-displacement of the bottom center of the EBW joint between 9Cr-ODS and JLF-1 after the bend experiments at (a) RT and (b) 550$^{\mathrm{o}}$C.
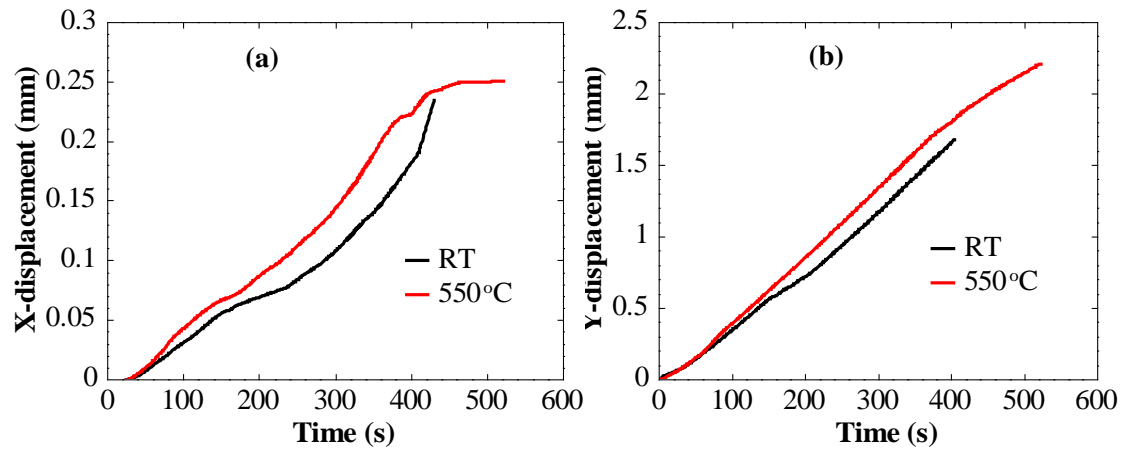
Figure 4-15 Simulated displacement of the bottom center joint in (a) X direction (towards the 9Cr-ODS side) and (b) Y direction (towards the lower jig).

Table 4-7 The simulated bonding properties at the bottom center of the EBW joint at RT and 550°C.

	RT	550°C
σ_{max} (X-component of stress), MPa	854	505
σ_{max} (von Mises stress), MPa	747	444
σ_{max} (Z-component of stress), MPa	422	242
X-component of elastic strain	0.0034	0.0023
X-component of plastic strain	0.20	0.234
Y-component of elastic strain	-0.0017	-0.0013
Y-component of plastic strain	-0.20	-0.2335
X-component of displacement, mm	-0.23	-0.25
Y-component of displacement, mm	-1.68	-2.21
Equivalent elastic strain	0.00343	0.00238
Equivalent plastic strain	0.2316	0.27

In L. Commin et al.'s work[90] on the EBW dissimilar-metal joint between ODS-RAFM steel and conventional RAFM steel, there is no result on the evaluation of bonding strength. The present work has successfully evaluated the bonding strength of the dissimilar-metal joint between 9Cr-ODS and JLF-1. The technology of four-point

119

bend tests combined with FEM simulation can be applied for the fusion blanket joints in the future.

4.4 Summary

To get the bonding properties, symmetric four-point bend experiments combined with FEM simulation were carried out for the EBW dissimilar-metal joint between 9Cr-ODS and JLF-1 at RT and 550°C. The accuracy of the FEM simulation is reflected in the following points:

(1) The displacement-load relationship of the upper jig during bending is coincident between simulation and experiment. The deviation between each other is 15 N at RT and 10 N at 550°C.

(2) At the bottom center of the joint, the yield stress at elastic phase in simulation is 538 MPa at RT and 410 MPa at 550°C. It almost has no difference with the 535 MPa at RT and 413 MPa at 550°C calculated by formula with elastic theory.

(3) The Y displacement of the bottom center joint by simulation is -1.68 mm at RT and -2.21 mm at 550°C. This is nearly agreed with the experiment of -1.69 mm at RT and -2.25 mm at 550°C.

Therefore, the FEM simulation results in the present study are believable. The maximum normal stress in X direction applied to the WM of the joint is estimated as 854 MPa at RT and 505 MPa at 550°C. Since the bending specimens were not fractured, the bonding strength is estimated to be larger than these values. The present study successfully utilized bend experiments and FEM simulation to make better estimation for the bonding strength than the tensile tests and the conventional analysis on the bend tests with elastic theory. The other bonding properties are also obtained in the present work. The stress in Z direction cannot be ignored. The homogeneity of the stress distribution in Z direction should be investigated by 3D model in the future work.

5.   Conclusions

Dissimilar-metal joints for fusion blanket structure were developed in the present work. HIP can be used for large area bonding for the thermal-protection plate bonding to the first wall. EBW can be utilized for the robust bonding for connection of coolant tubes. The mechanical properties of the joints were controlled by carbon behavior. As depicted in Figure 5-1, HIP always induced quenched martensite (carbon dissolution, hardening) for JLF-1 BM. While HIP at low temperature of 1000°C, the incomplete decomposition of carbides in ferritic structure induced softening of 9Cr-ODS BM. Decarburization also induced softening at the interface after the 1000°C-HIP. However, HIP at higher temperatures of 1050°C and 1100°C induced more decomposition of carbides and carbon dissolution for 9Cr-ODS (quenched martensite, hardening). For the EBW joints between 9Cr-ODS and JLF-1 and between F82H and 316L, carbon dissolution (quenched martensite) made hardening of WM and HAZs. Proper PWHT can recover the mechanical properties of the joints from the hardening and softening. In addition, the significant neutron hardening in the fine-grain HAZ of F82H is due to irradiation-induced precipitations from the carbon generated by the dissolution of prior carbides during the welding. The incomplete hardness recovery during PWHT at 680°C cannot make the dissolved carbides to be precipitated out and could be the source for the irradiation-induced precipitates.

(a) Joints between 9Cr-ODS and JLF-1

Interface: decarburization — Softening

HIP

9Cr-ODS BM
- 1000°C, coarse carbides — Softening
- 1050-1100°C, carbon dissolution, carbides decomposition — Hardening

JLF-1 BM: carbon dissolution — Hardening

$M_{23}C_6$ carbides

EBW

HAZs: carbon dissolution+ incomplete carbides decomposition — Hardening

WM: carbides dissolution — Hardening

PWHT: T
Softening, recovery

Carbides dissolution

PWHT: N
Hardening

(b) Joint between F82H and 316L

F82H side — $M_{23}C_6$ carbides **EBW** → Fine-grain HAZ: Carbon dissolution **680°C PWHT** → $M_{23}C_6$ carbides **Neutron irradiation** → High-density fine precipitates

Hardening — Incomplete recovery — Significant hardening

Figure 5-1 Carbon behavior in the dissimilar-metal joints at different conditions, reproduced from Figure 3-35.

The other main results in the present study are summarized as follows,

1. The dissimilar–metal joints between 9Cr-ODS and JLF-1 fabricated by HIP

The cooling rate after HIP in the present study is only 5°C/min. 1000°C-HIP induced ferrite, while 1050°C- and 1100°C-HIP induced quenched martensite for 9Cr-ODS BM. However, during the slow cooling process, coarse carbides with irregular shape always precipitated out. These coarse carbides influenced the mechanical properties of the joints. In the future work, HIP with fast cooling rate is necessary to form quenched martensite for 9Cr-ODS and avoid the formation of coarse carbides.

The above mentioned coarse carbides in 9Cr-ODS BM can be eliminated with PWHT of normalization at 1050°C with a fast cooling rate of 36°C/min. The elements in the

coarse carbides were dissolved into matrix to form quenched martensite. After the following tempering, new carbides precipitated out. The microstructure of 9Cr-ODS BM was recovered to that before HIP with tempered martensitic structure.

For the BM of JLF-1, the cooling rate after HIP is enough to form quenched martensite. PWHT with normalization and tempering is useful for the microstructure recovery to tempered martensite.

The interface is soft for all the joints after HIP at 1000 to 1100°C. For the 1000°C-HIP joint, the softening at the interface may be due to carbides coarsening (less decomposition of carbides), and decarburized few-particle layer. For the joints HIPed at higher temperatures of 1050°C and 1100°C, the softening is mainly due to carbides coarsening.

The coarse carbides at 9Cr-ODS near the interface is larger and denser than those in the BM of 9Cr-ODS. The less decomposition of carbides at the interface induced softening of 9Cr-ODS near the interface. This is a main reason why all the as-HIPed dissimilar-metal joints fractured at the interface.

1000°C is too low to bond well the dissimilar-metal joint. By the low temperature HIP, there may be un-bonded areas at the interface which was caused by the incomplete contact of the rough surfaces of the BM blocks. Even after PWHT, these un-bonded areas cannot be elapsed. In addition, there is a layer of few-particle grains existed on the JLF-1 side at the interface. The formation of few-particle layer may be caused by decarburization during HIP. Thus the joint fractured at the interface during tensile tests.

The optimum HIP temperature is 1050°C in the present study. The joint showed the best bonding strength and ductility. The 1100°C-HIP joint showed a little loss of strength probably due to grain structure coarsening. After PWHT with N&T, the bonding property was improved further, because the joints fractured at JLF-1 BM, not at the interface anymore.

In conclusion, PWHT with N&T is effective to recover microstructure and mechanical properties of BMs. But to keep good strength, HIP at the optimum temperature of 1050°C is necessary.

2. The dissimilar-metal joint between 9Cr-ODS and JLF-1 made by EBW

For the EBW dissimilar-metal joint between 9Cr-ODS and JLF-1, bonding mechanism was analyzed by microstructural characterization. The hardness of WM and HAZs in both 9Cr-ODS and JLF-1 was much higher than the BMs. The WM is quenched martensitic phase with occasionally some ferritic phase (iron metal phase with thermal equilibrium carbon in solid solution). The HAZs is also quenched martensitic phase with carbides decomposition. Two conditions of PWHT were carried out for the joints to recover the hardening and the microstructures of WM and HAZs to the levels close to the BMs.

One is only tempering at 720-780°C for 1h. The tempering removed a part of carbon in solid-solution and hardening by it, and changed the quenched martensite into tempered martensite. As tempering temperature increased, the hardening of WM and HAZs was relieved. The PWHT necessary for the complete recovery of the hardening is obtained as 780°C for 1h. However, the ferritic phase remained in the WM and softening was induced by over-tempering for BMs after the PWHT. Therefore, the other condition based on the 780°C PWHT was examined.

The other condition of PWHT is a combination of normalization at 1050°C for 1h and then tempering at 780°C for 1h. Because of the normalization, residual ferrite disappeared. The whole microstructures including WM, HAZs and BMs is quenched martensite just after the normalization. After the following tempering, the whole microstructure is tempered martensite. No residual ferrite existed anymore. The strength of the BMs was kept in the similar level as that before EBW. The PWHT is the optimum to relief the hardening of WM and HAZs, eliminate the residual ferrite, and avoid softening of BMs in the same time.

All the specimens fractured at the BM of JLF-1 steel in the tensile tests, because the interface is stronger than it. In this situation, the bonding strength cannot be determined in the same way with the HIP joints, and estimated simply as the one larger than the ultimate tensile strength of JLF-1 steel.

In order to make better estimation of the bonding strength of the joint, symmetric four-point bend tests, which can concentrate the stress inside the inner span including the WM, was executed for the joint. Generally, bend test results are analyzed with elastic deformation theory. However, a bending formula from the theory can provide the stress

condition of the present specimens up to only 0.25% in strain, though it shows larger deformation with more than 10% in strain due to plastic deformation. Thus, computer simulation with FEM was used to extend the analysis to larger deformation condition in the bend tests.

The large deformation induces sliding at the contact areas between the specimen and jig (specimen holder made of molybdenum). The sliding must be also simulated for accurate analysis, which requires an input parameter of friction coefficient at the contact. The friction coefficient was measured with a combination of bend tests on BM-single-material specimens and the simulations for them. According to the coincidence of the displacement-load curve of the upper jig in bend experiments and the simulation, the friction coefficient was determined as 0.3 for the contact between 9Cr-ODS and jig at RT, 0.5 and 0.55 between JLF-1 and jig at RT and 550°C, respectively.

In the simulation for the dissimilar-metal joint, the maximum displacement of the bottom center of the specimen is -1.68 mm at RT and -2.21 mm at 550°C, which are almost coincident with, -1.69 mm at RT and -2.25 mm at 550°C, the deformation of the specimens measured after the experiment. The simulation successfully calculated the stress distribution in the specimens up to 20.0% at RT and 23.4% at 550°C. The maximum stress applied to the bonding interface of the joint with the PWHT is estimated as 854 MPa at RT and 505 MPa at 550°C. The bonding strength is estimated to be larger than these stresses. The present study successfully made better estimation for bonding strength than the tensile tests and the conventional analysis on the bend tests with elastic deformation theory.

3. The dissimilar-metal joint between F82H and 316L made by EBW

The dissimilar-metal joint between non-ODS conventional steel and stainless steel will be used for only the cooling channel connection behind the blanket near the vacuum vessel. Therefore, only EBW process was investigated in the present study.

For the dissimilar-metal bonding between F82H and 316L in this work, the electron beam position was 0.2 mm shifted from the butting position toward 316L side according to previous studies. PWHT condition was also determined by the previous study as 680°C for 1h.

Neutron irradiation was carried out for the joint at 300°C with a neutron flux of 5.6±0.1×10^{23} n m^{-2}, which is equivalent to a dose of 0.1 dpa (displacement per atom). The joint will be located near the vacuum vessel and superconducting magnet in fusion reactors. The maximum dose for the vacuum vessel in ITER (International thermonuclear experimental reactor) has been estimated as 0.027 dpa. The neutron flux at the magnets in commercial-grade reactor design is about 1×10^{23} n m^{-2}. Since the present irradiation dose was more than these conditions, the present study can evaluate the resistance of the dissimilar-metal joint to neutron irradiation under fusion reactor condition.

Neutron irradiation induced hardening for the whole part of joint, such as BMs, WM, and HAZ. Hardness of the joint before irradiation ranged from 180 HV to 250 HV, while the one after the irradiation ranged from 230 HV to 300 HV. Significant hardening area with 450 HV in hardness and with a size of 50 μm was discovered at the fine-grain HAZ of F82H. One of possible mechanisms for the significant hardening is irradiation-induced precipitations produced by the carbides decomposed during the welding. As mentioned above, the PWHT condition with 680°C was determined mainly from the viewpoint to avoid softening of F82H steel by over-tempering. However, it was not enough to complete the recovery of the hardness change by the welding. The incomplete hardness recovery during the PWHT at 680°C indicates that the dissolved carbides still cannot be precipitated out and can be the source for the irradiation-induced precipitates. The present study found a better PWHT condition as 750°C for 1h from the viewpoint of precipitation control. This PWHT will suppress the significant irradiation hardening and should be examined under neutron irradiation in future.

Impact tests, high-speed bend tests with V-shaped notch at different positions of HAZ, BMs, and WM of the joint, were performed on the irradiated specimens. Fortunately, the significant irradiation hardening observed in the HAZ of F82H did not degrade the impact properties of the joint. This is probably because the hardening area was very limited as 50 μm in size. In addition, 316L steel part of the joint maintained much ductility and assisted the deformation of the joint during the impact tests. The present study successfully demonstrated the resistance of the joint to neutron irradiation under the commercial reactor condition.

Other topics not for the present study but for the future research on dissimilar-metal joints:

(1) More mechanical properties evaluation for the dissimilar-metal joints, such as Charpy impact tests, fatigue tests.

(2) The first wall blanket will undergo 30 to 80 dpa (displacement per atom) or even 100 to 150 dpa for the Demonstration (DEMO) or prototype commercial reactors[1]. Evaluation of neutron irradiation resistance at high dose is very important for the dissimilar-metal joints between ODS-RAFM steel and conventional RAFM steel.

(3) Thermal aging evaluation at the operation temperature of the dissimilar-metal joints.

(4) Corrosion resistance evaluation of the dissimilar-metal joints in flowing coolant of Li or FLiBe.

References

[1] V. Ghetta, D. Gorse, D. Mazière, V. Pontikis, Materials Issues for Generation IV Systems: Status, Open Questions and Challenges, Springer Science & Business Media, 2008.

[2] P.H. Yamada, Fusion Energy, in: W.-Y. Chen, J. Seiner, T. Suzuki, M. Lackner (Eds.), Handb. Clim. Change Mitig., Springer US, 2012: pp. 1183–1215.

[3] J. Jacquinot, Fifty years in fusion and the way forward, Nucl. Fusion. 50 (2010) 014001. doi:10.1088/0029-5515/50/1/014001.

[4] G.M. McCracken, P.E. Stott, Fusion: The Energy of the Universe, Academic Press, 2005.

[5] W.M. Stacey, Fusion Plasma Physics, John Wiley & Sons, 2012.

[6] Committee on the Prospects for Inertial Confinement Fusion Energy Systems, National Research Council, Division on Engineering and Physical Sciences, Board on Energy and Environmental Systems, Board on Physics and Astronomy, An Assessment of the Prospects for Inertial Fusion Energy, National Academies Press, 2013.

[7] E.I. Moses, C.R. Wuest, The National Ignition Facility: Laser Performance and First Experiments, Fusion Sci. Technol. 47 (2005) 314–322.

[8] G. Thiell, X. de la Roncière, M. Dupont, G. Coureau, P. Joyer, Dependability and Safety for Megajoule Laser Operations and Maintenance, Fusion Sci. Technol. 43 (2003) 478–483.

[9] K.M. et Al, Present Status of Fast Ignition Research and Prospects of FIREX Project, Fusion Sci. Technol. 47 (2005) 662–666.

[10] H. Azechi, F. Project, The FIREX program on the way to inertial fusion energy, J. Phys. Conf. Ser. 112 (2008) 012002. doi:10.1088/1742-6596/112/1/012002.

[11] A. Kitsunezaki, J.-60u Team, Status and Plans for JT-60U, Fusion Sci. Technol. 21 (1992) 1309–1316.

[12] J.L. et Al, Recent Progress on EAST, Fusion Sci. Technol. 64 (2013) 417–423.

[13] C. Zhou, J. Yan, Y. Liu, D. Liu, Progress of the HL-2A Project, Fusion Sci. Technol. 42 (2002) 102–106.

[14] J.-G. Kwak, Y.K. Oh, H.L. Yang, K.R. Park, Y.S. Kim, W.C. Kim, et al., An overview of KSTAR results, Nucl. Fusion. 53 (2013) 104005. doi:10.1088/0029-5515/53/10/104005.

[15] P.H. Rebut, B.E. Keen, The JET Experiment: Evolution, Present Status, and Prospects, Fusion Sci. Technol. 11 (1987) 13–42.

[16] C.A. Gentile, J.L. Anderson, P.H. LaMarche, The Operation of the Tokamak Fusion Test Reactor Tritium Facility, Fusion Sci. Technol. 28 (1995) 1327–1329.

[17] R.J. Hawryluk, D. Mueller, J. Hosea, C.W. Barnes1, M. Beer, M.G. Bell, et al., Status and Plans for TFTR, Fusion Sci. Technol. 21 (1992) 1324–1331.

[18] A. Komori, H. Yamada, S. Imagawa, O. Kaneko, K. Kawahata, K. Mutoh, et al., Goal and Achievements of Large Helical Device Project, Fusion Sci. Technol. 58 (2010) 1–11.

[19]   M.G. et Al, W7-X Progress, Fusion Sci. Technol. 47 (2005) 339–344.

[20]   P.S. Committee, B.P.A. Committee, B. on P. and Astronomy, D. on E. and P. Sciences, N.R. Council, Burning Plasma:: Bringing a Star to Earth, National Academies Press, 2004.

[21]   S. Tanaka, H. Takatsu, Japanese perspective of fusion nuclear technology from ITER to DEMO, Fusion Eng. Des. 83 (2008) 865–869. doi:10.1016/j.fusengdes.2008.06.028.

[22]   E. Gibney, Five-year delay would spell end of ITER, Nature. (2014). doi:10.1038/nature.2014.15621.

[23]   A. Sagara, O. Mitarai, S. Iamagawa, et. al., Design Integration toward optimization of LHD-type fusion reactor FFHR, Proceedings of ITC/ISHW2007.

[24]   Y. Igitkhanov, B. Bazylev, Evaluation of energy and particle impact on the plasma facing components in DEMO, Fusion Eng. Des. 87 (2012) 520–524. doi:10.1016/j.fusengdes.2012.01.013.

[25]   M. Gasparotto, L.V. Boccaccini, L. Giancarli, S. Malang, Y. Poitevin, Demo blanket technology R&D results in EU, Fusion Eng. Des. 61–62 (2002) 263–271. doi:10.1016/S0920-3796(02)00170-9.

[26]   K. Ehrlich, E.E. Bloom, T. Kondo, International strategy for fusion materials development, J. Nucl. Mater. 283–287, Part 1 (2000) 79–88. doi:10.1016/S0022-3115(00)00102-1.

[27]   J.-F. Salavy, G. Aiello, P. Aubert, L.V. Boccaccini, M. Daichendt, G. De Dinechin, et al., Ferritic–Martensitic steel Test Blanket Modules: Status and future needs for design criteria requirements and fabrication validation, J. Nucl. Mater. 386–388 (2009) 922–926. doi:10.1016/j.jnucmat.2008.12.239.

[28]   P. Rocco, M. Zucchetti, Criteria for defining low activation materials in fusion reactor applications, Fusion Eng. Des. 15 (1991) 235–244. doi:10.1016/0920-3796(92)90042-3.

[29]   Y. Seki, T. Tabara, I. Aoki, S. Ueda, S. Nishio, R. Kurihara, Composition adjustment of low activation materials for shallow land burial, Fusion Eng. Des. 48 (2000) 435–441. doi:10.1016/S0920-3796(00)00152-6.

[30]   P. Rocco, M. Zucchetti, Recycling and clearance of fusion activated waste, J. Nucl. Mater. 233–237, Part 2 (1996) 1500–1504. doi:10.1016/S0022-3115(96)00141-9.

[31]   P. Rocco, M. Zucchetti, Waste management for different fusion reactor designs, J. Nucl. Mater. 283–287, Part 2 (2000) 1473–1477. doi:10.1016/S0022-3115(00)00127-6.

[32]   A.R. Raffray, M. Akiba, V. Chuyanov, L. Giancarli, S. Malang, Breeding blanket concepts for fusion and materials requirements, J. Nucl. Mater. 307–311, Part 1 (2002) 21–30. doi:10.1016/S0022-3115(02)01174-1.

[33]   K. Abe, A. Kohyama, S. Tanaka, C. Namba, T. Terai, T. Kunugi, et al., Development of advanced blanket performance under irradiation and system integration through JUPITER-II project, Fusion Eng. Des. 83 (2008) 842–849. doi:10.1016/j.fusengdes.2008.07.028.

[34]   S. Mori, S. Yamazaki, J. Adachi, T. Kobayashi, S. Nishio, M. Kikuchi, et al., Blanket and divertor design for the Steady State Tokamak Reactor (SSTR), Fusion Eng. Des. 18 (1991) 249–258. doi:10.1016/0920-3796(91)90135-D.

[35] M. Kikuchi, Y. Seki, A. Oikawa, T. Ando, Y. Ohara, S. Nishio, et al., Conceptual design of the steady state tokamak reactor (SSTR), Fusion Eng. Des. 18 (1991) 195–202. doi:10.1016/0920-3796(91)90127-C.

[36] S. Mori, H. Miura, S. Yamazaki, T. Suzuki, A. Shimizu, Y. Seki, et al., Preliminary Design of a Solid Particulate Cooled Blanket for the Steady State Tokamak Reactor (SSTR), Fusion Sci. Technol. 21 (1992) 1744–1748.

[37] F. Najmabadi, C.G. Bathke, M.C. Billone, J.P. Blanchard, L. Bromberg, E. Chin, et al., Overview of the ARIES-RS reversed-shear tokamak power plant study, Fusion Eng. Des. 38 (1997) 3–25. doi:10.1016/S0920-3796(97)00110-5.

[38] L.A. El-Guebaly, Overview of ARIES-RS neutronics and radiation shielding: key issues and main conclusions, Fusion Eng. Des. 38 (1997) 139–158. doi:10.1016/S0920-3796(97)00114-2.

[39] M.S. Tillack, Engineering design of the ARIES-RS power plant, Fusion Eng. Des. 41 (1998) 491–499. doi:10.1016/S0920-3796(97)00161-0.

[40] H. Kai-hui, S. Nishio, Thermo-Mechanical Design Considerations for First Wall of A-SSTR2, Plasma Sci. Technol. 5 (2003) 1651. doi:10.1088/1009-0630/5/1/009.

[41] A. Sagara, O. Mitarai, S. Imagawa, T. Morisaki, T. Tanaka, N. Mizuguchi, et al., Conceptual design activities and key issues on LHD-type reactor FFHR, Fusion Eng. Des. 81 (2006) 2703–2712. doi:10.1016/j.fusengdes.2006.07.057.

[42] A.-A.F. Tavassoli, E. Diegele, R. Lindau, N. Luzginova, H. Tanigawa, Current status and recent research achievements in ferritic/martensitic steels, J. Nucl. Mater. 455 (2014) 269–276. doi:10.1016/j.jnucmat.2014.06.017.

[43] T. Muroga, M. Gasparotto, S.J. Zinkle, Overview of materials research for fusion reactors, Fusion Eng. Des. 61–62 (2002) 13–25. doi:10.1016/S0920-3796(02)00219-3.

[44] R.L. Klueh, D.S. Gelles, S. Jitsukawa, A. Kimura, G.R. Odette, B. van der Schaaf, et al., Ferritic/martensitic steels – overview of recent results, J. Nucl. Mater. 307–311, Part 1 (2002) 455–465. doi:10.1016/S0022-3115(02)01082-6.

[45] G.J. Butterworth, S.R. Keown, The commercial production of high-purity low-activation steels for fusion reactor application, J. Nucl. Mater. 186 (1992) 283–287. doi:10.1016/0022-3115(92)90348-O.

[46] G.J. Butterworth, L. Giancarli, Some radiological limitations on the compositions of low-activation materials for power reactors, J. Nucl. Mater. 155–157, Part 2 (1988) 575–580. doi:10.1016/0022-3115(88)90374-1.

[47] T. Muroga, Vanadium Alloys for Fusion Blanket Applications, Mater. Trans. - MATER TRANS. 46 (2005) 405–411. doi:10.2320/matertrans.46.405.

[48] B. Raj, M. Vijayalakshmi, 4.03 - Ferritic Steels and Advanced Ferritic–Martensitic Steels, in: R.J.M. Konings (Ed.), Compr. Nucl. Mater., Elsevier, Oxford, 2012: pp. 97–121.

[49] A.-A.F. Tavassoli, J.-W. Rensman, M. Schirra, K. Shiba, Materials design data for reduced activation martensitic steel type F82H, Fusion Eng. Des. 61–62 (2002) 617–628. doi:10.1016/S0920-3796(02)00255-7.

[50] A. Kohyama, Y. Kohno, M. Kuroda, A. Kimura, F. Wan, Production of low activation steel; JLF-1, large heats – Current status and future plan, J. Nucl. Mater. 258–263, Part 2 (1998) 1319–1323. doi:10.1016/S0022-3115(98)00198-6.

[51]   K. Mergia, N. Boukos, Structural, thermal, electrical and magnetic properties of Eurofer 97 steel, J. Nucl. Mater. 373 (2008) 1–8. doi:10.1016/j.jnucmat.2007.03.267.

[52]   P. Wang, J. Chen, H. Fu, S. Liu, X. Li, Z. Xu, Effect of N on the precipitation behaviours of the reduced activation ferritic/martensitic steel CLF-1 after thermal ageing, J. Nucl. Mater. 442 (2013) S9–S12. doi:10.1016/j.jnucmat.2013.03.081.

[53]   Q. Huang, Development status of CLAM steel for fusion application, J. Nucl. Mater. 455 (2014) 649–654. doi:10.1016/j.jnucmat.2014.08.055.

[54]   R.L. Klueh, D.J. Alexander, M. Rieth, The effect of tantalum on the mechanical properties of a 9Cr–2W–0.25V–0.07Ta–0.1C steel1, J. Nucl. Mater. 273 (1999) 146–154. doi:10.1016/S0022-3115(99)00035-5.

[55]   Y. Li, T. Nagasaka, T. Muroga, A. Kimura, S. Ukai, High-temperature mechanical properties and microstructure of 9Cr oxide dispersion strengthened steel compared with RAFMs, Fusion Eng. Des. 86 (2011) 2495–2499. doi:10.1016/j.fusengdes.2011.03.004.

[56]   T. Muroga, T. Nagasaka, Y. Li, H. Abe, S. Ukai, A. Kimura, et al., Fabrication and characterization of reference 9Cr and 12Cr-ODS low activation ferritic/martensitic steels, Fusion Eng. Des. 89 (2014) 1717–1722. doi:10.1016/j.fusengdes.2014.01.010.

[57]   Kaito T, Mizuta S, Uwaba T, Ohtsuka S, Ukai, S,The Tentative Materials Strength Standard of ODS Ferritic Steel claddings, JNC TN9400 2005-015, Japan Atomic Energy Agency, 2005, in Japanese.

[58]   J. Isselin, R. Kasada, A. Kimura, T. Okuda, M. Inoue, S. Ukai, et al., Evaluation of fracture behavior of recrystallized and aged high-Cr ODS ferritic steels, J. Nucl. Mater. 417 (2011) 185–188. doi:10.1016/j.jnucmat.2010.12.061.

[59]   P. Dou, A. Kimura, R. Kasada, T. Okuda, M. Inoue, S. Ukai, et al., Effects of titanium concentration and tungsten addition on the nano-mesoscopic structure of high-Cr oxide dispersion strengthened (ODS) ferritic steels, J. Nucl. Mater. 442 (2013) S95–S100. doi:10.1016/j.jnucmat.2013.04.090.

[60]   C. Shin, S. Lim, H. Jin, P. Hosemann, J. Kwon, Development and testing of microcompression for post irradiation characterization of ODS steels, J. Nucl. Mater. 444 (2014) 43–48. doi:10.1016/j.jnucmat.2013.09.025.

[61]   A. Paúl, E. Alves, L.C. Alves, C. Marques, R. Lindau, J.A. Odriozola, Microstructural characterization of Eurofer-ODS RAFM steel in the normalized and tempered condition and after thermal aging in simulated fusion conditions, Fusion Eng. Des. 75–79 (2005) 1061–1065. doi:10.1016/j.fusengdes.2005.06.334.

[62]   R. Mateus, P.A. Carvalho, D. Nunes, L.C. Alves, N. Franco, J.B. Correia, et al., Microstructural characterization of the ODS Eurofer 97 EU-batch, Fusion Eng. Des. 86 (2011) 2386–2389. doi:10.1016/j.fusengdes.2011.01.011.

[63]   R. Lindau, M. klimiankou, A. Moslang, M. Rieth, B. Schedler, J. Schroder, A. Schwaiger, ODS-EUROFER-A Reduced Activation Ferritic Martensitic ODS-Steel for Structural Applications in Future Nuclear Fusion Reactors, Proceeding of the 16th International Plansee Seminar, Austria, 2005.

[64]   A. Steckmeyer, V.H. Rodrigo, J.M. Gentzbittel, V. Rabeau, B. Fournier, Tensile anisotropy and creep properties of a Fe–14CrWTi ODS ferritic steel, J. Nucl. Mater. 426 (2012) 182–188. doi:10.1016/j.jnucmat.2012.03.016.

[65] X. Liu, J.M. Chen, P.F. Zheng, P.H. Wang, J.H. Wu, Y.Y. Lian, Y. J. Feng, K. M. Feng, Z. Y. Xu, X. R. Duan, Y. Liu, Overview of fusion reactor materials study at SWIP, 25th IAEA Fusion Energy Conference, 13-18 October, 2014, Saint Petersburg, Russia.

[66] C. Lu, Z. Lu, C. Liu, Microstructure of nano-structured ODS CLAM steel by mechanical alloying and hot isostatic pressing, J. Nucl. Mater. 442 (2013) S148–S152. doi:10.1016/j.jnucmat.2013.01.297.

[67] A. Kohyama, A. Hishinuma, D.S. Gelles, R.L. Klueh, W. Dietz, K. Ehrlich, Low-activation ferritic and martensitic steels for fusion application, J. Nucl. Mater. 233–237, Part 1 (1996) 138–147. doi:10.1016/S0022-3115(96)00327-3.

[68] A. Cardella, E. Rigal, L. Bedel, P. Bucci, J. Fiek, L. Forest, et al., The manufacturing technologies of the European breeding blankets, J. Nucl. Mater. 329–333, Part A (2004) 133–140. doi:10.1016/j.jnucmat.2004.04.014.

[69] 畠山耕一　他, 代替溶接法による ODS 鋼被覆管/端栓接合部の強度 評価, JNC-TN9400 2001-110.

[70] R. Lindau, M. Klimenkov, U. Jäntsch, A. Möslang, L. Commin, Mechanical and microstructural characterization of electron beam welded reduced activation oxide dispersion strengthened – Eurofer steel, J. Nucl. Mater. 416 (2011) 22–29. doi:10.1016/j.jnucmat.2011.01.025.

[71] W. Sittel, W.W. Basuki, J. Aktaa, Diffusion bonding of the oxide dispersion strengthened steel PM2000, J. Nucl. Mater. 443 (2013) 78–83. doi:10.1016/j.jnucmat.2013.06.048.

[72] S. Noh, A. Kimura, T.K. Kim, Diffusion bonding of 9Cr ODS ferritic/martensitic steel with a phase transformation, Fusion Eng. Des. 89 (2014) 1746–1750. doi:10.1016/j.fusengdes.2013.12.023.

[73] W. Han, A. Kimura, N. Tsuda, H. Serizawa, D. Chen, H. Je, et al., Effects of mechanical force on grain structures of friction stir welded oxide dispersion strengthened ferritic steel, J. Nucl. Mater. 455 (2014) 46–50. doi:10.1016/j.jnucmat.2014.03.027.

[74] 秀男遠藤, 正之関, 藤雄石橋, 藤雄石橋, 一仁平子, 竜也塚田, 抵抗溶接試験結果報告(基本特性把握試験結果 その 2), JNC-TN8430 2000-002. (1999) 1–30.

[75] M. Seki, K. Hirako, S. Kono, Y. Kihara, T. Kaito, S. Ukai, Pressurized resistance welding technology development in 9Cr-ODS martensitic steels, J. Nucl. Mater. 329–333, Part B (2004) 1534–1538. doi:10.1016/j.jnucmat.2004.04.172.

[76] T. Nozawa, S. Noh, H. Tanigawa, Determining the shear fracture properties of HIP joints of reduced-activation ferritic/martensitic steel by a torsion test, J. Nucl. Mater. 427 (2012) 282–289. doi:10.1016/j.jnucmat.2012.05.019.

[77] T. Hirose, K. Shiba, M. Ando, M. Enoeda, M. Akiba, Joining technologies of reduced activation ferritic/martensitic steel for blanket fabrication, Fusion Eng. Des. 81 (2006) 645–651. doi:10.1016/j.fusengdes.2005.07.015.

[78] H. Kishimoto, T. Ono, H. Sakasegawa, H. Tanigawa, M. Ando, T. Shibayama, et al., Oxide formation and precipitation behaviors on interface of F82H steel joints during HIPing and hot pressing, J. Nucl. Mater. 442 (2013) S546–S551. doi:10.1016/j.jnucmat.2013.03.003.

[79]   T. Sawai, K. Shiba, A. Hishinuma, Microstructure of welded and thermal-aged low activation steel F82H IEA heat, J. Nucl. Mater. 283–287, Part 1 (2000) 657–661. doi:10.1016/S0022-3115(00)00089-1.

[80]   T. Nakata, H. Tanigawa, Evaluation of local deformation behavior accompanying fatigue damage in F82H welded joint specimens by using digital image correlation, Fusion Eng. Des. 87 (2012) 589–593. doi:10.1016/j.fusengdes.2012.01.048.

[81]   S.W. Kim, H.K. Yoon, W.J. Park, A. Kohyama, Fatigue crack growth behavior of JLF-1 steel including TIG weldments, J. Nucl. Mater. 329–333, Part A (2004) 248–251. doi:10.1016/j.jnucmat.2004.04.019.

[82]   Q. Zhu, Y. Lei, X. Chen, W. Ren, X. Ju, Y. Ye, Microstructure and mechanical properties in TIG welding of CLAM steel, Fusion Eng. Des. 86 (2011) 407–411. doi:10.1016/j.fusengdes.2011.03.070.

[83]   Y. Zhao, C. Li, B. Huang, S. Liu, Q. Huang, Verification of the effect of surface preparation on Hot Isostatic Pressing diffusion bonding joints of CLAM steel, J. Nucl. Mater. 455 (2014) 486–490. doi:10.1016/j.jnucmat.2014.08.004.

[84]   C. Li, Q. Huang, Q. Wu, S. Liu, Y. Lei, T. Muroga, et al., Welding techniques development of CLAM steel for Test Blanket Module, Fusion Eng. Des. 84 (2009) 1184–1187. doi:10.1016/j.fusengdes.2008.12.039.

[85]   J.M. Chen, P.H. Wang, H.Y. Fu, Z.Y. Xu, Research of low activation structural material for fusion reactor in SWIP, the 24th IAEA Fusion Energy Conference, 8-13 October, 2012, San Diego, California, USA.

[86]   R. Montanari, G. Filacchioni, B. Riccardi, M.E. Tata, G. Costanza, Characterization of Eurofer-97 TIG-welded joints by FIMEC indentation tests, J. Nucl. Mater. 329–333, Part B (2004) 1529–1533. doi:10.1016/j.jnucmat.2004.04.173.

[87]   Y. Poitevin, P. Aubert, E. Diegele, G. de Dinechin, J. Rey, M. Rieth, et al., Development of welding technologies for the manufacturing of European Tritium Breeder blanket modules, J. Nucl. Mater. 417 (2011) 36–42. doi:10.1016/j.jnucmat.2010.12.259.

[88]   S. Noh, R. Kasada, A. Kimura, Solid-state diffusion bonding of high-Cr ODS ferritic steel, Acta Mater. 59 (2011) 3196–3204. doi:10.1016/j.actamat.2011.01.059.

[89]   R. Lindau, A. Möslang, M. Rieth, M. Klimiankou, E. Materna-Morris, A. Alamo, et al., Present development status of EUROFER and ODS-EUROFER for application in blanket concepts, Fusion Eng. Des. 75–79 (2005) 989–996. doi:10.1016/j.fusengdes.2005.06.186.

[90]   L. Commin, M. Rieth, V. Widak, B. Dafferner, S. Heger, H. Zimmermann, et al., Characterization of ODS (Oxide Dispersion Strengthened) Eurofer/Eurofer dissimilar electron beam welds, J. Nucl. Mater. 442 (2013) S552–S556. doi:10.1016/j.jnucmat.2012.11.019.

[91]   S. Noh, B. Kim, R. Kasada, A. Kimura, Diffusion bonding between ODS ferritic steel and F82H steel for fusion applications, J. Nucl. Mater. 426 (2012) 208–213. doi:10.1016/j.jnucmat.2012.02.024.

[92]   T. Uwaba, S. Ukai, T. Nakai, M. Fujiwara, Properties of friction welds between 9Cr-ODS martensitic and ferritic–martensitic steels, J. Nucl. Mater. 367–370, Part B (2007) 1213–1217. doi:10.1016/j.jnucmat.2007.03.221.

[93]   D.T. Hoelzer, K.A. Unocic, M.A. Sokolov, Z. Feng, Joining of 14YWT and F82H by friction stir welding, J. Nucl. Mater. 442 (2013) S529–S534. doi:10.1016/j.jnucmat.2013.04.027.

[94]   Y.D. Chung, H. Fujii, Y. Sun, H. Tanigawa, Interface microstructure evolution of dissimilar friction stir butt welded F82H steel and SUS304, Mater. Sci. Eng. A. 528 (2011) 5812–5821. doi:10.1016/j.msea.2011.04.023.

[95]   S. Nogami, N. Hara, T. Nagasaka, A. Hasegawa, T. Muroga, Effect of PWHT on the Mechanical and Metallographical Properties of a Dissimilar-Metal Weld Joint of F82H and SUS316L Steels, Fusion Sci. Technol. 60 (2011) 334–338.

[96]   N. Hara, S. Nogami, T. Nagasaka, A. Hasegawa, H. Tanigawa, T. Muroga, Mechanical property changes and irradiation hardening due to dissimilar metal welding with reduced activation ferritic/martensitic steel and 316L stainless steel, Fusion Sci. Technol. 56 (2009) 318–322.

[97]   H. Serizawa, D. Mori, Y. Shirai, H. Ogiwara, H. Mori, Weldability of dissimilar joint between F82H and SUS316L under fiber laser welding, Fusion Eng. Des. 88 (2013) 2466–2470. doi:10.1016/j.fusengdes.2013.03.041.

[98]   K. Furuya, M. Ida, M. Miyashita, H. Nakamura, Mechanical properties of F82H/316L and 316L/316L welds upon the target back-plate of IFMIF, J. Nucl. Mater. 386–388 (2009) 963–966. doi:10.1016/j.jnucmat.2008.12.259.

[99]   T. Nishitani, H. Tanigawa, T. Nozawa, S. Jitsukawa, M. Nakamichi, T. Hoshino, et al., Recent progress in blanket materials development in the Broader Approach activities, J. Nucl. Mater. 417 (2011) 1331–1335. doi:10.1016/j.jnucmat.2010.12.304.

[100]   S. Kou, Welding Metallurgy, John Wiley & Sons, 2003.

[101]   K. Shiba, N. Yamanouchi, A. Tohyama, Preliminary results of the round-robin testing of F82H.

[102]   T. Nagasaka, Y. Hishinuma, T. Muroga, H. Watanabe, H. Sakasegawa, H. Tanigawa, et al., Analysis on precipitation behavior of reduced activation ferritic/martensitic steels with extraction residue tests, Fusion Eng. Des. 88 (2013) 2565–2568. doi:10.1016/j.fusengdes.2013.05.037.

[103]   C.P. Dillon, Corrosion Resistance of Stainless Steels, CRC Press, 1995.

[104]   P.J. Maziasz, J.T. Busby, 2.09 - Properties of Austenitic Steels for Nuclear Reactor Applications, in: R.J.M. Konings (Ed.), Compr. Nucl. Mater., Elsevier, Oxford, 2012: pp. 267–283.

[105]   J. Gan, B. A. Hilton, TEM Examination of Advanced Alloys Irradiated in ATR, Report of Idaho National Laboratory, 2007.

[106]   L. Toualbi, C. Cayron, P. Olier, J. Malaplate, M. Praud, M.-H. Mathon, et al., Assessment of a new fabrication route for Fe–9Cr–1W ODS cladding tubes, J. Nucl. Mater. 428 (2012) 47–53. doi:10.1016/j.jnucmat.2011.12.013.

[107]   M. Rieth, M. Schirra, A. Falkenstein, P. Graf, S. Heger, H. Kempe, R. Lindau, H. Zimmermann, Eurofer 97-tensile, charpy, creep and structural tests, FZK Report 6911, 2003.

[108]   L. Tan, Y. Yang, J.T. Busby, Effects of alloying elements and thermomechanical treatment on 9Cr Reduced Activation Ferritic–Martensitic (RAFM) steels, J. Nucl. Mater. 442 (2013) S13–S17. doi:10.1016/j.jnucmat.2012.10.015.

[109]   K.E. Easterling, Introduction to the physical metallurgy of welding, Butterworth Heinemann, 1992.

[110] K. Furuya, E. Wakai, M. Ando, T. Sawai, A. Iwabuchi, K. Nakamura, et al., Tensile and impact properties of F82H steel applied to HIP-bond fusion blanket structures, Fusion Eng. Des. 69 (2003) 385–389. doi:10.1016/S0920-3796(03)00079-6.

[111] S. Sam, C.R. Das, V. Ramasubbu, S.K. Albert, A.K. Bhaduri, T. Jayakumar, et al., Delta ferrite in the weld metal of reduced activation ferritic martensitic steel, J. Nucl. Mater. 455 (2014) 343–348. doi:10.1016/j.jnucmat.2014.07.008.

[112] S. Ukai, Microstructure and High-Temperature Strength of 9CrODS Ferritic Steel, in: J. Cuppoletti (Ed.), Met. Ceram. Polym. Compos. Var. Uses, InTech, 2011.

[113] P.J. Maziasz, Formation and stability of radiation-induced phases in neutron-irradiated austenitic and ferritic steels, J. Nucl. Mater. 169 (1989) 95–115. doi:10.1016/0022-3115(89)90525-4.

[114] G. Kalinin, W. Gauster, R. Matera, A.-A.F. Tavassoli, A. Rowcliffe, S. Fabritsiev, et al., Structural materials for ITER in-vessel component design, J. Nucl. Mater. 233–237, Part 1 (1996) 9–16. doi:10.1016/S0022-3115(96)00316-9.

[115] Y. Asaoka, K. Okano, T. Yoshida, K. Tomabechi, Y. Ogawa, N. Sekimura, et al., Conceptual design of a breeding blanket with super-heated steam cycle for CREST-1, Fusion Eng. Des. 48 (2000) 397–405. doi:10.1016/S0920-3796(00)00149-6.

[116] L.A. El-Guebaly, Nuclear performance assessment of ARIES-AT, Fusion Eng. Des. 80 (2006) 99–110. doi:10.1016/j.fusengdes.2005.06.355.

[117] H. Oka, N. Hashimoto, T. Muroga, A. Kimura, M.A. Sokolov, T. Yamamoto, et al., Hardness distribution and tensile properties in an electron beam weldment of F82H irradiated in HFIR, J. Nucl. Mater. 455 (2014) 454–459. doi:10.1016/j.jnucmat.2014.07.076.

[118] J. Rensman, E.V. van Osch, M.G. Horsten, D.S. d'Hulst, Post-irradiation mechanical tests on F82H EB and TIG welds, J. Nucl. Mater. 283–287, Part 2 (2000) 1201–1205. doi:10.1016/S0022-3115(00)00152-5.

[119] H. Bhadeshia, R. Honeycombe, Steels: Microstructure and Properties, Third Edition, 3 edition, Butterworth-Heinemann, Amsterdam ; Boston, 2006.

[120] A. von der Weth, H. Kempe, B. Dafferner, Deterioration of EUROFER plates by severe bending, J. Nucl. Mater. 359 (2006) 150–154. doi:10.1016/j.jnucmat.2006.08.002.

[121] H. Tanigawa, K. Shiba, A. Möslang, R.E. Stoller, R. Lindau, M.A. Sokolov, et al., Status and key issues of reduced activation ferritic/martensitic steels as the structural material for a DEMO blanket, J. Nucl. Mater. 417 (2011) 9–15. doi:10.1016/j.jnucmat.2011.05.023.

[122] H. Tanigawa, T. Hirose, K. Shiba, R. Kasada, E. Wakai, H. Serizawa, et al., Technical issues of reduced activation ferritic/martensitic steels for fabrication of ITER test blanket modules, Fusion Eng. Des. 83 (2008) 1471–1476. doi:10.1016/j.fusengdes.2008.07.024.

[123] A. von der Weth, A. Felde, H. Hellmeier, J. Rey, S. Rudolf, Theoretical investigation of a first wall fabrication process, J. Nucl. Mater. 417 (2011) 25–28. doi:10.1016/j.jnucmat.2011.05.022.

[124] T. Nagasaka, M. Kondo, T. Muroga, A. Sagara, O. Motojima, T. Tsutsumi, et al., Development of anti-corrosion coating on low activation materials against

fluoridation and oxidation in Flibe blanket environment, Fusion Eng. Des. 85 (2010) 1261–1265. doi:10.1016/j.fusengdes.2010.03.012.

[125] J. Konys, W. Krauss, Z. Zhu, Q. Huang, Comparison of corrosion behavior of EUROFER and CLAM steels in flowing Pb–15.7Li, J. Nucl. Mater. 455 (2014) 491–495. doi:10.1016/j.jnucmat.2014.07.045.

[126] Y. Li, H. Abe, T. Nagasaka, T. Muroga, M. Kondo, Corrosion behavior of 9Cr-ODS steel in stagnant liquid lithium and lead–lithium at 873 K, J. Nucl. Mater. 443 (2013) 200–206. doi:10.1016/j.jnucmat.2013.07.026.

[127] E. Ruedl, T. Sasaki, Effect of lithium on grain-boundary precipitation in a Cr-Mn austfnitic steel, Journal of Nuclear Materials, 116 (1983) 112-122.

[128] Q. Xu, M. Kondo, T. Nagasaka, T. Muroga, M. Nagura, A. Suzuki, Corrosion characteristics of low activation ferritic steel, JLF-1, in liquid lithium in static and thermal convection conditions, Fusion Eng. Des. 83 (2008) 1477–1483. doi:10.1016/j.fusengdes.2008.05.034.

[129] T. Muroga, T. Nagasaka, M. Kondo, A. Sagara, N.Noda, A. Suzuki, T. Terai, Compatibility of reduced activation ferritic/martensitic steels with liquid breeders, NIFS report, 2008.

[130] X. Chen, Z. Shen, X. Chen, Y. Lei, Q. Huang, Corrosion behavior of CLAM steel weldment in flowing liquid Pb-17Li at 480 °C, Fusion Eng. Des. 86 (2011) 2943–2948. doi:10.1016/j.fusengdes.2011.07.005.

[131] V. Tsisar, M. Kondo, T. Muroga, T. Nagasaka, I. Matushita, Morphological and compositional features of corrosion behavior of SUS410–SUS410, SUS316–SUS316 and SUS410–SUS316 TIG welded joints in Li, Fusion Eng. Des. 87 (2012) 363–368. doi:10.1016/j.fusengdes.2012.03.014.

[132] W. Wang, N. Roubier, G. Puel, J.-M. Allain, I.C. Infante, J.-P. Attal, et al., A New Method Combining Finite Element Analysis and Digital Image Correlation to Assess Macroscopic Mechanical Properties of Dentin, Materials. 8 (2015) 535–550. doi:10.3390/ma8020535.

[133] J.B. Wachtman, W.R. Cannon, M.J. Matthewson, Mechanical Properties of Ceramics, John Wiley & Sons, 2009.

[134] George D. Quinn, Brain T. Sparenberg, Philip Koshy, Lewis k. Ives, Said Jahanmir, Dwayne D. Arola, Flexural strength of ceramic and glass rods, Journal of Testing and Evaluation, 37 (3)(2009)1-23.

[135] Walter D. Musial, Ben Bourne, Scott D. Hughes, Michael D. Zuteck, Four-point bending strength testing of pultruded fiberglass wind turbine blade section, AWEA's WINDPOWER 2001 Conference, June 4-7, 2001, Washington, D.C., USA.

[136] H. Yoshihara, Y. Sawamura, Measurement of the shear modulus of wood by the square-plate twist method, Holzforschung. 60 (2006). doi:10.1515/HF.2006.090.

[137] W. Araki, K. Nemoto, T. Adachi, A. Yamaji, Fracture toughness for mixed mode I/II of epoxy resin, Acta Mater. 53 (2005) 869–875. doi:10.1016/j.actamat.2004.10.035.

[138] Ö. Unal, I.E. Anderson, J.L. Harringa, R.L. Terpstra, B.A. Cook, J.C. Foley, Application of an asymmetrical four point bend shear test to solder joints, J. Electron. Mater. 30 (2001) 1206–1213. doi:10.1007/s11664-001-0151-7.

[139] C.A. Lewinsohn, M. Singh, T. Shibayama, T. Hinoki, M. Ando, Y. Katoh, et al., Joining of silicon carbide composites for fusion energy applications, J. Nucl. Mater. 283–287, Part 2 (2000) 1258–1261. doi:10.1016/S0022-3115(00)00247-6.

[140] H. SERIZAWA, C.A. Lewinsohn, H. MURAKAWA, FEM Evaluation of Asymmetrical Four-Point Bending Test of SiC/SiC Composite Joints(Mechanics, Strength & Structure Design), Trans. JWRI. 30 (2001) 119–125.

[141] H. Serizawa, C.A. Lewinsohn, H. Murakawa, FEM Analysis of Asymmetrical Bending Test for Smart Materials Joints, Mater. Trans. 43 (2002) 994–1000. doi:10.2320/matertrans.43.994.

[142] K. Ueda, M. Satou, A. Hasegawa, K. Abe, Deformation analysis of small size bend specimens by FEM calculation to estimate irradiation induced embrittlement of Mo and W, J. Nucl. Mater. 258–263, Part 1 (1998) 466–470. doi:10.1016/S0022-3115(98)00307-9.

[143] J. Henry, L. Vincent, X. Averty, B. Marini, P. Jung, Bending tests on T91 samples implanted with 0.25 at.% helium: Experiments and mechanical analysis, J. Nucl. Mater. 356 (2006) 78–87. doi:10.1016/j.jnucmat.2006.05.004.

[144] M.A. Meyers, K.K. Chawla, Mechanical Behavior of Materials, 2 edition, Cambridge University Press, Cambridge ; New York, 2008.

[145] B.J.M. Donald, Practical Stress Analysis with Finite Elements, Glasnevin Publishing, 2007.

[146] D. Sang, G. Jones, Cambridge O Level Physics with CD-ROM, Cambridge University Press, 2012.

[147] N.N. Greenwood, A. Earnshaw, Chemistry of the Elements, Elsevier, 2012.

[148] F. Tavassoli, Appendix A Material Design Limit Data A3.S18E Eurofer steel, Fusion Demo Interim Structural Design Criteria, 2004.

[149] B.J.M. Donald, Practical Stress Analysis with Finite Elements, 2nd edition, Glasnevin Publishing, Dublin, 2011.

[150] B. Kudryavtsev, Sounds We Cannot Hear, The Minerva Group, Inc., 2001.

[151] R. Farraro, R.B. Mclellan, Temperature dependence of the Young's modulus and shear modulus of pure nickel, platinum, and molybdenum, Metall. Trans. A. 8 (1977) 1563–1565. doi:10.1007/BF02644859.

[152] S.J. Zinkle, J.P. Robertson, R.L. Klueh, Thermophysical and mechanical properties of Fe-(8-9)%Cr reduced activation steels.

[153] P.J. Blau, Friction Science and Technology: From Concepts to Applications, Second Edition, CRC Press, 2008.

[154] D.J. Sheskin, Handbook of Parametric and Nonparametric Statistical Procedures: Third Edition, CRC Press, 2003.

[155] 温诗铸, 黄平, 摩擦学原理, 清华大学出版社有限公司, 2002.

Abbreviations

A: austenite

BM: base metal

CCT: continuous cooling transformation

DBTT: ductile-to-brittle transition temperature

DEMO: Demonstration reactor

DGR: deep geological repository

D-T: deuterium-tritium

EBW: electron beam welding

EDS: energy dispersive X-ray spectroscopy

F: ferrite

FEM: finite element method

FFHR: force-free helical reactor

FIREX: the Fast Ignition Realization Experiment project

FSW: friction stir welding

HAZ: heat-affected zone

HIP: hot isostatic pressing

HP: hot pressing

IL: interlayer

i-LIFT: International Laboratory Inertial Fusion Test

ITER: International Thermonuclear Experimental Reactor

JET: Joint European Torus

KIT: Karlsruhe Institute for Technology

KSTAR: Korea Superconducting Tokamak Advanced Research facility

LHD: the Large Helical Device

LMJ: the Laser MegaJoule Facility

LW: laser welding

M: martensite

N: normalization

N&T: normalization and tempering

NIF: the National Ignition Facility

NIFS: National Institute for Fusion Science

ODS: oxide-dispersion-strengthened

OM: optical microscopy

PRW: pressurized resistance welding

PWHT: post-weld heat treatment

RAFM: reduced activation ferritic/martensitic

RT: room temperature

SEM: scanning electron microscopy

SLB: shallow land burial

SPS: spark plasma sintering

T: tempering

TBM: test blanket module

TEM: transmission electron microscopy

TFTR: the Tokamak Fusion Test Reactor tritium facility

TIGW: tungsten inert gas welding

USE: upper shelf energy

VIM: vacuum induction melting

WM: weld metal

W7-X: the WENDELSTEIN 7-x strellarator

List of Tables

List of Figures

145

Published papers and conference presentations

Papers

(1) H.Y. Fu, T. Nagasaka, T. Muroga, A. Kimura, J.M. Chen, Microstructural characterization of a diffusion-bonded joint for 9Cr-ODS and JLF-1 reduced activation ferritic/martensitic steels, Fusion Engineering and Design, 89 (2014)1658-1663.

(2) H.Y. Fu, T. Nagasaka, T. Muroga, W.H. Guan, S. Nogami, A. Hasegawa, H. Serizawa, Weldability of 9Cr-ODS and JLF-1 Steels for Dissimilar Joining with Hot Isostatic Pressing and Electron Beam Welding, Plasma and Fusion Research, 10 (2015)3405015 1-4.

(3) H.Y. Fu, T. Nagasaka, T. Muroga, Microstructural evolution of 9Cr-ODS and JLF-1 in a HIP joint after post-bond heat treatment, Journal of Plasma and Fusion Research SERIES,11 (2015)61-64.

(4) H.Y. Fu, T. Nagasaka, N. Kometani, T. Muroga, W.H. Guan, S. Nogami, K. Yabuuchi, T. Iwata, A. Hasegawa, M. Yamazaki, S. Kano, Y. Satoh, H. Abe, H. Tanigawa, Effect of post-weld heat treatment and neutron irradiation on a dissimilar-weld joint of F82H RAFM steel and 316L stainless steel, Fusion Engineering and Design, in press.

(5) H.Y. Fu, T. Nagasaka, T. Muroga, W.H. Guan, S. Nogami, H. Serizawa, S. F. Geng, K. Yabuuchi, A. Kimura, Plastic deformation behavior and bonding strength of an EBW joint between 9Cr-ODS and JLF-1 estimated by symmetric four-point bend tests combined with FEM analysis, Fusion Engineering and Design, under review.

Conferences

(1) H.Y. Fu, T. Nagasaka, T. Muroga, A. Kimura, J.M. Chen, Microstructural characterization of a diffusion-bonded joint for 9Cr-ODS and JLF-1 reduced activation ferritic/martensitic steels, the 11th International Symposium on Fusion Nuclear Technology, 16-20 September, 2013, Barcelona, Spain.

(2) H.Y. Fu, T. Nagasaka, T. Muroga, A. Kimura, Mechanical properties evaluation for a HIPed joint of 9Cr-ODS and JLF-1 reduced activation ferritic/martensitic steels, the 23rd International Toki Conference on Large-scale Simulation and Fusion Science, 18-21 November, 2013, Gifu, Japan.

(3) H.Y. Fu, T. Nagasaka, T. Muroga, Microstructural evolution of 9Cr-ODS and JLF-1 in a HIP joint after post-bond heat treatment, the 12th Japan-China Symposium on Materials for Advanced Energy Systems and Fission& Fusion Engineering, 17-20 September, 2014, Shizuoka, Japan.

(4) H.Y. Fu, T. Nagasaka, N. Kometani, T. Muroga, W.H. Guan, S. Nogami, K. Yabuuchi, T. Iwata, A. Hasegawa, M. Yamazaki, S. Kano, Y. Satoh, H. Abe, H. Tanigawa, Effect of post-weld heat treatment and neutron irradiation on a dissimilar-weld joint of F82H RAFM steel and 316L stainless steel, the Symposium of Fusion Technology (SOFT28), September 29th-October 3rd, 2014, San Sebastian, Spain.

(5) H.Y. Fu, T. Nagasaka, T. Muroga, W.H. Guan, S. Nogami, A. Hasegawa, H. Serizawa, Evaluation of bonding strength with finite element method simulation of the joints for 9Cr-ODS and JLF-1, the 24th International Toki Conference (ITC-24) on Expanding Horizons of Plasma and Fusion Science through Cross-Fertilization, November 4-7, 2014, Gifu, Japan.

(6) H.Y. Fu, T. Nagasaka, T. Muroga, W.H. Guan, S. Nogami, H. Serizawa, S. F. Geng, K. Yabuuchi, A. Kimura, Mechanical properties of dissimilar-metals bonding between low-activation ferritic steel and ODS steel, the 6th International Symposium of Advanced Energy Science—Towards the Realization of Zero-Emission Energy, September 1-3, 2015, Kyoto University, Japan.

Acknowledgements

Besides research work and studies, I have also met a lot of good professors and young friends. They are friendly and energetic. From them I learnt how to be a researcher and a happy person. I express my great appreciation to them.

At last, I want to express gratefulness from the support of my family especially my father and my husband.